Title
Drift Natural Convection and Seepage at the Yucca Mountain Repository

Author
Halecky, Nicholaus Eugene

Publication Date
2010

Peer reviewed|Thesis/dissertation

DRIFT NATURAL CONVECTION AND SEEPAGE AT THE YUCCA MOUNTAIN REPOSITORY

by

Nicholaus Eugene Halecky

A dissertation submitted in partial fulfillment
of the requirements for the degree of

Doctor of Philosophy
in
Engineering – Nuclear Engineering

in the
GRADUATE DIVISION
of the

UNIVERSITY OF CALIFORNIA, BERKELEY

Committee in charge:

Professor Per F. Peterson, Chair
Professor Joonhong Ahn
Dr. Jens T. Birkholzer
Professor T. N. Narasimhan

Fall 2010

Abstract

Drift Natural Convection and Seepage at the Yucca Mountain Repository

by Nicholaus Eugene Halecky

Doctor of Philosophy in Nuclear Engineering

Department of Nuclear Engineering

University of California, Berkeley

Professor Per. F.Peterson, Chair

The decay heat from radioactive waste that is to be disposed in the once proposed geologic repository at Yucca Mountain (YM) will significantly influence the moisture conditions in the fractured rock near emplacement tunnels (drifts). Additionally, large-scale convective cells will form in the open-air drifts and will serve as an important mechanism for the transport of vaporized pore water from the fractured rock, from the hot drift center to the cool drift end. Such convective processes would also impact drift seepage, as evaporation could reduce the build up of liquid water at the tunnel wall. Characterizing and understanding these liquid water and vapor transport processes is critical for evaluating the performance of the repository, in terms of water-induced canister corrosion and subsequent radionuclide containment. To study such processes, we previously developed and applied an enhanced version of TOUGH2 that solves for natural convection in the drift. We then used the results from this previous study as a time-dependent boundary condition in a high-resolution seepage model, allowing for a computationally efficient means for simulating these processes. The results from the seepage model show that cases with strong natural convection effects are expected to improve the performance of the repository, since smaller relative humidity values, with reduced local seepage, form a more desirable waste package environment.

Drift Natural Convection and Seepage
at the Yucca Mountain Repository
by
Nicholaus Eugene Halecky

"The release of atomic energy has not created a new problem. It has merely made more urgent the necessity of solving an existing one."

Albert Einstein (1879-1955).

Acknowledgements

I have nothing but admiration for...

Dr. Jens T. Birkholzer, my supervisor, for his guidance, patience, and knowledge during my graduate education, I will always be grateful.

Julia Auzmendi, for her enduring support during my final hours.

Christopher Cantalupo, in the lasts moment, you made all of this possible.

Contents

List of Figures

List of Tables

Dedicated to Mom and Dad,

Chris, Aaron, Tim,
and Julia.

Chapter 1

Introduction

Even before United States President Franklin D. Roosevelt received the Einstein-Szilárd letter on August 2, 1939, warning the President of the possibility for the creation ofd an extremely destructive nuclear device using recently-developed enriched uranium, man-made radioactive waste had been introduced into the environment, at a small but ever-increasing rate. Heeding the warning that the two physicists wrote about, Roosevelt convened a scientific commission to explore the potential of this immense technological advancement and with this began the Manhattan Project and along with it, the dawn of the nuclear era. Since the time of the sciences infancy in the early 1940's—from Enrico Fermi's first sustained nuclear reaction to the detonation of Trinity, the first nuclear weapon—nuclear technologies have evolved rapidly.

Now encompassing non-destructive and beneficial roles such as the production of non-carbon, nuclear generated electricity, major advancements in medical imaging and diagnostics, and material detection—modern societies dependency on nuclear technology had been firmly established. Still, as tremendous benefits have been realized by society from such technologies, the burden of an ever-increasing volume of the toxic byproducts of these nuclear processes have become more apparent.

From the initial criticality experiments at the University of Chicago, during which time the scientists involved were harmed by receiving extreme doses of radiation[1], the scientific knowledge of the effects of radiation exposure on human beings[1, 2] has advanced in parallel with the understanding of nuclear processes themselves. Radiation emitting radioactive waste—in the form of spent nuclear fuel, residual material from nuclear weapons decommissioning, byproducts from the production of radioisotopes for medical imaging and industry use, and other naturally occurring sources—has become an aspect of life in modern times. The sequestering of these toxic radioactive materials from human populations, other living organisms and the environment

[1]During this time of research and understanding of basic nuclear processes, little was still understood about the effects of ionizing radiation, how it was created, transported and how it damages human tissue.

at large, has become a necessary obligation due to our past and continuing use of nuclear technologies.

1.1 Yucca Mountain Repository

Yucca Mountain was the proposed geologic disposal site for the high level waste (HLW) that currently exists in the United States including spent nuclear fuel, defense waste from weapons decommissioning, and vitrified waste byproducts from nuclear weapons development. The repository was to serve as secure and central location for the storage and sequestration of toxic radionuclides from the biosphere for a time sufficient enough to allow the decay of even the longest-lived radionuclides to benign products.

1.1.1 History and Current Status

In 1955, the U. S. Atomic Energy Commission (AEC) requested that the National Academy of Sciences (NAS) recommend options for the disposal of radioactive wastes from the production of nuclear weapons. A few years later in 1957 after much discussion and debate, the NAS reported back their findings and recommended disposal of transuranic and high-level wastes in geologic formations, specifically suggesting further research into burial in salt beds or salt domes[3]. Although the salt deposits in Lyons, Kansas were initially selected as the location for such geologic disposal, in 1972 the federal government withdrew the selection due to concern that recent drilling in the vicinity of the deposits had compromised the integrity of the site for geologic disposal of nuclear waste.

After this, little progress came from the national disposal effort until a decade later when the *Nuclear Waste Policy Act (NWPA)* was passed by Congress in 1982, helping to resolve the long-term nuclear waste disposal issue, and establishing geologic disposal as the strategy for nuclear waste disposal in the United States. In addition, the act reestablished the responsibility of the federal government for management of the country's spent nuclear fuel and designated roles for oversight of these responsibilities to three government agencies. Combined, these agencies encompass all the responsibilities designated to the since disbanded AEC, and are:

- **Department of Energy (DOE)** - responsible for design, construction, operation and closure of the geologic repository. DOE created the Office of Civilian Radioactive Waste Management (OCRWM) to manage these responsibilities.
- **Environmental Protection Agency (EPA)** - responsible for developing the public health and safety standards for the repository.

- **Nuclear Regulatory Commission (NRC)** - responsible for licensing the repository, ensuring that the DOE design meets the standards required by the EPA.

Of the nine sites selected by DOE as potential repositories, in 1986 President Reagan approved three sites (Hanford, Washington; Deaf Smith, Texas; and Yucca Mountain, Nevada) for further study and site characterization. A year later, due to political pressures and limited funding, Congress amended the NWPA to direct DOE to focus research of waste disposal only on Yucca Mountain. Since that time in 1987 to now, a total of around $9 billion USD worth of research has been performed to characterize Yucca Mountain for use as a repository, making it the most heavily researched geological structure in history. In the most recent *Total System Life Cycle Cost* analysis, OCRWM concluded the total cost for Yucca Mountain to be just under $100 billion dollars ($96.18 billion in constant 2007 US dollars)[2], including both the historical costs and costs projected through decommissioning, which would occur in 2133[7].

Following the legal framework set by the NWPA, in June 2008, DOE submitted the License Application (LA) to the NRC for review of the DOE's plans for construction, operation and closure of the repository. The NRC thus began its review of designs for each aspect of the repository and ensure that DOE could safely perform all responsibilities in compliance with established regulations. This LA review was expected to be completed in 3-4 years in 2011, however, much has changed in recent times.

In early 2009, with the newly elected Obama administration, the federal government made a break with previous Presidential administrations on the national strategy for disposal of long-lived radioactive waste with their opposition to long term geologic disposal at Yucca Mountain and filed to withdraw from their investigation of Yucca Mountain in March of 2010[8]. Under the direction of former Lawrence Berkeley National Laboratory director and current Department of Energy Secretary, Dr. Steven Chu, the administration has currently assembled a 15-member Blue Ribbon Commission[3] to explore alternative options for the nation's long-term nuclear waste management strategy.

A very recent study by MIT, however, emphasizes that regardless of the fuel cycle (open, closed, or partially closed), some form of interim storage will be necessary along with long term storage for residual long-lived isotopes from either process[9]. How US policy makers will respond is yet to be seen. Still though, current actions by

[2]For comparison, the costs of other national endeavors in units of constant 2007 dollars:

1. The Manhattan Project (1939 through 1945): **$26.4 billion**[4]
2. Apollo Space Program: **$180 billion** [5]
3. The Global War on Terror™(post 9/11 through 2010): **$1,000 billion**[6]

[3]Serving on this commission is Prof. Per Peterson, current Chair of the Department of Nuclear Engineering at U.C. Berkeley, my dissertation committee chair, and also my advisor during my time as a graduate student.

federal administration make clear that Yucca Mountain will not be used in the manner for which was previously intended. In October of 2010, the chairman of the NRC, Gregory Jaczko, directed his scientists to halt their review of the License Application submitted by DOE to validate of the plans for waste disposal at Yucca Mountain[10]. At the time of this writing, it is unclear what the future of Yucca Mountain[4] and geologic disposal of radioactive waste will be in the United States.

1.1.2 Region Characteristics

Yucca Mountain is located in Nye County in southern Nevada at the former Nevada Nuclear Test Site and is roughly 120 km northwest of Las Vegas, Nevada—one of the United States' fastest growing metropolitan areas. Yucca Mountain consists of a federally owned land withdrawal of about 230 square miles (600 square kilometers), and is located about 14 miles (22.5 kilometers) from the nearest year-round population of Lathrop Wells, now collectively incorporated into what is known as Amorgosa Valley (Figure 1.1). Located in a high altitude desert, the peak elevation at the crest of the mountain is at almost 5000 ft. (1525 m) above sea level. The modern-day regional climate has average temperatures ranging from 29℃ (84˚F) in the summer to 6℃ (43˚F) during the winter[11]. The region is also very arid receiving less that 7.5 inches (170 mm) of rainfall annually, very little of which actually infiltrates into the mountain (about 5-6 $^{mm}/_{year}$)[12].

Geologically, Yucca Mountain is composed primarily of stratified layers of compacted volcanic ash tuff, deposited some 10 million years ago, and contains no resources of commercial value, ensuring that future generations will have little desire for excavation in the region[13]. Ash tuff at Yucca Mountain is a highly fractured rock, with strong heterogeneity existing though both the fracture and matrix domains, along with both welded and non-welded geologic layers that significantly alter the characteristics of groundwater flow through the vadose zone. Studies have shown that most water flow through the rock occurs through the fracture domain, as the permeability of the matrix is extremely small (10^{-18} m^2), however, not all fracture pathways are continuously connected and therefore do not serve as a continuous flow path for percolation water.

1.1.3 Repository Design

Following the concepts of geologic disposal, the desolate, dry, and removed region of Yucca Mountain serves first and foremost as a *natural barrier* by significantly reducing the ensuing migration of the radionuclides from the repository location, through the geosphere (the geologic region through which the maybe transported), and

[4]For sake of clarity, reading rhythm, and tone, the remainder of this dissertation will reference the now considered expired plans of a geologic repository at Yucca Mountain in the present tense.

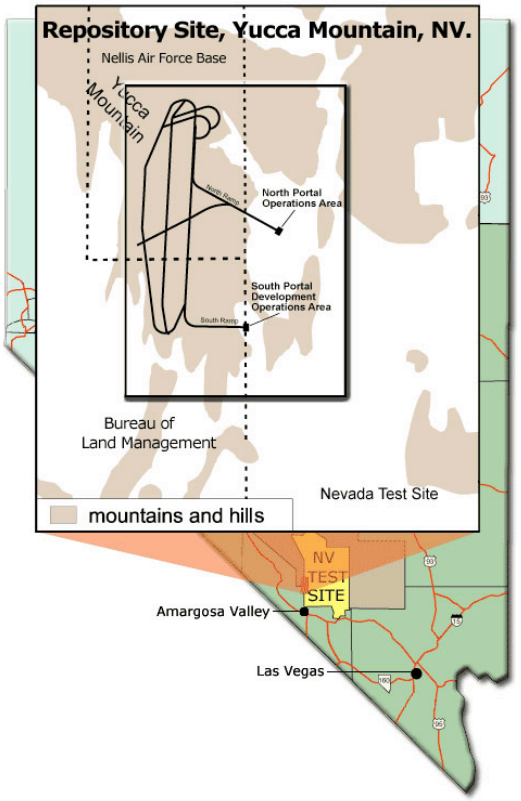

Figure 1.1: Yucca Mountain location, southwest Nevada

to the biosphere (the region where the radionuclides could contact living organisms). During their lifespan, the radionuclides undergo decay, changing the characteristics of their toxicities and eventually becoming benign, as is the case for some radionuclide species, or reduced to a concentration that poses no increased harm when compared to background radiation exposure from the ambient environment.

To further delay the introduction of radionuclides into the geosphere, the waste canisters containing the different forms of radioactive waste provide an additional *engineered barrier*—offsetting the release by an assumed 10,000 years. This is, however, a very conservative estimate as corrosion modeling studies predict that the canisters will remain intact for much longer times (∼300,000 years)[14]. Still, the performance of these canisters is integral part of the performance of the repository at large, allowing a considerable amount of decay of the radionuclides to occur before their release into the geosphere. This engineered barrier together with the natural barrier form a multi-barrier concept to the sequestration of radioactive waste at Yucca Mountain.

The downward migration of the radionuclides from the repository through the thick unsaturated zone towards the water table at Yucca Mountain is driven primarily by

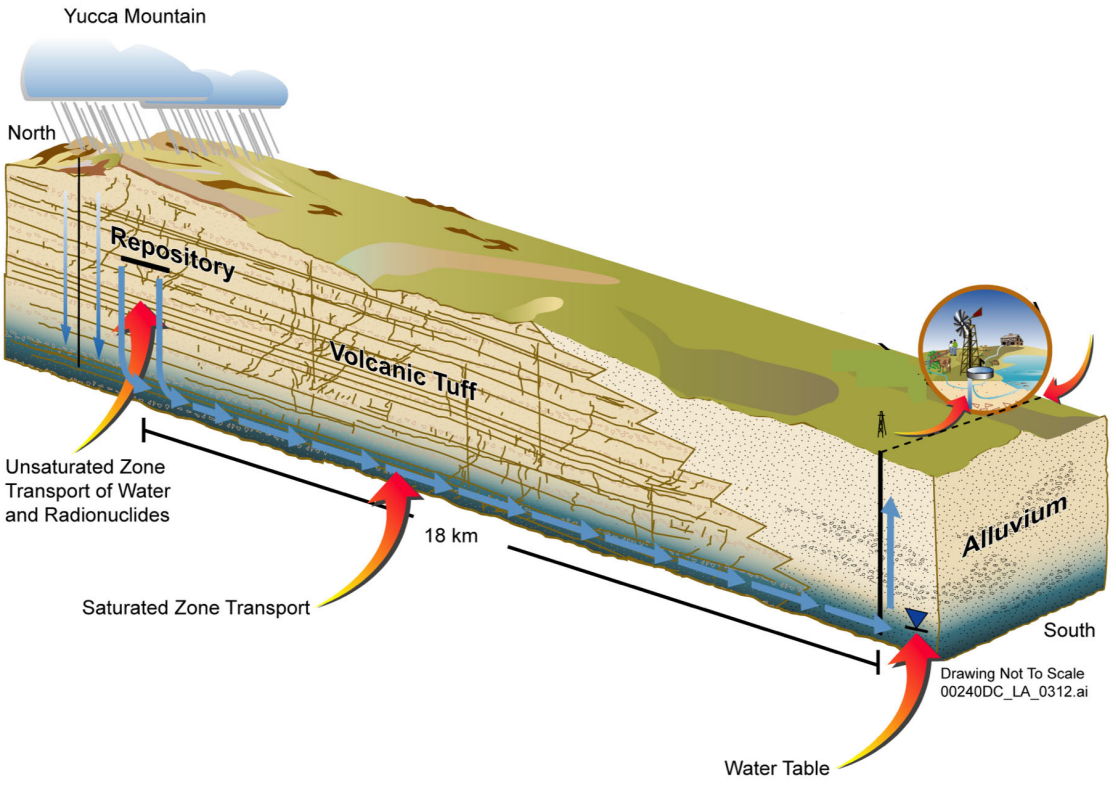

Figure 1.2: Flow path of radionuclides from repository and into biosphere

bulk advection transport with the flow of groundwater within the fracture network. However, due to the long time scales over which these transport processes would occur, also important for some of the radioisotope species is the effect of diffusive transport into the matrix domain. Depending on the radionuclide colloid size, matrix diffusion can assist in significantly retarding radionuclide transport though the unsaturated zone[15]. As shown in Figure 1.2, the groundwater flow path through the Yucca Mountain region starts with rainfall at the mountain surface. While most of this water is transported back to the air through evaporation and transpiration in the soil, a small amount of the rainwater infiltrates into the ground, thus providing the source for water within the geologic system. Gravity-induced flow allows the water to slowly percolate downward through the unsaturated rock until it reaches the water table below. Here, in the saturated zone, exists another gravity potential, from the water table elevation below the repository to the elevation of the aquifer below the Armagosa Valley, driving the groundwater south. From this aquifer, water could be extracted from wells for terrestrial use in irrigation and drinking, thus completing the groundwater flow pathway from the repository to the biosphere.

The planned repository horizon exists entirely in the unsaturated zone (UZ), about 1000 ft. (300 m) above the water table with the surface of the mountain existing

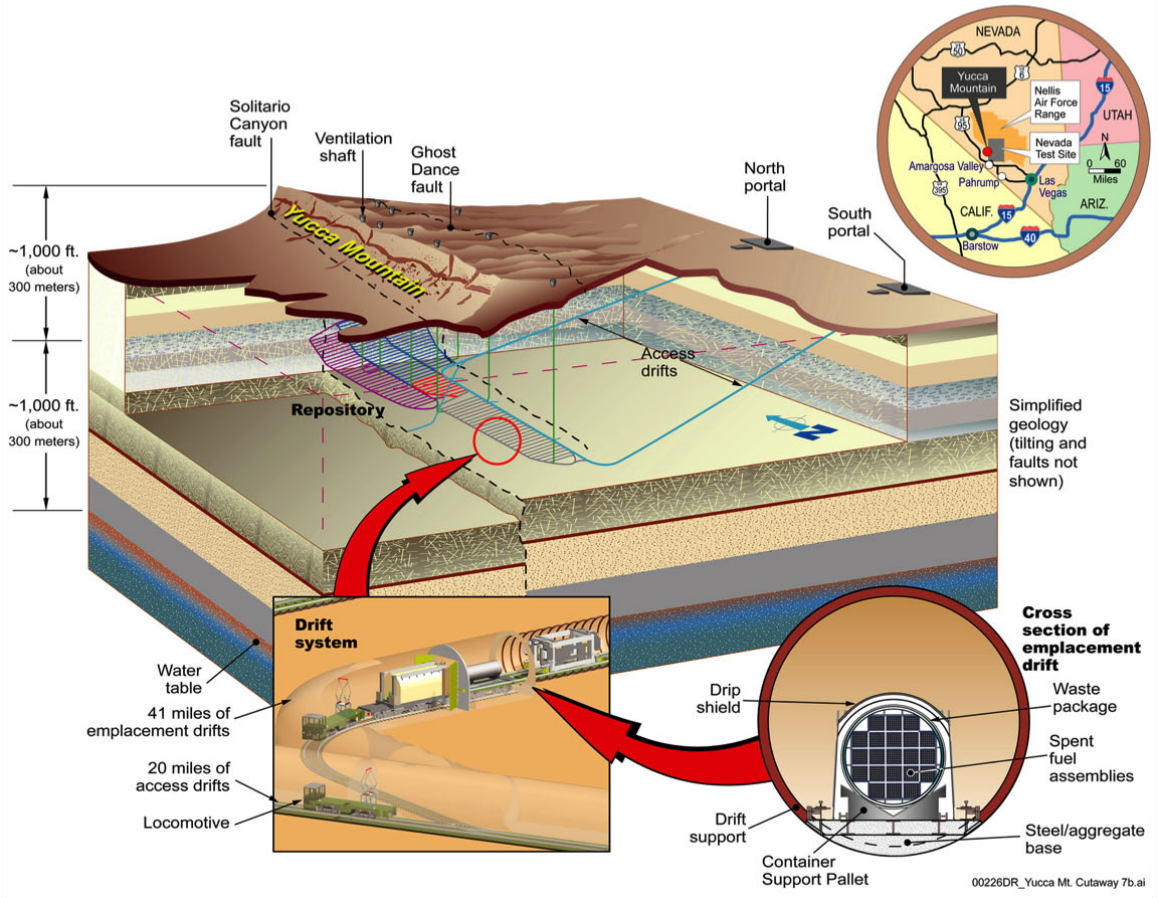

Figure 1.3: Cutaway image of Yucca Mountain, rock layers, and the planned network of repository tunnels along with cross-sectional view of an emplacement drift (from Figure 1 in [17]).

another 1000 ft. (300 m) above. The repository design considers of a network of parallel emplacement tunnels (often referred to as drifts), each being about 600 m in length followed by end sections (turnouts) that can be as long as 100 m or more. The emplacement drifts are 5.5 meters in diameter and are spaced at intervals of 81 meters, center to center. In the current design, cylindrical waste canisters will be distributed along these horizontal tunnels, which in total provide more than 112 miles (180 kilometers) of waste emplacement distance, which, in comparison, is nearly the size of the subway system in New York City[16]. The repository is accessed via two portal tunnels entering east of the Yucca Mountain range, about 8 miles away to the east (shown in Figure 1.3).

The emplacement drifts are to contain all waste package types from the various waste streams that are to be disposed in Yucca Mountain including vitrified high level waste, spent nuclear fuel, and waste from weapons development along with other military

use. The cylindrical waste canisters range from 1.75 m to 2.11 m in diameter and are ∼5 m in length, and will be distributed in 0.1 m intervals along the length of the drift. Robotic trains will transport the waste packages from a sorting and storage facility on the surface through the access drifts to the emplacement tunnels where they will be placed horizontally on pallets. After the final waste canister is emplaced, forced ventilation cooling will proceed for a period of 50 years, helping to remove a significant amount of decay heat from the waste that would have otherwise heated the surrounding fractured rock. After ventilation, a titanium drip shield will be installed over all waste canister surfaces, preventing seepage water from contacting the canister surfaces, after which the repository is to be shut permanently.

The average rate of water transport through the UZ is extremely slow (∼10 mm/year), thus minimizing the contribution of the rate of advective transport of radionuclides into the water table below. Still, the fractured tuff at Yucca Mountain has shown to provide preferential fast-flow pathways, whereby certain large, episodic infiltration rates see the groundwater flow quickly through the the fracture network, allowing downward transport to occur at a much larger local rate[18]. Similar to the flow pathway for groundwater, the path for radionuclide transport starts at the repository itself, where radionuclides, once introduced to the fractured host rock at the drift wall (through failure of the waste canister and subsequent release of the waste contained therein), must transport downward through the unsaturated zone before reaching the water table. From here, groundwater flow in the saturated zone eventually transports the radionuclides south to the water table below the Armagosa Valley (Figure 1.2), with possible ingestion by the use of water from the contaminated aquifer.

1.2 Thermal Hydrological Processes at Yucca Mountain

To ensure that the repository at Yucca Mountain is suitable for the disposal of high-level radioactive waste, the understanding of both the:

- **Thermodynamic conditions of the in-drift environment** during the initial closure of the repository—governing the lifespan of the waste canisters and, subsequently, the average release time of the radionuclides into the geosphere, and also the,
- **Thermal-Hydrological (TH) processes that govern the flow pathways in the surrounding fractured rock**—governing the mechanisms by which radionuclides transport in the fractured rock (both by advective and diffusive processes) and also determining the thermodynamic conditions of the in-drift,

are necessary. Extensive and rigorous scientific investigations conducted over the last thirty or more years to understanding such processes have explored whether the site functions well for such a purpose[19]. Among the many parameters important for describing both the transport behavior of the repository and in-drift conditions (e.g., rate of percolation, decay heat rate, permeability, etc.), the temperature of the local rock environment can impact flow processes significantly. The effect of decay heat (generated from the thermal energy imparted by the particles emitted during radioactive decay) and the resultant temperature increase in the surrounding rock, has been investigated by many predictive modeling research endeavors.

1.2.1 Previous Investigations

From the first borehole samples being drilled in 1978, to the initial conceptual models that were developed in the early 1980's, characterization of Yucca Mountain has seen much progress (a wonderful history of this development can be found in Flint et al., 2001[20]). After advances from matrix-dominated flow models of the UZ region at Yucca Mountain[21], numerical modeling of the near-field[5] environment was first used to understand possible temperature response of the rock formation surrounding the in-drift, by varying the mobility of liquid water in the fractures[22]. Building off this, further effort saw the development of the dual-continuum (dual-permeability) approximation for capturing the complex interactions between the fractures and matrix domains, by creating two overlapping continua in space (one for both fractures and matrix), each with their own unique hydraulic properties and a unique model for how they interact. The limitations of where such an approximation can be made was also well explored[23]. As refinement of these models continued, the modeling community saw the development of TOUGH2 (described in more detail in Chapter 2), a robust porous media simulator used to significantly expand the breath and scope of the modeling efforts of Yucca Mountain[24].

To capture the behavior the thermally-driven flow processes induced by the specific design of the repository, three dimensional representations of the entire repository were modeled (referred to as the Yucca Mountain Unsaturated Zone (UZ) model) and simulated, yielding predictions of the large-scale average temperature and moisture response, and the effects of Dirichlet-type boundary conditions at the water table and mountain surface[25]. Conversely, to capture the unique TH behavior of the drift-region, near the waste packages (including the emplacement drift and surrounding fractured rock), more-refined, two-dimensional models were also developed. These models contributed to the knowledge of liquid seepage processes (discussed a greater length in Chapter 5: Drift Seepage) in emplacement drifts, along with other near-field effects (e.g., heat pipes, heterogeneity of rock properties)[26, 27]. Other investigations attempted to capture the interaction between both the repository-scale response

[5]The *near-field* refers to the rock environment nearby an emplacement drift.

and drift-scale response with the development of multiscale models, exploring various manners of repository operation (e.g., backfill, dripshield, ventilation time, etc.)[28]. Validations of the methodologies employed by these models were conducted by comparison of the predictive model results with observed data of TH response of large in situ[6] heater tests, performed on site at Yucca Mountain[29–32]. More discussion on model validation can be found in Section 6.1: Model Validation and Limitations.

These investigations advanced the knowledge of repository behavior, showing that for quite some time after ventilation ceases the temperatures within and near emplacement drifts will be above boiling (around 500-600 years), initially reaching 140℃ at the rock wall. These temperatures were shown to give rise to complex multiphase mass and heat transfer processes[26, 33], in both the fractured rock and the open emplacement drifts containing the waste canisters. Pore-water, from the small amount of rainfall that feeds the hydrological cycles at Yucca Mountain, slowly flows through the unsaturated rock nearby an emplacement drift (Figure 1.4). The heated conditions of the rock there vaporize the liquid, which then transports via pressure and concentration gradients, and condenses in cooler areas of the rock, leading to a large saturation and flux redistribution, specifically near the emplacement drifts where temperature changes compared to ambient conditions are extreme.

This better understanding of the strong coupling between hydrological and thermal processes, and the resulting behavior within the heterogenous fractured rock at Yucca Mountain, gave insight into the formation of heat-pipes near the emplacement drift, whose flow magnitudes were investigated in detail[34]. Also investigated was the diversion of flow around the open tunnel due to capillarity of the rock formation, leading to the significant drying of the rock directly below the emplacement tunnel, an effect more commonly referred to as the *drift shadow*. The effect of this drift shadow was explored and found to be beneficial to repository function by further retarding the transport of the radionuclides eventually introduced to this region from the waste canister above[35].

While capturing many aspects of the heated environment response, these studies assumed the effects of heat and mass transport in the open air spaces along the length of the drift to be negligible by either not modeling drift tunnels or defining them as closed systems. As such, the studies predict that water vapor produced by the boiling of porewater remains confined to the fractured rock, while in reality there might be considerable transport of vapor into the open tunnel and subsequently, a large flux and moisture redistribution could also occur within it. Specifically, the presence of the: **(i)** large volumes of rock heated to above boiling conditions, and **(ii)** the ability for vapor to effectively transport through the fracture network spaces to the open tunnel (via convection and diffusion), might give rise to different saturation distribution in

[6] *In situ* is a Latin phrase, directly translated to mean, *in the place*. In the context of Yucca Mountain, it refers to any experiment or procedure performed *at the actual site* of Yucca Mountain in Nevada, at one of the many exploration facilities contained there.

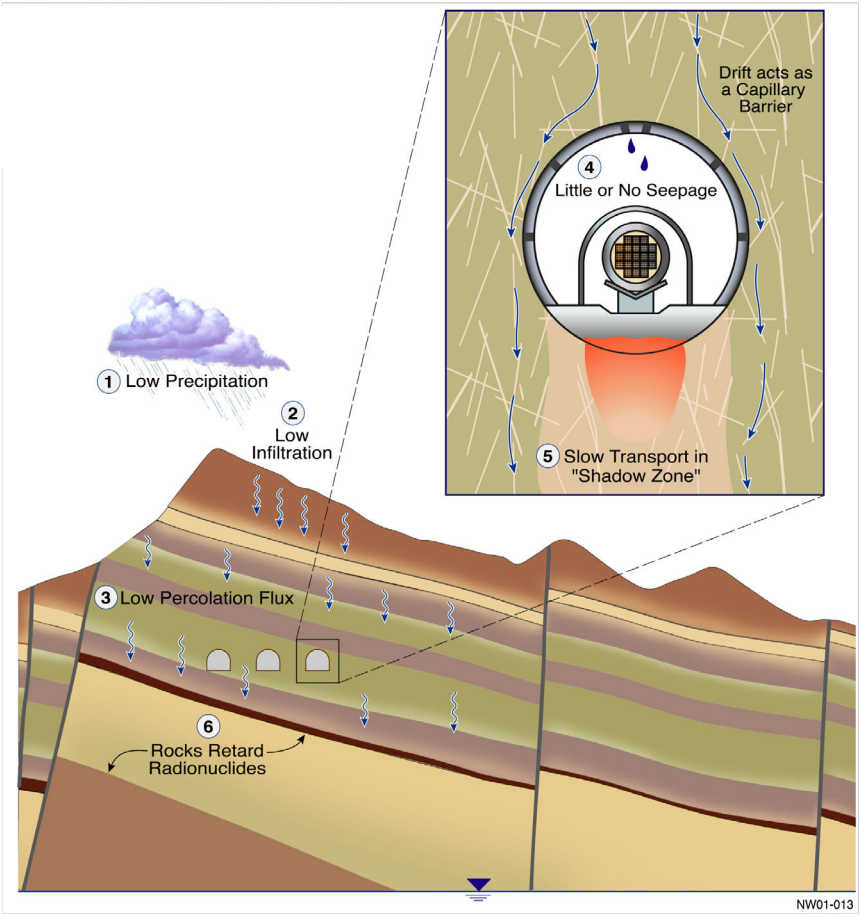

Figure 1.4: Schematic of hydrological processes in the unsaturated zone in the Yucca Mountain repository and around the drift.

the surrounding fractured rock than what was predicted in previous modeling studies when these aspects were not considered.

1.2.2 Current Knowledge

More recently, research into the impact that the open drifts would have on the future in-drift environment have yielded more insight. Using computational fluid dynamic (CFD) simulations of a representative in-drift, Webb and Itamura, 2004[36], have shown that heat output from the waste packages would create a notable axial transport of vapor due to natural convective processes in the drift (interpreted in greater length at Chapter 4: Drift Natural Convection). These studies convey the potential for the removal of water vapor produced in the hot and moist drift center, by transport the cool drift end, reducing the RH in the emplacement region. Ghezzehei et al.

2004[37], investigated the effect of evaporation of liquid water from the drift wall on minimizing seepage during ambient conditions, modeling evaporation as a first-order diffusion process with a boundary-layer approximation. Their results concluded showing evaporation does reduce the potential of seepage by keeping the rock drier with reduced RH of the in-drift environment[37]. Other efforts to understand in-drift transport have also been undertaken regarding the efficiency of ventilation of the repository. Danko and Bahrami, 2003, developed a unique decoupling of the the in-drift and fractured rock domains by representing the near-field in an multi-parameter response function, developed from an iterative refinement with existing TH models[38, 39].

1.2.3 Motivation

While the waste canisters that contain the heat-emitting waste products will be made of advanced materials, highly durable to these extreme environments, they are still susceptible to increased corrosion rates due to the presence of liquid water. With expected time-periods during which there exists both extreme temperatures combined with large vapor transport rates, the presence of liquid water on the canister surface might allow the conditions for an accelerated corrosion process to occur[40], however, there is disagreement as to the likelihood of what specific corrosion events could occur[41, 42]. Still, being that waste canister integrity in terms of canister corrosion and radionuclide containment is critical for the long-term performance of the repository, it is very important to understand and predict what mechanisms exist—in the natural system as well as in the drifts—for allowing the transport and deposition of liquid water to the canister surface.

As discussed with the previously mentioned research efforts, the existing knowledge of the transport processes at Yucca Mountain is extensive, however, does not account for the effects of:

(i) axial heat and vapor transport in open air drift spaces,

(ii) during heated conditions both boiling and sub-boiling,

(iii) while accounting for the important feedback that exists between the

  (a) *fractured rock*—the source of the water vapor that enters the tunnel, and the

  (b) *open drift turnouts*—the sink for the water vapor.

Accounting for such processes allows for a more accurate description of the future environment at Yucca Mountain, contributing to the furthered assurance of the performance of such an important human endeavor as is the disposal of high-level radioactive waste.

1.3 Research Objectives

So then, with the need to understand water transport processes, the principle objectives of this doctoral research is the modeling and analysis of thermally-induced water vapor production, transport, and removal at the drift-scale at the Yucca Mountain repository. Specifically, the goal is to expand on the many previously developed models to better understand what role:

(i) thermal radiation transport,

(ii) natural convection transport, and

(iii) evaporation transport processes

would have during the early postclosure phase on reducing/increasing relative humidity conditions near waste packages and along seepage-prone areas along the drift wall. These implementations will even further bound the expected conditions at Yucca Mountain, likely reducing the expectations for vapor condensation on waste canisters surfaces along with minimizing the likelihood of predicted seepage of percolation water into the drifts. This work contributes to the understanding of geological systems for use in the disposal of radioactive waste, a problem that as the time of the writing, has still yet to be solved and implemented by any of the world's nuclear states.

The remainder of this thesis is organized as follows: In Chapter 2, the TOUGH2 simulator used for the modeling effort is discussed in detail. Then, in Chapter 3, the models developed for radiation transport, and, in Chapter 4, the models for natural convection transport, are discussed. Following this, Chapter 5 covers the development and results of the Thermal-Hydrological seepage model, coupled with the previous developments, and is culmination of the research presented in this chapter. Finally, Chapter 6 discusses the model validation efforts and assumptions and ends with discussion of what future modeling efforts are envisioned for increased understanding of these processes at Yucca Mountain.

Chapter 2

A Simulation Code for Yucca Mountain Transport Processes: *TOUGH2v1.6*

2.1 Description

TOUGH2 is an integral-finite-difference numerical code that simulates non-isothermal flows of multicomponent, multiphase fluids in fractured and porous unsaturated media. Developed in 1991 by Karsten Pruess at Lawrence Berkeley National Laboratory (LBNL)[43], TOUGH2 is based on the MULKOM code developed by T. N. Narasimhan[44]. Its development was intended for applications in geothermal reservoir engineering, nuclear waste disposal, environmental assessment and remediation, and unsaturated and saturated zone hydrology and is now being used in areas of geologic storage of CO_2 (carbon capture and sequestration) and methane hydrate extraction.

TOUGH2 is also the simulator used for the thermal-hydrological (TH) models developed by the Earth Sciences Division at LBNL for scientific investigations into the disposal of radioactive waste at Yucca Mountain. Similarly, these models and TOUGH2 are the basis for the seepage models developed by the author (and in conjunction with with many others[1] during his graduate studies), the crux of the research represented in this dissertation. The following discussion is but a brief overview on structure and theory on TOUGH2, much more information on the program can be found in the official documentation[45].

[1]My scientific advisor, Dr. Jens T. Birkholzer, was instrumental in the development of my knowledge of numerical modeling and understanding of unsaturated zone transport.

2.2 Program Structure

TOUGH2 employs the same modular architecture as MULKOM, a research code from the early 1980's, and because the governing equations for all multiphase flow use the same mathematical form, TOUGH2 was assembled to allow the main flow in porous media and transport modules to operate independently of fluid property modules (equations of state - EOS), which define the thermodynamic properties of specific fluids. This allows the code an ability to handle many different types of multiphase and multicomponent transport systems.

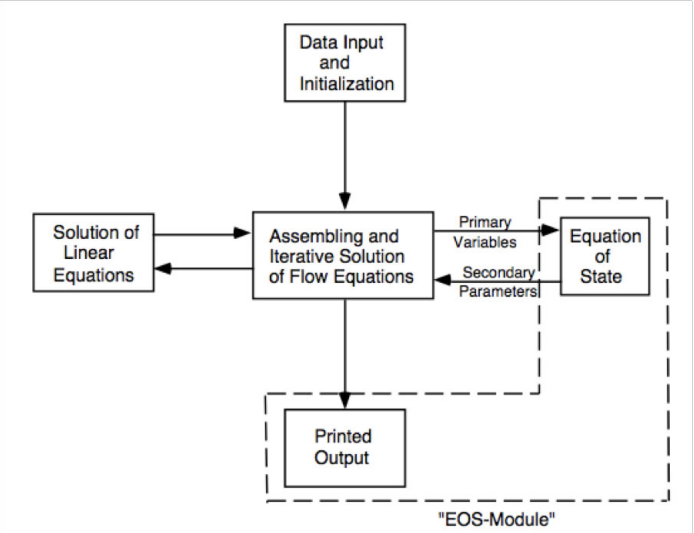

Figure 2.1: TOUGH2 program architecture (image from [45]).

TOUGH2 solves general energy and mass balance equations that describe multiphase, multicomponent heat and mass transport in a multi-dimensional porous system. Space discretization is performed using integral finite difference method (IFDM)[44], a method that does not convert the integral form of the general balance equations into partial differential equations. Benefits from this discretization procedure include:

(i) There is no need to reference a global coordinate system.

(ii) The use of regular and irregular discretization of meshes for any multi-dimensional system.

(iii) The ability to easily implement a multi-permeability model, allowing for modeling of transport in both fracture and matrix rock domains.

Time discretization is a first-order backward difference and is fully implicit, helping to achieve stability.

The IFDM discretization procedure results in a set of nonlinear algebraic equations with unknowns in the form of the time-dependent primary thermodynamic variables of the mesh elements. These equations are setup in residual form where

$$[\text{residuals}] = [\text{Right Hand Side}] - [\text{Left Hand Side}] = 0, \tag{2.1}$$

and are solved at the same time using Newton-Rhapson iteration. Time stepping is determined by the user and has options to be set to a fixed time, or can be automatically adjusted during simulation with a pre-established logic for convergence.

Data input and initialization results in the creation of two large 1-D arrays; one holds the primary thermodynamic variables for all mesh elements, and the other holds all secondary thermo-physical parameters needed for creation of flow and transport equations. Simulation proceeds with a computation of all residuals, with the largest residual checked for convergence. Achieving convergence results in an update of the the primary thermodynamic variables at the new time and the simulation continues. Otherwise, if convergence is not reached for the many reasons that it can, the time interval is reduced and the simulation is recalculated. Execution continues until a termination criteria is reached (i.e., maximum simulation time, maximum number of time steps, or if the automatically adjusted time steps reach a maximum value, indicating the system has reached steady-state).

2.3 Mass and Energy Balance

The general mass and energy balance equations that are solved by TOUGH2 are given as:

$$\underbrace{\frac{d}{dt}\int_{V_n} M^\kappa dV_n}_{\text{Volume Storage}} = \underbrace{\int_{\Gamma_n} \mathbf{F}^\kappa \bullet \mathbf{n}\, d\Gamma_n}_{\text{Normal Fluxes}} + \underbrace{\int_{V_n} q^\kappa dV_n}_{\text{Sources/Sinks}} \tag{2.2}$$

Equation (2.2) comprises an integration over some arbitrary volume subdomain V_n, bounded by a closed surface, Γ_n, and represents a common balance equation containing an accumulation term, boundary flow term, and a volume generation term. The indexing for mass and energy components is represented by κ (i.e., 1 = air, 2 = water, and 3 = heat), for a total of NK components. The LHS of eq. (2.2) is the volume storage term where M^κ represents the mass or energy per unit volume. The flux of heat and mass into and out of the volume represented by the vector $\mathbf{F}^\kappa$ through the bounding surface Γ_n, with $\mathbf{n}$ a unit normal vector pointing inward into the volume. Volume generation and losses (sources and sinks) is represented by q^κ, a rate per unit volume.

2.3.1 Volume Storage

The mass accumulation per volume term can be expressed in more detail as,

$$M^{\kappa} = \phi \sum_{\beta} S_{\beta} \rho_{\beta} X_{\beta}^{\kappa} \tag{2.3}$$

where the total mass for a component, κ, is the product of the porosity[2] of the volume element, ϕ, and the summation over the volume of the individual phases, β (i.e., gas, liquid) contained within that component. The volume of a phase, β, is the product of the phase saturation, S_{β} (fraction of pore volume occupied by phase β), the phase density, ρ_{β}, and the mass fraction of component κ in phase β, X_{β}^{κ}.

In a similar manner, the energy accumulation per volume term (κ = h) can be expressed as:

$$M^{h} = (1 - \phi)\, \rho_R C_R T + \phi \sum_{\beta} S_{\beta} \rho_{\beta} u_{\beta} \tag{2.4}$$

The total energy in the volume V_n is then the sum of two regions in the rock—the energy in the rock grain and the energy of the phases contained in the rock pores. The energy in the rock grain is the product of the volume of the rock $(1 - \phi)$, the rock density ρ_R, the rock specific heat C_R, and the absolute temperature of the volume, T. The energy contained in the fluid mixture stored in the rock pores is very similar to Equation (2.3), yet instead of summing mass fractions, we instead sum specific internal energies[3] of each phase u_{β}.

2.3.2 Boundary Fluxes

Flow of mass and energy into the volume, V_n , can represented by both advective and diffusive fluxes across the boundary surface, Γ_n.

[2]The *porosity* is the ratio of pore (void) volume V_v to the total volume of the material V_T, including void and solid volumes. $\phi = V_v / V_T$

[3]Instead of total enthalpy of the phase h_{β}, the internal energy of phase β is used. This simplification is valid when the energy associated with volumetric changes in the gas phase, caused by pressure changes, is small compared to the energy associated with temperature changes of the entire fluid mixture.

2.3.2.1 Advection

The advective mass flux for mass component κ is the summation over all the individual phase fluxes, $\mathbf{F}_\beta$, and can be expressed as,

$$\mathbf{F}^\kappa|_{\text{adv}} = \sum_\beta X_\beta^\kappa \mathbf{F}_\beta \tag{2.5}$$

The individual phase fluxes are then just the product of the phase density ρ_β and the Darcy velocity vector $\mathbf{u}_\beta$ (a volume flux),

$$\mathbf{F}_\beta \;=\; \rho_\beta \mathbf{u}_\beta \;=\; -k\frac{k_{r\beta}}{\mu_\beta}\left(\nabla P_\beta - \rho_\beta \mathbf{g}\right) \tag{2.6}$$

which can be further expanded by a multiphase version of Darcy's Law, accounting for flow contributions from both gradients of fluid pressures in phase β, ∇P_β, and also also gravity effects, $\mathbf{g}$. Resistances to flow of fluid through the rock, from both solid grain structure and the properties of the fluid itself, are accounted for with k being the absolute permeability of the rock, $k_{r\beta}$ the relative permeability to phase β, and μ_β the viscosity of the phase. The fluid pressure in phase β is,

$$P_\beta = P + P_{c\beta} \tag{2.7}$$

which includes contributions of both the pressure of a reference phase P (traditionally the gas phase) and the capillary pressure of the phase in the rock $P_{c\beta}$ (≤ 0). Vapor pressure lowering, a well-understood phenomenon allowing liquid water to exist in the small pore spaces at temperatures well above the boiling point[4], is accounted for by the use of Kelvin's equation:

$$P_v\left(T, S_l\right) = f_{\text{vpl}}\left(T, S_l\right) P_{\text{sat}}\left(T\right) \tag{2.8}$$

with the modified vapor pressure, P_v, being a function of the temperature, T, and the liquid saturation, S_l. It is calculated by reducing the saturated vapor pressure of the bulk liquid phase, P_{sat}, by a vapor pressure lowering factor, f_{vpl}, defined as,

$$f_{\text{vpl}} = \exp\left[\frac{M_w P_{cl}\left(S_l\right)}{\rho_l R\left(T + 273.15\right)}\right] \tag{2.9}$$

[4]Accounting for vapor pressure lowering in the modeling of Yucca Mountain is of great importance do to the extreme temperatures the fractured rock experiences after waste emplacement.

and is identical to the definition of relative humidity. P_{cl} is the difference between liquid and gas phase pressures (a function of the liquid saturation, S_l), M_w, the molecular weight of water and, R, the universal gas constant.

Also, heat flow through the boundary surface is given by,

$$\mathbf{F^h} = -\lambda \nabla T + \sum_\beta h_\beta \mathbf{F}_\beta \tag{2.10}$$

and includes heat transfer from both convective and conductive components. The conductive component includes the thermal conductivity of the total volume λ (rock-/fluid mixture) and the temperature gradient ∇T. Additionally, energy is transferred into the volume by all of the enthalpies of phase fluxes $\mathbf{F}_\beta$.

The thermal conductivity of the rock matrix is calculated using a square root interpolation, as a function of liquid saturation S_l,

$$\lambda\left(S_l\right) = \lambda_{\text{dry}} + \left(\lambda_{\text{dry}} + \lambda_{\text{wet}}\right)\sqrt{S_l} \tag{2.11}$$

with λ_{dry} the thermal conductivity of a completely dry sample[5] and λ_{wet} the thermal conductivity of a completely saturated sample.

2.3.2.2 Diffusion

Also, flow of mass and energy can occur by diffusion, given by

$$\mathbf{F}^\kappa|_{\text{diff}} = -\phi \sum_\beta \tau_0 \tau_\beta \rho_\beta d_\beta^\kappa \nabla X_\beta^\kappa \tag{2.12}$$

where $\tau_0\tau_\beta$ is the tortuosity including both a porous medium dependent factor τ_0 and factor dependent on phase saturation S_β, $\tau_\beta = \tau_\beta\left(S_\beta\right)$. The molecular diffusion coefficient, d_β^κ, is given for component κ in phase β, along with the driving potential for diffusive flow from the gradient of mass fraction of component κ in phase β, ∇X_β^κ.

[5]Interestingly, in the case of soil or rock, pore spaces contained therein can never be completely devoid of water. With decreasing saturation, the force due to capillary pressure eventually comes into balance with the vapor pressure, even at boiling temperatures. So then, to calculate *dry* heat conductivity of some soil type, a representative sample is baked in an oven at a temperature above the boiling point for some time until the change in weight of the sample changes little with time, ensuring that the water that can vaporize has done so.

2.3.2.3 Radiation

In addition to both the conductive and convective transfer of heat (as given in eq. (2.10)), heat transfer by thermal radiation can be defined using the Stefan-Boltzmann approximation for radiative transfer between any two gray bodies (n and m) of different temperatures, T_n and T_m,

$$\mathbf{F}^h\big|_{\text{rad}} = \epsilon\sigma_0 A\left(T_n^4 - T_m^4\right) \tag{2.13}$$

where ϵ is the emissivity of the material surface (assumed to be equal in eq. (2.13) for both bodies, n and m). The Stefan-Boltzmann constant is given as $\sigma_0 = 5.6687 \times 10^4$ J/m^{2}K^{4}s, and A is an arbitrary area over which the radiative transport takes place (explained in much greater detail in Chapter 3).

2.3.3 Sources and Sinks

Finally, for the integral sink/source term, $\int_{V_n} q^\kappa dV_n$ in the RHS of Equation (2.2), generation (production) and losses (drainage) for each component κ, q^κ, are represented simply by a volumetric rate (component/volume·time),

$$q^\kappa = \sum_\beta X_\beta^\kappa q_\beta^\kappa \tag{2.14}$$

where q_β^κ, is the volumetric rate of production/loss of component κ, in phase β. Similarly, the rate of heat (energy) removal or injection from the production/loss of each phase, β, is given by

$$q^h = \sum_\beta X_\beta^\kappa q_\beta^\kappa h_\beta^\kappa \tag{2.15}$$

where h_β^κ is the specific enthalpy of component κ in phase β.

2.3.4 Parameter relationships

All parameters used within the transport equations described previously have the advantage of holding constitutive relationships, in that TOUGH2 can express them all as a function of primary variables. This can occur through either the use of functional relationships (i.e., $f\left(T, P, P_{sat}\right)$) or from interpolation of lookup tables. Water vapor,

for instance, is described in TOUGH2 by the use of the steam table formulas given by the International Formulation Committee (IFC). Air (vapor and gas) is approximated as in ideal gas, with the total mixture pressure, $P_{mix} = P_{gas} + P_{vapor}$. Additionally, Henry's Law is used to calculate the solubility of gas in a liquid.

2.4 Integral Finite Difference Method

To begin, given two elements m and n (Figure 2.2), we assume that all quantities (e.g., temperature, pressure, density, etc.) within both elements are well averaged (i.e., there is no change in the value of any quantity at any location within the element).

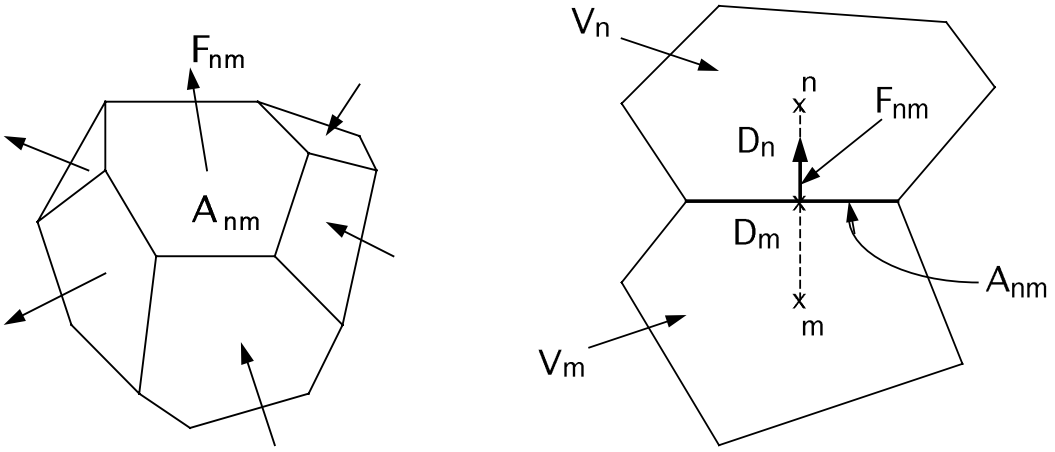

Figure 2.2: Arbitrary connecting elements in TOUGH2 mesh (image from [45]).

2.4.1 Space Discretization

Starting with the general mass and energy balance equation (eq. (2.2)), the volume accumulation term is approximated as,

$$\int_{V_n} M^\kappa dV_n = V_n M_n^\kappa \tag{2.16}$$

and M_n^κ is the volume averaged M^κ over volume V_n.

The surface flux term is approximated as the summation of all component fluxes into element m. The flux

$$\int_{\Gamma_n} \mathbf{F}^\kappa \bullet \mathbf{n}\, d\Gamma_n = \sum_m A_{nm} F^\kappa_{nm} \tag{2.17}$$

with F^κ_{nm} the averaged flux of component κ between elements m and n and the interfacial area between the two elements given by A_{nm}.

The Darcy flux term (eq. (2.6)), with the subscripts nm indicating a volume averaged parameter, can be written in a discretized manner as

$$F_{\beta,nm} = -k_{nm} \left[\frac{k_{r\beta}\rho_\beta}{\mu_\beta}\right]_{nm} \left[\frac{P_{\beta,n} - P_{\beta,m}}{D_{nm}} - \rho_{\beta,nm} g_{nm}\right] \tag{2.18}$$

with the effective distance between nodal points $D_{nm} = D_m + D_n$ and g_{nm} the component of gravitational acceleration between n and m (figure 2.2).

2.4.2 Time Discretization

Substituting the space discritized equations (eqs. (2.16) and (2.17)) into the mass and energy balance equation (eq. (2.2)) we have,

$$\frac{dM^\kappa_n}{dt} = \frac{1}{V_n} \sum_m A_{nm} F_{nm} + q^\kappa_n \tag{2.19}$$

a first-order ordinary differential equation in time.

Now, discretizing time as a first-order finite difference (k as time index), and evaluating the RHS of eq. (2.19) at the new time $t^{k+1} = t^k + \Delta t$ we have,

$$R^{\kappa,\,k+1}_n = M^{\kappa,\,k+1}_n - M^{\kappa,\,k}_n \frac{\Delta t}{V_n} \left\{ \sum_m A_{nm} F^{\kappa,\,k+1}_{nm} + V_n q^{\kappa,\,k+1}_n \right\} \tag{2.20}$$

$$= 0 \tag{2.21}$$

where we now have defined the residuals $R^{\kappa,\,k+1}_n$. For each volume element there are NEQ equations ($\kappa = 1,\, 2,\, \ldots,\, NEQ$) and NEL elements in the mesh resulting in a total of ($NEL \times NEQ$) unknowns for the primary independent variables x_i

$\{1, \ldots, NEL \times NEQ\}$, which completely define the flow system at time t^{k+1}. Newton-Raphson iteration (p as iteration index) is used to solve this set of equations. Using iteration index $p+1$, we expand the residuals $R_n^{\kappa,\,k+1}$ in a Taylor Series,

$$\begin{aligned} R_n^{\kappa,\,k+1}\left(x_{i,\,p+1}\right) &= R_n^{\kappa,\,k+1}\left(x_{i,\,p}\right) + \sum_i \left.\frac{\partial R_n^{\kappa,\,k+1}}{\partial x_i}\right|_p \left(x_{i,p+1} - x_{i,p}\right) + \ldots \\ &= 0 \end{aligned} \tag{2.22}$$

We drop all higher order terms in the expanded taylor polynomial resulting in a set of $NEL \times NEQ$ linear equations for the iteration range $(x_{i,\,p+1}, x_{i,\,p})$, which can be more simply written as,

$$-\sum_i \left.\frac{\partial R_n^{\kappa,\,k+1}}{\partial x_i}\right|_p \left(x_{i,p+1} - x_{i,p}\right) = R_n^{\kappa,\,k+1}\left(x_{i,\,p}\right) \tag{2.23}$$

2.4.3 Linear Equation Structure

Equation (2.23) can be expanded to matrix algebra in the form of a Jacobian matrix[6], with every partial derivative of the residual term, $\dfrac{\partial R_n}{\partial x_i}$, in the Jacobian matrix evaluated using numerical differentiation.

$$\overbrace{\left[\left.\frac{\partial R_n^{\kappa}}{\partial x_i}\right|_p\right]}^{\mathbf{J}} \bullet \overbrace{\left[x_{i,p+1} - x_{i,p}\right]}^{\mathbf{\Delta x}} = \overbrace{\left[\left. R_n^{\kappa}\right|_p\right]}^{\mathbf{R}} \tag{2.24}$$

The matrix is solved using either sparse direct matrix methods or iteratively using preconditioned conjugate gradient solvers. The Newton-Raphson iteration continues until every residual $R_n^{\kappa,\,k+1}$ reaches convergence tolerance, defined as,

$$\left|\frac{R_{n\,p+1}^{\kappa,\,k+1}}{M_{n\,p+1}^{\kappa,\,k+1}}\right| \leq \varepsilon_1 \tag{2.25}$$

where the default convergence criteria is set to a small value, e.g., $\varepsilon_1 = 10^{-5}$. If the convergence is not reached within a certain maximum number of iterations, the time interval Δt for the current time step is reduced and a new iteration sequence is started.

[6] A matrix of all first-order partial derivatives of a vector-valued function.

Chapter 3

Drift Thermal Radiation

3.1 Description

Any object or material above absolute zero constantly emits electromagnetic (EM) radiation across all spectrums due to the interaction—repulsion and attraction—of the charged particles (e.g., protons, electrons, ions and dipoles) of which it is composed. This EM radiation transports unabated through a vacuum and, upon collision with a molecule located in a recipient surface, has a probability of imparting its momentum, thus increasing the kinetic energies of the molecules with which it interacts. This average kinetic energy of the molecules of the material is quantifiable as the measurement of the material's temperature, so that if one surface absorbs more EM radiation than which it emits, its temperature will rise. Thermal radiation characterizes this implicit transport of kinetic energy from one surface to another via the emission, propagation, and absorption of EM radiation.

The decay heat of waste canisters (i.e., imparted kinetic energy transferred by both decay particles and EM radiation emitted from the decaying radioactive nuclei) gives rise to the increase in temperature of the waste canister material (e.g., fuel matrix, cladding, vitrified glass). As the temperature of the waste canister rises in comparison to the cooler drift wall, more thermal radiation is emitted from the waste canister and absorbed by drift wall than in reverse, resulting in an increase of the temperature of the drift wall. This specific mechanism of heat transfer was not explicitly considered in the many previous modeling studies investigating the in-drift environment at Yucca Mountain[26, 28, 29, 46, 47], and likely will have a unique role for the distribution of heat throughout the drift. It is thus is important to characterize its effects on temperature and moisture redistribution. This chapter discusses how thermal radiation was incorporated into the expanded TH models presented in chapters ahead and presents conceptual discussions for understanding the impact that thermal radiation has on the in-drift environment.

3.2 Comparison of heat transfer modes from Waste Package to Drift Wall

Temperature differences between the waste package and the surrounding environment not only drive heat transfer by radiation, but also induce natural convection flows, transferring heat through the circulation of warm air to the surrounding rock (continued discussion in Chapter 4). How do these two modes compare during different temperatures that exist during the repository operation? While the actual in-drift environment heat transfer processes are a multifaceted problem, we first look to a fundamental understanding by use of engineering approximations, specifically, we look to basic analytical models to compare both radiation and natural convection.

3.2.1 Simple natural convection approximation

Natural convection correlations between concentric cylinders—geometry similar to what exists at Yucca Mountain with the waste package and drift wall—were developed by Raithby and Hollands [48]. Assumed is that the increased rate of heat transfer due to natural convection within the tunnel can be approximated as a conductive process between two concentric cylinders of radii, r_i and r_o and temperatures T_i and T_o, respectively, as shown in Figure 3.1.

Following their methodology, the rate of heat transfer due to natural convection, per unit length, is given as,

$$q'_{\text{conv}} = \frac{q_{\text{conv}}}{L} = \frac{2\pi k_{\text{eff}} \left(T_i - T_o\right)}{\ln\left(r_o/r_i\right)} \qquad \left[\frac{\text{W}}{\text{m}}\right] \tag{3.1}$$

where the effective heat conductivity due to natural convection, k_{eff}, is given by the correlation,

$$\frac{k_{\text{eff}}}{k_{\text{gas}}} = 0.386 \left(\frac{Pr}{0.861 + Pr}\right)^{1/4} Ra_{L_c}^{1/4} \tag{3.2}$$

a function of both the Prandtl number, $Pr = \nu/\alpha$, and the Rayleigh number, R_{L_c}. In the case of vertical flow in concentric cylinders, the Rayleigh number is prescribed by

$$Ra_{L_c} = \frac{g\beta \left(T_i - T_o\right) L_c^3}{\upsilon\alpha} \tag{3.3}$$

where g is the gravitational force, β is the inverse of the average fluid temperature, υ is the kinematic viscosity[1], and α, the thermal diffusivity. The length parameter, L_c,

[1]Given as $\upsilon = \mu/\rho$, the kinematic viscosity is a ratio of the inertial forces to the viscous forces, an important parameter when considering transport by natural convection.

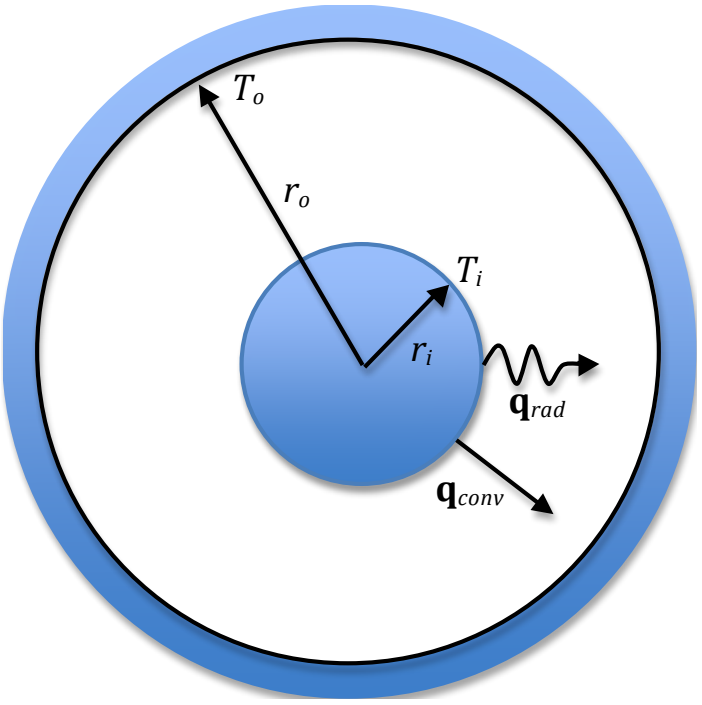

Figure 3.1: Concentric cylinder geometry used for approximating natural convection and radiation transport in a drift at the Yucca Mountain repository.

is given as

$$L_c = \frac{2\left[\ln\left(r_o/r_i\right)\right]^{4/3}}{\left(r_i^{-3/5} + r_o^{-3/5}\right)^{5/3}} \tag{3.4}$$

We further simplify eqs. (3.1) to (3.4) by combining and reducing them to the form of eq. (3.1), having only a dependency on the temperature difference, $(T_i - T_o)$ given as,

$$q'_{\text{conv}} = \frac{q_{\text{conv}}}{L} = C_{\text{conv}}\left(T_i - T_o\right)^{5/4} \tag{3.5}$$

a function slightly non-linear for small temperature differences, with constant C_{conv}, given as,

$$C_{\text{conv}} = C_q C_k C_{Ra}^{1/4} L_c^{3/4} \tag{3.6}$$

where the individual constants are further defined as,

$$C_q = \frac{2\pi}{\ln\left(r_o/r_i\right)} \qquad [-] \tag{3.7a}$$

$$C_k = 0.386\left(\frac{Pr}{0.861+Pr}\right)^{1/4} k_{\text{gas}} \qquad \left[\frac{\text{W}}{\text{mK}}\right] \tag{3.7b}$$

$$C_{Ra} = \frac{g\beta}{\upsilon\alpha} \qquad \left[\frac{1}{\text{m}^3\text{K}}\right] \tag{3.7c}$$

3.2.2 Simple radiation approximation

Expanding on the previously defined eq. (2.13), for a sufficiently long configuration (i.e., $F_{o\to i} \sim 1$), radiative heat emitted by an enclosed cylinder can be represented as,

$$q'_{\text{rad}} = C_{\text{rad}}\left(T_i^4 - T_o^4\right) \qquad \left[\frac{\text{W}}{\text{m}}\right] \tag{3.8}$$

a function with a highly non-linear response to temperature differences between the inner and out cylinders, with the constant, C_{rad}, given as

$$C_{\text{rad}} = 2\pi r_i \epsilon \sigma_0 \tag{3.9}$$

where ϵ is the emissivity of the material of the inner cylinder and σ_0 is the well-known Stefan-Boltzmann constant, $\sigma_0 = 5.6704 \times 10^{-8}$ W/m^{2}K^4.

3.2.3 Ratio of radiative to convective heat transfer

Finally, we are able to define the ratio of radiative to convective heat transfer, $\eta = q_{\text{rad}}/q_{\text{conv}}$, by dividing eq. (3.8) by eq. (3.5) resulting in

$$\eta = \frac{C_{\text{rad}}}{C_{\text{conv}}}\frac{\left(T_i^4 - T_o^4\right)}{\left(T_i - T_o\right)^{5/4}} \tag{3.10}$$

where T_i and T_o are absolute temperatures in unit Kelvin. Equation (3.10) is a function that, when used to analyze the configuration of a drift at Yucca Mountain, is dependent on only the temperature of the drift wall, T_{dw}, and the temperature of the waste package surface, T_{s}. When radiative transfer is larger than that of natural convection, $\eta > 1$, conversely, if natural convective heat transfer is dominate, $\eta < 1$.

For average conditions expected at Yucca Mountain, we assume the thermodynamic properties of air for a selected average gas temperature of $T_{\text{gas}} = 177°\text{C}$ (Table 3.1), the emissivity of waste canister surface to be that of stainless steel at 350 K ($\epsilon_{T_{\text{s}}\sim 350\,K} =$

Table 3.1: Thermodynamic properties of air at temperature, $T_{\text{gas}} = 177°\text{C}$ (450K).

Parameter	Units	Symbol	Value
Thermal conductivity	$W/m\,K$	k_{gas}	0.0363
Density	kg/m^3	ρ_{gas}	0.784
Dynamic viscosity	$kg/m^2\,s$	μ_{gas}	2.49×10^{-6}
Kinematic viscosity	m^2/s	ν_{gas}	3.18×10^{-5}
Thermal diffusivity	m^2/s	α_{gas}	4.45×10^{-5}
Prandtl number	–	Pr	0.7
Inverse average temperature	$1/K$	β_{gas}	2.22×10^{-3}

0.22) and along with the dimensions of waste package and drift given as $r_{\text{s}} = 0.3\,\text{m}$ and $r_{\text{dw}} = 2.25\,\text{m}$, we solve for constants in eq. (3.10) as,

$$\frac{C_{\text{rad}}}{C_{\text{conv}}} = 1.074 \times 10^{-8} \quad \left[\frac{\text{K}^{5/4}}{\text{K}^4}\right] \tag{3.11}$$

To more easily comprehend the function response during varying modes of drift operation, we transform the multi-parameter dependency of $\eta\left(T_{\text{s}}, T_{\text{dw}}\right)$ in eq. (3.10) as,

$$\eta\left(T_{\text{s}}, T_{\text{dw}}\right) \longrightarrow \eta\left(T_{\text{avg}}, \frac{T_{\text{s}} - T_{\text{dw}}}{\Delta T_{\text{max}}}\right) \tag{3.12}$$

where the average temperature between the waste canister surface and drift wall, T_{avg}, is given by $T_{\text{avg}} = \left(T_{\text{s}} + T_{\text{dw}}\right)/2$, and the non-dimensional temperature parameter, $\left(T_{\text{s}} - T_{\text{dw}}\right)/\Delta T_{\text{max}}$, relates the temperature difference to maximum temperature differences and is restricted to values $0 < \frac{T_{\text{s}} - T_{\text{dw}}}{T_{\text{max}}} \leq 1$.

Assuming the maximum temperature difference to be $\Delta T_{\text{max}} = 10°\text{C}$, the heat transfer ratio η is plotted in figure 3.2 for different average temperatures ($T_{\text{avg}} = 50°\text{C}$, 90°C, and 130°C), along an axis of dimensionless temperature difference, $\left(T_{\text{s}} - T_{\text{dw}}\right)/\Delta T_{\text{max}}$. For the case when $T_{\text{avg}} = 130°\text{C}$, it is observed that η is always greater than the results for lower average temperatures (i.e., green line ($T_{\text{avg}} = 130°\text{C}$) is above red line ($T_{\text{avg}} = 90°\text{C}$) which is above the blue line ($T_{\text{avg}} = 50°\text{C}$)). This shows that high average temperatures in this type of configuration always result in a larger portion of heat transfer occurring by radiative transport, a property of blackbody emissive power being related to temperature by $Q_{\text{blackbody}} \sim T^4$.

Similarly, when observing the response due to temperature differences, a general trend exists showing that as temperature differences become smaller, $\frac{T_{\text{s}} - T_{\text{dw}}}{\Delta T_{\text{max}}} \longrightarrow 0$, the rate of radiative heat transfer becomes larger, doing so rapidly as the temperature difference approaches zero. For example, when $\frac{T_{\text{s}} - T_{\text{dw}}}{\Delta T_{\text{max}}} = 0.1$ in the $T_{\text{avg}} = 130°\text{C}$ case

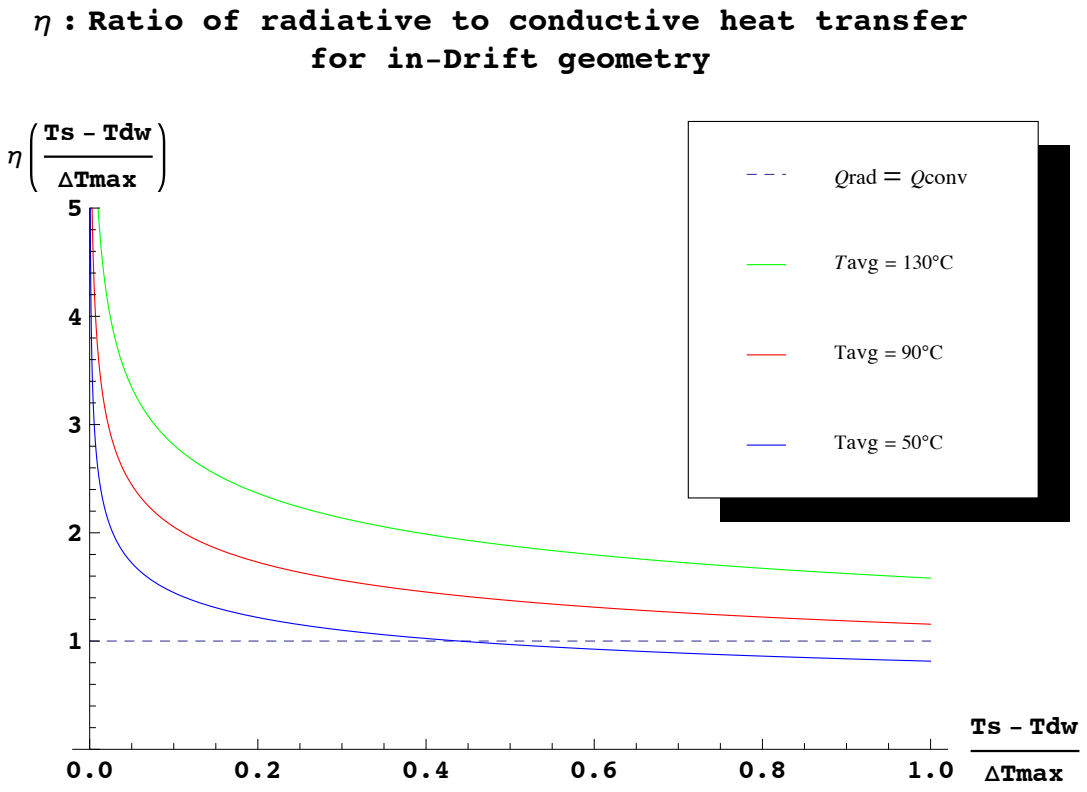

Figure 3.2: Ratio of radiative heat transport and convective heat transport, η for concentric cylinder-in-cylinder geometry, similar to that of Yucca Mountain, for average temperatures T_{avg} of 50°C, 90°C, and 130°C and varying temperature differences, $\frac{T_{\text{s}} - T_{\text{dw}}}{\Delta T_{\text{max}}}$, and with $\Delta T_{\text{max}} = 10$°C.

(where $T_{\text{s}} = 130.5$°C and $T_{\text{dw}} = 129.5$°C), the resulting value for radiative to convection heat transfer is $\eta \sim 3$, meaning that radiative heat transfer is responsible for 75% of the transport to the drift-wall, a considerable contribution. At the same temperature difference, however, in the alternate case of $T_{\text{avg}} = 50$°C, the ratio is $\eta \sim 1.5$, or 60% of transport is by radiation.

When temperature differences are larger, $\frac{T_{\text{s}} - T_{\text{dw}}}{\Delta T_{\text{max}}} \longrightarrow 1$, the radiative heat transfer contribution to overall heat transfer is reduced. The high average temperature, $T_{\text{avg}} = 130$°C, results in a radiative transport of about twice that of convective transport, while in the case for $T_{\text{avg}} = 50$°C, natural convection is the dominant mode, accounting for just over 50% of the total heat transport.

This basic engineering approximation reveals that heat transport by radiation is clearly an important mode of heat transfer for geometric configurations similar to Yucca Mountain, and has a

(i) larger role during times of higher average temperatures, and also is the

(ii) dominant mode of heat transfer when temperature differences are smaller, regardless of average temperature.

As such, to better capture the thermohydrological response of the in-drift environment during heated conditions at Yucca Mountain, thermal radiation transport should be modeled and represented by at least a basic approximation, which is further described below.

3.3 Modeling Thermal Radiation in a drift

In reality, the transport of thermal radiation is a complex process involving many material and surface properties that impact its behavior. Various advanced modeling options exist for capturing the effects of such details, however, for use in the modeling of the Yucca Mountain repository—where transients in the fractured rock (i.e., temperature and saturation) and transients in the decay heat source are relatively slow—simpler efforts are appropriate. Radiation transport can be sufficiently approximated by use of the well-known *Stefan-Boltzmann Law*, modeled as the difference in the emissive power between two surfaces in radiative exchange. While our discussion earlier as to the significance of radiative heat transport used the *Stephan Boltzmann Law*, it was but for a simple configuration which considered the radiation transport between the entire waste canister to the entire drift wall in a single representation. In most systems, including Yucca Mountain, *many* surfaces of varying spatial orientations, dimensions, temperatures and thermal characteristics can be in radiative exchange.

To incorporate such relationships, we expand on the concepts for radiative transfer by considering some surfaces n and m of finite areas dA_n and dA_m, such as those shown in Figure 3.3. Assuming diffusive[2] emission from both surfaces, there exists a certain ratio of the radiation emitted by surface n that is intercepted by surface m, something that must be accounted for when calculating the radiative transfer between them both. As such, we modify the previously given eq. (2.13) to include this ratio and rewrite it as,

$$\boxed{q_{\text{rad},n\to m} = \epsilon\sigma_0 F_{n\to m} A_n \left(T_n^4 - T_m^4\right)} \tag{3.13}$$

where $F_{n\to m}$ is the fraction of radiative energy leaving the surface of body n that is intercepted by the surface of body m, and is commonly referred to as the radiative view factor. With this, Equation (3.13) is the governing equation for thermal radiation transport between interacting surfaces in TOUGH2.

[2] A *diffusive* emission approximation assumes that emissivity and absorptivity of the material or surface are constant with regards to temperature, spectral angle, and wavelength of radiation emitted or received.

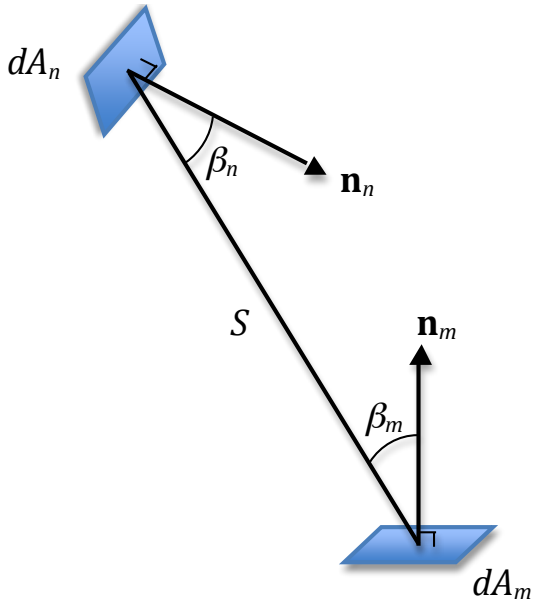

Figure 3.3: Two finite grey surfaces of area dA_n and dA_m oriented uniquely in space, and separated from one another by some distance S, with angles to normals vectors, $\mathbf{n}_n$ and $\mathbf{n}_m$, given by β_n and β_m.

3.3.1 Solving for the View Factor

Consider radiant exchange of thermal energy between two finite grey[3] surfaces, n and m, as those shown in Figure 3.3. The view factor (also know as shape, configuration, or geometric factor), $F_{n\to m}$, defines the amount of radiant energy emitted by n that is intercepted by m. $F_{n\to m}$ is based strictly on a geometrical concept and depends only on the shape, size and orientation of the two surfaces in space. It can vary between values of 0 (implying that none of the energy emitted by surface n is intercepted by surface m) and 1 (all energy emitted is intercepted), and can be defined analytically using solid angle calculus (for sake of brevity not derived here, see Section 10.3 of [49]). This derivation results in

$$F_{n\to m} = \frac{1}{A_n}\int_{A_n}\int_{A_m} \frac{\cos\beta_n \cos\beta_m}{\pi S^2} dA_n dA_m \tag{3.14}$$

a double integration where β_n and β_m are angles to the normals of both surfaces, $\mathbf{n}_n$ and $\mathbf{n}_m$, to the distance, S. The analytical calculation of the view factor can be a difficult problem when the geometry is anything but simple, involving complex integrations that must be solved numerically for most surface relations.

[3]Grey bodies/surfaces are not perfect blackbodies and therefore do not absorb or emit as a blackbody would and have therefore, a specific emissivity and absorptivity value < 1.

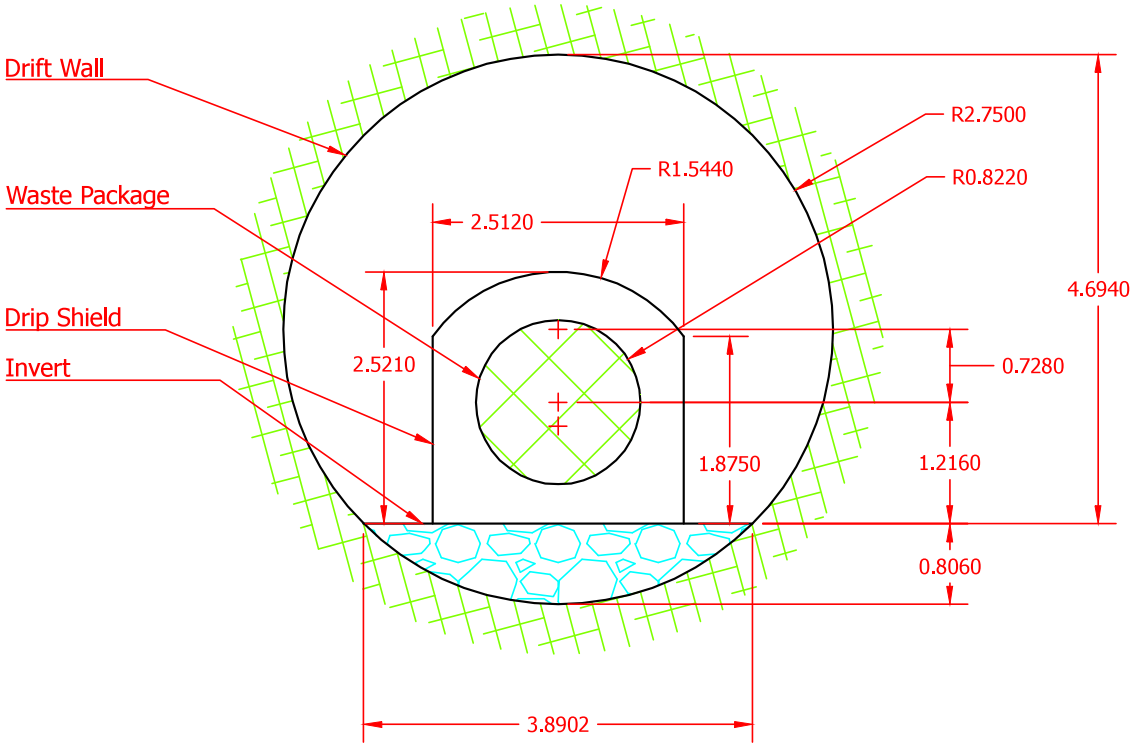

Figure 3.4: In-drift geometry and dimensions (in units meters) at the Yucca Mountain repository.

The specific dimensions of the in-drift geometry at Yucca Mountain, as depicted in Figure 3.4, also represent a complex problem (i.e., the analytical relationship between the hotter radiating surfaces of either the waste package or drip shield and the drift wall and invert) for which no analytical solution exists for calculation of view factors using eq. (3.14). Instead, the double integration of the unique inner function, $\cos\beta_n \cos\beta_m / S^2$, was solved using numerical methods from a custom program written in Fortran 95. The in-drift mesh elements that composed the surfaces that would be involved in thermal radiation transport were discretized into a number of smaller element areas, $i \times j$. Refining the trapezoidal-rule, numerical algorithms were used for integration. Using the program, the surface to surface distance S is calculated as a distance between Cartesian coordinates in three dimensions, and sub-element to sub-element view factor calculations were performed by calculating eq. (3.14) many times across a set number of element increments, and later summed to give the total view factor from some element n to some element m as,

$$\sum_i \sum_j F_{n_{i,j} \to m_{i,j}} = F_{n \to m} \tag{3.15}$$

increasing the accuracy of the view factor calculation by numerical approximation.

3.3.2 Implementation in TOUGH2 models

To establish the analytical definitions for the parameters required in eq. (3.14), we again consider a case where radioactive exchange occurs between two surfaces, n and m, however this time specifically to the in-drift geometry at Yucca Mountain. Specifically, we look to describe

(i) S, the distance between a point, D, on the waste package/drip shield surface, and a point B, on the drift wall, and also

(ii) β_n and β_m, the angles between the normals and S

as functions dependent on the locations along the waste canister/drip shield and drift wall surfaces in three dimensions. We begin by defining two angular coordinate systems, θ and ϕ, used to further define geometric relationships between the waste package and the drift wall. We let θ be the angular displacement around the shared geometric center of the drip shield and the waste package, and ϕ the angular displacement around the geometric center of the drift tunnel (labeled as points F and A in Figure 3.5, respectively).

Looking at $\triangle AFD$ in figure 3.5, we solve for L, the distance between the center of the drift and the inner heated radiating surface (waste package surface or drip shield) at any angle, θ, using the *Law of Cosines* as

$$L(\theta) = \left(r^2 + h^2 + 2rh\cos\theta\right)^{1/2} \tag{3.16}$$

where h is the offset between the center of the waste package and the center of the drift, a constant value, and represented by distance AF in figure 3.5. For use in the TH models of Yucca mountain, the heated surface radius, represented by r, could be either the drip shield radius, r_{ds}, or the waste package radius, r_{wp}. We can again use *Law of Cosines* on $\triangle AFD$ to solve for γ_n as

$$\gamma_n(\theta) = \cos^{-1}\left(\frac{h^2 + L(\theta)^2 + r^2}{2h\,L(\theta)}\right) \tag{3.17}$$

and also, simply by summing angles in $\triangle ADB$, we can solve for γ_m as

$$\gamma_m(\theta,\phi) = \left|\pi - \phi - \gamma_n(\theta)\right| \tag{3.18}$$

Having this angle defined, we can finally solve for the length S using law of cosines in $\triangle ADB$, by writing

$$S(\theta,\phi) = \left(r_{\mathrm{dw}}^2 + L(\theta)^2 - 2r_{\mathrm{dw}}L(\theta)\cos\gamma_m(\theta,\phi)\right)^{1/2} \tag{3.19}$$

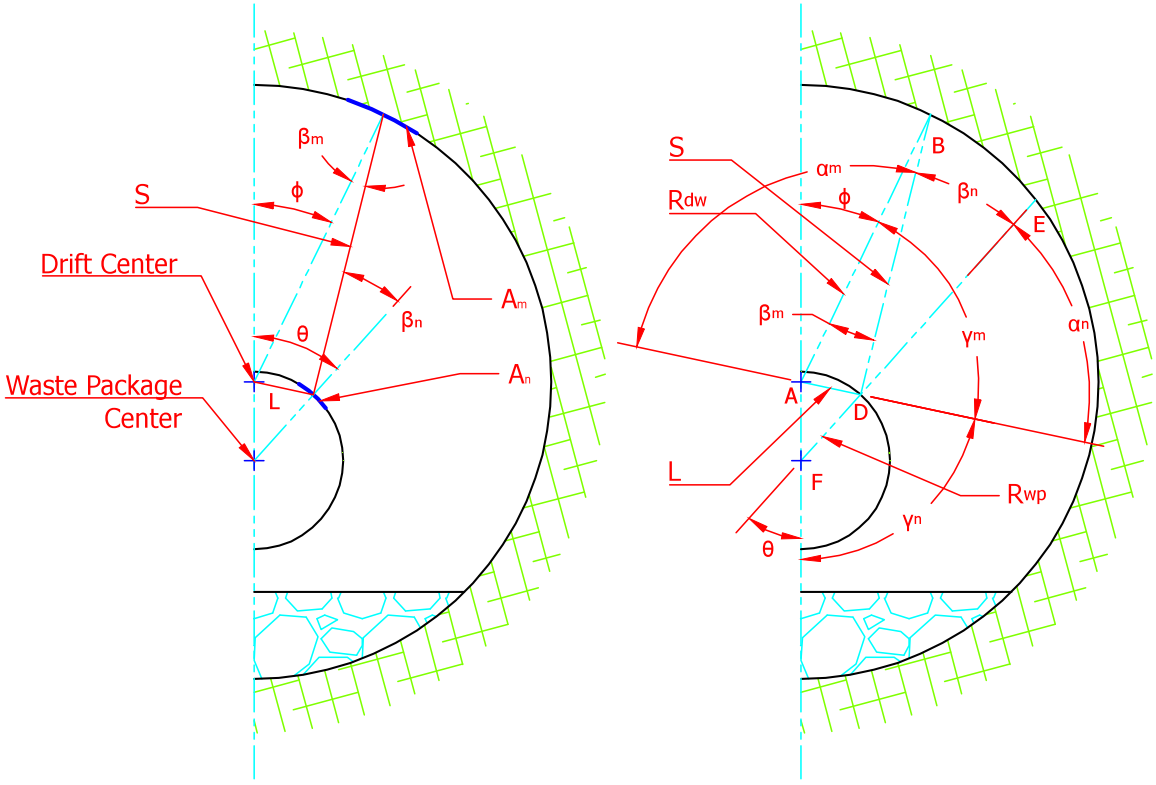

Figure 3.5: *Left*: Representative parameters of in-drift geometry at the Yucca Mountain repository for view factor calculation in Equation (3.27), with representative surfaces, A_n and A_m, for thermal radiation transport. *Right:* Further definition of geometric relations used in derivation of necessary parameters for use in Equation (3.27).

With S defined, we have the length of a second side in $\triangle ADB$ and can now also solve for β_m as

$$\beta_m(\theta,\phi) = \cos^{-1}\left(\frac{r_{\text{dw}}^2 + S(\theta,\phi)^2 - L(\theta)^2}{2r_{\text{dw}}S(\theta,\phi)}\right) \tag{3.20}$$

The total sum of angles in $\triangle AFD$ is equal to π, so we can solve for α_n as

$$\alpha_n(\theta) = \left|\pi - \gamma_n(\theta) - \theta\right| \tag{3.21}$$

and similarly, one can solve for α_m by maintaining the sum of angles in $\triangle ADB$ as

$$\alpha_m(\theta,\phi) = \left|\pi - \beta_m(\theta,\phi) - \gamma_m(\theta,\phi)\right| \tag{3.22}$$

Both these angles, α_m and α_n are centered around point D, and when considering summation of total angles around this point in reference to the line segment AD, we

can solve for the final angle, β_n, as

$$\beta_n(\theta, \phi) = \left|\pi - \alpha_n(\theta) - \alpha_m(\theta, \phi)\right| \tag{3.23}$$

These equations, eqs. (3.19), (3.20) and (3.23), together represent the analytical relations for 2D in-drift geometry, however, when considering a third dimension, at some distance z in the axial direction away from the drip shield, we can solve for the 3D distance, S_z, as

$$\boxed{S_z(\theta, \phi, z) = \left(z^2 + S(\theta, \phi)\right)^{1/2}} \tag{3.24}$$

Similarly, using concepts of plane projection of right triangles and knowing the distance, z, along the axial direction, we can solve for the angles between the length, S_z, and normals, as

$$\boxed{\beta_{m_z}(\theta, \phi, z) = \sin^{-1}\left(\frac{\sin\left(\beta_m\right) S}{S_z}\right)} \tag{3.25}$$

$$\boxed{\beta_{n_z}(\theta, \phi, z) = \sin^{-1}\left(\frac{\sin\left(\beta_n\right) S}{S_z}\right)} \tag{3.26}$$

With the analytical relations for in-drift geometry defined as functions θ, ϕ, and z, we can substitute $A_n = r_n z_n \, d\theta$ and $A_m = r_m z_m \, d\phi$, and rewrite eq. (3.14) in terms of these new parameters, as

$$\boxed{F_{n\to m}(\theta, \phi, z) = \frac{r_m}{\pi d\theta dz_n} \int_{dz_n} \int_{dz_m} \int_{d\phi} \int_{d\theta} \frac{\cos\beta_n \cos\beta_m}{S_z^2} \, d\theta \, d\phi \, dz_n \, dz_m} \tag{3.27}$$

where z is some length in the axial direction; r_m is the radius of surface m (the drift wall in this example); and $d\theta$ and $d\phi$ are the angle increments and dz_n and dz_m the axial increments that bound areas A_n and A_m, respectively.

With these solutions, Equations (3.24) to (3.26) are then used in conjunction with the numerical solution to eq. (3.27) to calculate view factors for the meshes used in both the *natural convection model*, and also the *seepage model*[4] (explained in greater detail in Chapter 4 and Chapter 5, respectively). The view factors are then weighted

[4]For calculating view factors for use in the *seepage model*, whose in-drift mesh region was much more detailed then that used in the *nat-co* model, initial results from the view factor numerical calculation resulted in regions with anomalous values (i.e., discontinuous and fluctuating, in what should have been an otherwise continuous and smooth distribution for view factor values). Although a discussion is well beyond scope of this dissertation, significant research into the issue found that the quadrature solution to the view factor integral in eq. (3.14) was suffering from a well-known numerical artifact referred to as the *ray effect*[50]. As such, the calculation of view factor values in this model were assisted with the use of an over-the-counter thermal radiation package, RadCAD[51, 52], which uses a Monte-Carlo method of ray-tracing, a procedure that can employed to calculate radiative

into a special constant used by *TOUGH2*, including the emissivity and area of emitting surface, in a list of unique connections between emitting and receiving elements. For simplification of the calculations, drift wall to drift wall connections were never considered—an appropriate assumption as the largest temperature differences (and therefore the largest rates of radiative heat transfer) exist between the waste package/drip shield surfaces and the drift wall. It is noted that once a radiative connection has been established between any two elements, radiation can transport in either direction, depending on whichever surfaces has the highest temperature.

3.4 Understanding the impact of 3D radiative heat transport, a simple discussion

In order to understand the significance that thermal radiation might have on the in-drift environment outside of a full model simulation, we will consider a simple scenario by which the effects of three-dimensional radiation would be important. As the waste packages to be placed in Yucca Mountain will contain various waste streams, the radioactive content contained within them will have different radionuclide compositions, and so will also display different decay heat outputs[53], such as the difference between a *hot* 21-PWR waste canister (having an initial decay heat output of 1.1 kW/m), and the *cool* 5-HLW waste canister (having an initial decay heat output of 0.085 kW/m)[54], shown ahead in Figure 4.6. With this large range of decay heat outputs, we can consider a scenario where a *cool* 5-BWR waste canister is placed next to a *hot* 21-PWR waste canister and see what effects radiation would have on heat transport to the drift wall via thermal radiation, as depicted in Figure 3.6.

Assuming each of the waste canisters has equal dimensions, with canister radius $r_{\text{wp}} = 0.822\,\text{m}$, canister length, $l_{\text{wp}} = 5.25\,\text{m}$, and with gap spacing $l_{\text{gap}} = 0.1\,\text{m}$, we use the 3D view factor numerical integration code described previously to calculate the view factors from waste packages to varying drift wall layer. Being that the geometry for each waste canister is equal in our example, view factor results will be equal across many canisters and therefore it is sufficient tocalculate view factors from a single canister. Specifically, we calculate the view factor from the waste canister to the drift wall in the same layer and find that $F_{\text{wp}|_i \to \text{dw}|_i} = 0.755$, and also to an adjacent drift wall layer, resulting in $F_{\text{wp}|_i \to \text{dw}|_j} = 0.111$. These values can be interpreted by observing that of the total heat radiation emitted by a waste package in any layer, a little over 75% is intercepted by the drift wall in the same layer. Similarly, a little over 10% of the thermal radiation emitted by a waste package is intercepted by the two adjacent drift wall layers and when combined together (the drift wall surfaces in the same and adjacent areas) represent the surfaces that intercept 97.7% of the energy emitted by a single waste canister.

view factors with high precision with the need for numerical intergration, albeit a computationally intensive process.

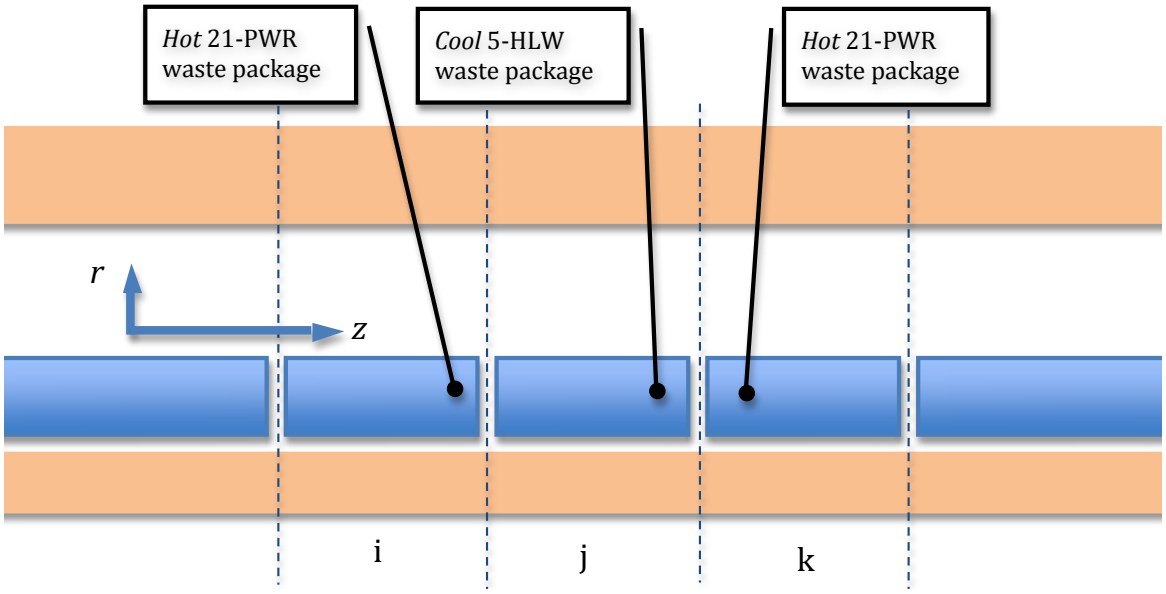

Figure 3.6: A cross-axial view for example waste emplacement configuration, with a *cool* 5-HLW waste package residing between to *hot* 21-PWR waste packages.

To conceptualize how thermal radiation affects adjacent layers, we simply calculate the transport of thermal radiation to direct and adjacent drift wall layers (assuming 1/2 of the total heat transport from the waste package to the drift wall occurs by radiation transport). First, we begin with a *hot* 21-PWR waste canister as,

$$0.5\,(1.1\,\mathrm{kW/m})\,(5.25\,\mathrm{m})\,(0.755) = 2.18\,\mathrm{kW}$$
$$0.5\,(1.1\,\mathrm{kW/m})\,(5.25\,\mathrm{m})\,(0.111) = 0.32\,\mathrm{kW}$$

and similarly for the *cool* 5-BWR waste canister as,

$$0.5\,(0.085\,\mathrm{kW/m})\,(5.25\,\mathrm{m})\,(0.755) = 0.17\,\mathrm{kW}$$
$$0.5\,(0.085\,\mathrm{kW/m})\,(5.25\,\mathrm{m})\,(0.111) = 0.025\,\mathrm{kW}$$

These results are significant—the radiative heat transfer from a *hot* 21-PWR waste canister to the drift wall in an adjacent layer containing a *cool* 5-BWR waste canister is over an order of magnitude larger (0.32 kW) than the radiative heat transfer from the *cool* 5-BWR waste canister to the drift wall in the same layer (0.17 kW). Considering the mechanisms of radiative transport, three-dimensioal radiative heat transfer would always contribute to a smoothing of the temperature profile along the drift axis. In general, this would work to prevent any region from having any significant change in temperature from nearby regions—an aspect beneficial in terms of the reduced

possibility for vapor condensation on cooler waste packages—concepts that are further developed in the chapters to come.

Chapter 4

Drift Natural Convection

The previous chapter discussed how temperature differences between surfaces drive heat transport by thermal radiation, a process shown to contribute significantly to the heat distribution within the in-drift environment for an emplacement tunnel at the Yucca Mountain repository. Beyond such variation of surface temperatures, also existing within a heated system can be regional temperature differences in a fluid surrounding such surfaces, which, along with differences in chemical concentrations or material phases in such a fluid, result in density gradients across the bulk fluid volume. These density differences can then be acted upon by external force fields producing a buoyancy-induced flow within the system—a transport process referred to as natural convection. For the in-drift environment of an emplacement tunnel at Yucca Mountain, these buoyancy-induced flows occur when density differences in the in-drift air—due to thermal and vapor mass fraction gradients—are acted upon by gravity, resulting in the transport of heat and moisture within the open air spaces of the emplacement tunnel. What impacts these flow processes might have on the redistribution of heat and saturation in the fractured rock is explored in this chapter.

4.1 Expected Thermal-Hydrological Processes in the Near-Field

The desire to understand such processes in regard to waste emplacement at Yucca Mountain is not new, as many modeling studies have been conducted to understand in-drift transport[37, 38, 55]. The goals of these modeling studies were each different, however, each revealed important transport processes that would heavily impact the moisture conditions of the surrounding fractured rock.

Webb and Itamura et al. developed a detailed computational fluid dynamic (CFD) simulation of a section of the in-drift to explore the effects of natural convection

Table 4.1: Previously calculated effective mass dispersion coefficients[55], and those used in these simulations.

	Effective Diffusivity for different times [m^2/s]			
Cases	**300 years**	**1000 years**	**3000 years**	**Value used in model (all times)**
Case 1: Temperature gradient (strong convective mixing)	0.1	0.1	0.1	**0.1**
Case 2: No temperature gradient (moderate convective mixing)	0.008	0.004	0.004	**0.004**
Case 3: Comparison case (binary diffusion only)	–	–	–	$\mathbf{2.14 \times 10^{-5}}$

within the heated emplacement tunnel[55]. Their model consisted of a 70 m long section of emplacement tunnel, containing heat generation from an average collection of the waste package types to be expected at Yucca Mountain. Considering *only* temperature differences for the density gradients that would drive buoyancy-induced transport (one could have also considered effects of chemical concentration gradients with the inclusion of water vapor into the bulk fluid), their simulations revealed the formation of natural convection cells, in both the radial (as shown in Figure 4.1) and axial directions, with the gas velocities on the order of ∼2 cm/s.

Depending on the temperature gradient that might exist along this 70 m section of tunnel (0°C or 4°C), these natural convection cells result in moderate or strong rate of bulk transport of air from the tunnel center to the drift turnout. They then used the results of the CFD flow fields to calculate an effective dispersion coefficient, later used in a separate, one-dimensional, semi-analytical, binary diffusion model to study the amount of vapor transport along the drift (shown in Table 4.1). Their results showed the importance of these turbulent natural convective processes on the transport of vapor from the heated tunnel centers to the cooler drift end, however, did not include the important feedback of the vapor source from the heated fractured rock mass, instead employing a pre-defined boundary condition at the drift wall.

When considering results for the expected in-drift transport processes, from studies such as this, combined with the knowledge previously garnered about the behavior of the surrounding fractured rock mass, we can tie together both domains to paint a conceptual picture of how both might impact one another.

4.1.1 In the Fractured Rock surrounding the Emplacement Drift

A majority of all decay heat emitted from the waste packages will be effectively transferred to the drift walls and into the near-drift formation[46]. As shown in the previous chapter, thermal radiation is a dominate mode of heat transport within the drift, while the complex processes of conduction and convection will be most important in the fractured rock. As the partially saturated formation near the drifts heats up to above-boiling temperatures, the initially mostly-stagnant pore water in the matrix will become mobile through vaporization. With this liquid to gas phase change a significant pressure increase occurs, driving the vapor from the matrix to the highly permeable fractures— pervasive throughout the geology at Yucca Mountain— where it can transport away from the boiling region. The vapor production and transport during this time results in a hot dryout zone that forms around the heated emplacement tunnels—a desaturated region with little or no amount of liquid water present (observed in many studies[22, 23, 28, 47]).

Because of the gas flow communication between an emplacement tunnel and (i) the main access tunnels and (ii) the large volume of permeable fractured rock, it can be assumed that the gas pressure within the drifts would remain at atmospheric conditions. So then, of the vapor that flees the higher-pressure boiling region, a portion will also be driven into open air spaces in the drifts, increasing the concentration of vapor in such heated sections. The remaining volume of the vapor will move away through the unobstructed fracture network in the direction of the pressure gradient (radially away from the heated drift) into the cooler rock regions where it will eventually condense on the fracture walls. This scenario gives rise to many interesting transport processes in the fractured rock including the formation a geologic heat pipe—an effective form of heat dissipation. Condensation of cooled vapor on fracture walls is imbibed into the matrix structure due to the stronger capillarity of that domain and is further driven towards the dryout zone due to capillary forces where it is again vaporized upon its entrance into the boiling region.

Condensation, as such, could also contribute to an increase in liquid fluxes in the fracture domain, especially during times of cooling, and is of concern for repository performance due to potential for thermal seepage (discussed more in section 5.2.2.2). At later times, as the rock temperature has returned to below boiling conditions, the constant percolation flux results in the gradual rewetting of the rock mass near the drifts (Figure 4.2b). For drifts with average temperature conditions, rewetting will occur roughly a few hundred years after boiling has ceased[27], still however, due to elevated temperatures, natural convection will play an important role during these times.

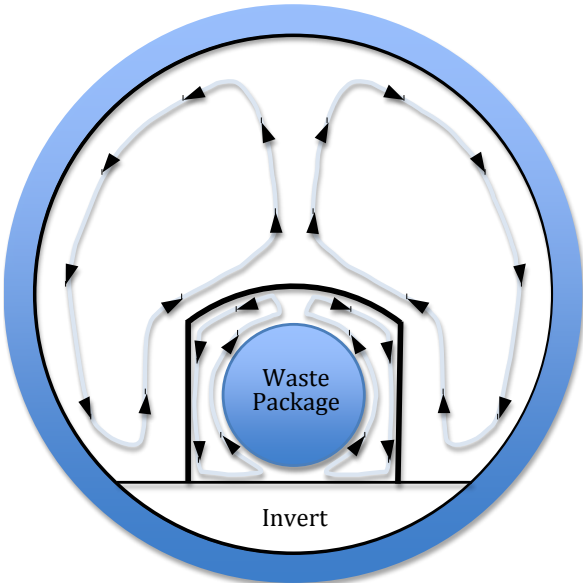

Figure 4.1: Average flow patterns for natural convection processes in radial direction from (i) waste package and drip shield, and (ii) drip shield and drift wall.

4.1.2 In the Open-Air spaces of the Emplacement Drift

The heat generated from the radioactive decay of nuclear waste will create temperature differences in the emplacement drift, in both the axial and transverse directions, giving rise to natural convective flows within the vapor/air mixture.

In the transverse direction, from the heated surfaces to the drift wall, a natural convection flow is established as the air layer close to the drip shield is heated, with its density decreasing in the process. This lighter, warmer volume of air will rise as a heated plume due to the buoyancy effect and continues to rise until it reaches the top of the drift tunnel—a region referred to as the drift crown. Thermal energy of the air volume is then transferred to the colder rock surface, decreasing the temperature of the gas while increasing its density. The gas then begins to flow downward along the drift wall to the invert floor—establishing a natural convective flow in a radial region as shown in Figure 4.1. This process causes turbulence in the air volume undergoing this motion, increasing the mixing of the air and vapor masses that exist within it.

In the axial direction, large scale natural convective circulation patterns will form, giving rise to a transport mechanism for the vapor mass produced in the hot drift center to migrate to the cool drift end—further enhanced by the turbulence provided from the radial mixing discussed previously. This heated moist air would be transported down the drift until it arrived in the cooler drift end, where thermodynamic conditions there would require that the vapor-rich air condense a portion of its water content. Thus, the drift turnouts can behave as an engineered system to condense

vapor, commonly referred to as a cold trap. This cold trap effect would occur for both periods of boiling (when vapor is produced by the boiling front on the heated rock) and non-boiling (when vapor is produced by evaporation from the heated drift wall) as shown in Figure 4.2.

If sufficiently large in its rate and magnitude, this vapor transport process and cold trap effect would be a primary mechanism for sustained reduction of relative humidity[1] in the drift center, promoting a further drying of the rock in this region and reducing the likelihood of seepage during the thermal perturbation. Similarly, with a large rate of vapor transport to the cooler drift ends, differences in decay heat output from the varying radioactive waste stream might result in condensation near cooler waste packages, a potential outcome not beneficial for repository performance and assessment. The understanding of these processes, and their impact on the redistribution of moisture in the heated repository, form the basis for our investigation.

4.1.3 At the Drift Wall and other In-Drift Boundaries

The drift wall acts as the physical boundary connecting the two different domains of the fractured rock mass and the open in-drift and, as such, defines the characteristics of the transport processes between them. Similarly, the heated surface of the drip-shield and waste package form the physical boundary between the heated source and the in-drift environment, and as such, govern how heat is transported to the air/vapor mixture bulk volume.

The fractured rock domain is governed by fractured porous media transport, and the open in-drift governed by natural convection transport—two distinct systems that vary greatly in the time scales and length scales over which transport occurs. Through the drift wall occurs the exchange of both heat and mass (air and water vapor) between the domains and, depending on local thermodynamic conditions, in directions both into and out of the fractured rock. This can be explained with first considering the heated plumes of the air mixture rising from natural convection flow and transporting heat to the drift wall as shown in Figure 4.1. In doing so, they provide the energy for the liquid moisture residing at the rock surface to undergo phase-change to a vapor—decreasing the temperature of the near-by environment in the process, a result of the latent heat of phase change.

Conversely, after the air-vapor mixture interacts with a cooler surface—presumably in the drift turnout where no waste is emplaced, or possibly, on a cooler waste canister or drip shield surface—the vapor will condense. The phase change reversal would result in both drying the air and a slight heating that occurs do to the latent heat change

[1]The relative humidity, ϕ, is a ratio between the vapor density, ρ_{vap}, and the saturated vapor density, $\rho_{\text{vap, sat}}$ at some temperature, T. It gives a value that signifies the additional existing potential for the air-mixture to contain (or not) more vapor as a constituent.

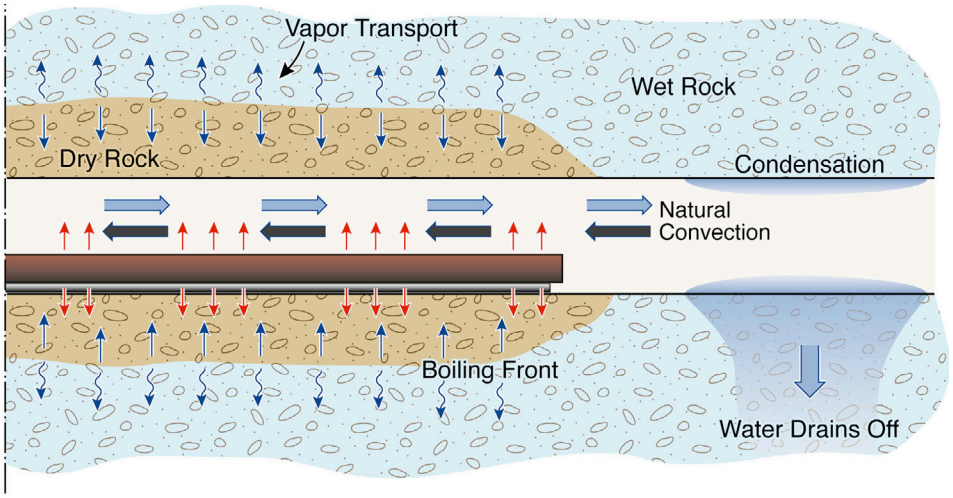

(a) *Boiling Phase*: heated drift section above boiling temperature.

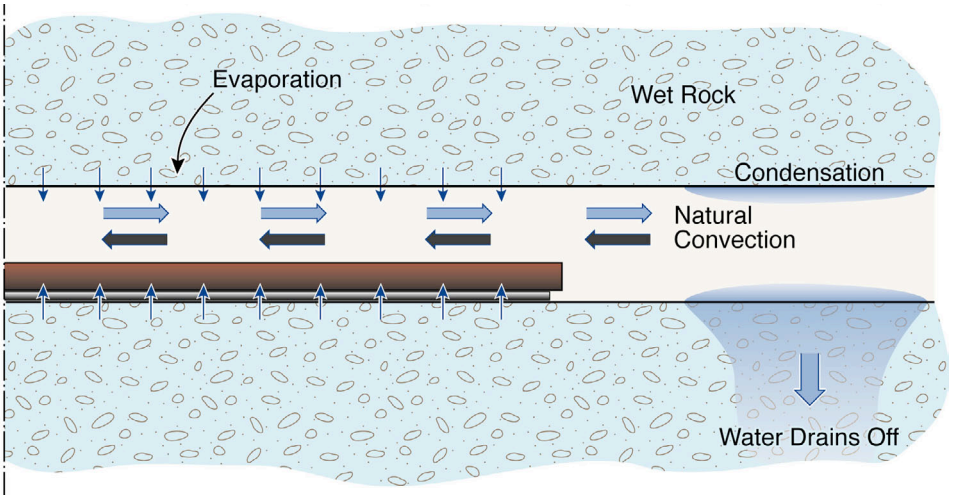

(b) *Sub-Boiling Phase*: heated drift section below boiling temperature.

Figure 4.2: Natural convection transport in the axial direction (based on Figure 2 from [17]).

to liquid, slightly increasing the temperature in the region where the condensation occurs.[2] As such, we expect that larger rates of natural convection transport (and subsequent increased rates of evaporation) will result in lower temperature of the heated drift section and higher temperatures will result in the cooler drift ends when compared to cases with reduced rates of convective transport.

[2]This effect of lower temperature in the drift center and higher temperature at the drift end would also happen without the contributions from phase changes, as natural convection also transports heat by the migration of heated vapor and air.

4.2 Conceptual Model development considering Natural Convection: the *Nat-co Model*

To include the effects of the processes discussed in the previous section, the drift natural convection model (from here on referred to as the *nat-co model*) was developed to account for the:

(i) the mass and energy transport processes in the fractured rock,

(ii) the mass and energy transport processes in the open drifts, and

(iii) the heat, fluid, and gas exchanges at the interface between the rock formation and the cavity.

In general, the model concepts used for the partially saturated mass and heat transport in the fractured formation are based on existing models[26, 46]. In-drift convection was approximated as a binary diffusion process, with effective dispersion coefficients estimated from supporting CFD analyses[36]. Mass and heat transfer between the formation and the drift were approximated by empirical boundary-layer correlations[48, 56, 57], based on a previously developed methodology[58]. The governing equations for the integrated drift and rock-mass model were solved in a fully coupled, non-iterative manner, ensuring consistency between the TH conditions in the fractured rock and those in the open drift, an approach similar to a comparative modeling study[33].

4.2.1 Thermal Hydrological Processes in Fractured Rock

Assumptions from many existing TH models for Yucca Mountain form the modeling framework for this study in simulating the near-field fracture response to the thermal load imparted by the waste canisters[26, 28, 46]. The description presented here is but a summary of these substantial research efforts—much more description is available in provided references. As shown in these studies, many relevant TH processes exist in the fractured rock mass and are explicitly accounted for in TOUGH2, including:

(i) convective and diffusive movement of gaseous and liquid phases of water and air (under pressure, viscous, capillary, and gravity forces)

(ii) transport of latent and sensible heat,

(iii) phase transition between liquid and vapor, and

(iv) vapor-pressure lowering.

Fluid transport is described with a multiphase extension of Darcys law, with heat transport occurring in the porous media by conduction, convection, and phase change. A local equilibrium model of the three phases (an equation of state of liquid, gas, and solid rock) provides the thermodynamic conditions for each element. Water vapor and air gas mixtures are assumed ideal and Henry's Law is assumed for the solubility of air in water. Vapor-pressure lowering effects, important for situations with significant porewater boiling, are also included (described previously in Chapter 2). Geomechanical and geochemical effects—shown to not have a large impact on the temperature response in these models—are neglected in this study.

Due to the large impact that the highly-fractured properties of the rock at Yucca Mountain have on the transport processes there, the rock domain is described using a dual-permeability approximation so that effects of the low-permeability matrix and the high-permeability fracture are both considered. This allows the TOUGH model to calculate transport in the matrix and fracture continua separately, while still considering local interactions between them (e.g., energy transfer, imbibition, matrix diffusion), driven by the differences in the thermodynamic conditions they might have.

4.2.2 Transport Processes within the Open Air Space of the Emplacement Drift

As explained earlier, and continued in Appendix A.2.1, the open air in-drift spaces are governed by the physics of compressible fluid flow and can be described by Navier-Stokes equations. The spatial and temporal discretization requirements for a numerical mesh adequate to bound all important processes—mass, momentum, and energy conservation—that impact flow in such a system demand very detailed resolution. The modeling of transport processes in porous media flow, however, have different requirements for numerical discretization procedures. Flow processes occur over much longer times and over much shorter distances and therefore, do not necessitate the high resolution found in CFD meshes. Knowing this, to include the calculations of both of these models, a complex coupling would have to be undertaken—spatially at the interface between the two domains and temporally with a time-stepping iterative scheme. An obviously challenging and extremely computationally-intensive endeavor, it has yet to be undertaken.

Instead, researchers have attempted to overcome this difficulty by developing approximate solutions for the coupled domain problem. One such endeavor is performed with the development of a lumped-parameter CFD model for the in-drift domain that allows use of an efficient iterative coupling scheme with porous-media simulators[39, 59]. In another endeavor, the in-drift domain was represented as an equivalent porous medium allowing a direct, non-iterative solution to the coupled problem[17]. The research presented here is a continuation of this study, and as such still follows the methodology

described in [17, 60], by assuming that the heat and mass transfer of the open in-drift can be represented with the standard methodologies applied for Darcy-type flow and transport (such as those implemented in TOUGH2), with the drift represented as a specific solution subdomain that requires certain code modifications and parameter specifications.

In short, changes were implemented to the TOUGH2 code allowing users to define natural convection subdomains in which binary diffusion is calculated using a predefined value—calculated from complementary CFD flow-field simulations—for effective dispersion coefficients, thus approximating the axial transport of vapor and energy. Drift elements representing such subdomains are assigned thermal conductivities calculated based on a Lewis number[3] equal to one so that heat and energy transport at the same rate, and, in addition, the values are applied isotropically, so that the effects are the same in both the radial and axial directions. With these changes, TOUGH2 can solve simultaneously for heat and fluid flow within the drift and in the surrounding rock mass in a direct procedure avoiding iterative solution techniques, more details can be found in [17].

4.2.2.1 Effective Dispersion Coefficient

Because of the significance dependance that the *nat-co model* has on the effective dispersion parameter, D, it is derived here for conceptual understanding of how the approximation methodology is connected to the CFD calculations (procedure adapted from [58]). In-drift axial vapor transport, a result of bulk fluid mixing from natural convection, varies the thermodynamic conditions of the in-drift air/water vapor mixture in space and in time. The convective mixing is a phenomena driven by concentration and temperature gradients in a fluid, and as such, has an ill-defined, however, real relationship with the magnitude of axial transport—larger gradients result in larger convection driving forces.

To approximate axial natural convection and the subsequent net vapor migration down the drift in a porous-media model, we try and capture the impacts of temperature and concentration gradients with a simplistic, yet effective, approximation of the vapor mass transport as a simple diffusive flux. We begin by defining the vapor mass flux as,

$$\frac{n_{\text{vap}}}{A} = \rho_{\text{mix}} D \nabla C_{\text{vap}} \qquad \left[\frac{\text{kg}_{\text{vap}}}{\text{m}^2\text{s}}\right] \tag{4.1}$$

[3]The *Lewis number* is a dimensionless parameter defined as the ratio of the thermal diffusivity to the mass diffusivity and is used to characterize flow systems in which both energy and mass transport via convection. Traditionally, it can be defined as $Le = \alpha/D$, where α is the thermal diffusivity of the fluid mixture and D the mass diffusivity. In the case of air-vapor mixtures in temperatures similar to found in the in-drift environment at Yucca Mountain, previous correlations developed for the Lewis number show that both mass and energy transfer at nearly the same rates (i.e., $Le \sim 1$)[61, 62].

where n is the net axial mass flow rate of vapor driven by natural convection $\left[\mathrm{kg_{vap}/s}\right]$, A is the cross sectional area of the flow conduit (in the case of Yucca Mountain, the area of the open air space) $[\mathrm{m^2}]$, ρ_{mix} is the air/vapor mixture density $[\mathrm{kg_{mix}/m^3}]$, D is the dispersion coefficient $[\mathrm{m^2/s}]$, and ∇C_{vap}, the concentration (mass fraction) gradient [1/m]. Solving for the dispersion coefficient, D we proceed as,

$$D = \frac{n_{\mathrm{vap}}/A}{\rho_{\mathrm{mix}} \nabla C_{\mathrm{vap}}} \qquad \left[\frac{\mathrm{m^2}}{\mathrm{s}}\right] \tag{4.2}$$

The dispersion coefficient, D, can also be described as a proportionality constant, effectively relating vapor mass flux n_{vap}/A, to some potential, in this case the vapor concentration (or mass fraction) gradient, ∇C_{vap}.

Equation (4.2) yields a value that relates rate of vapor flow to some driving gradient and absolute reference, and was used to calculate the dispersion coefficients in Table 4.1, as performed in [58]. From here, it can be implemented in porous-media calculations for Darcy-type flow, and is directly used in the *nat-co model* by substituting the dispersion coefficient, D, for the molecular diffusion coefficient, d^{κ}_{β}, in Equation (2.12). Noted is that with an increase in the rate of vapor transfer due to this approximation, expected also is an increase in the rate of energy transfer, as the rate of enthalpy that is associated with the vapor flow increases also, as shown in the convective component of Equation (2.10).

Additionally, however, natural convection would also result in an axial transport of energy due to the mixing of the entire heated gas volume (not the same process as the energy associate with the vapor transfer, as we have just described). This process is also accounted for using the dispersion approximation, however, now desired is a diffusion approximation for energy driven by temperature gradients, or, as it is better known, heat conduction. Again, we assume that thermal diffusivity, α, is equal to the mass diffusivity, D for the air-vapor mixture ($Le = 1$) and with this, we define an enhanced thermal conductivity for the in-drift elements as,

$$\lambda_{\mathrm{eff}} = \alpha_{\mathrm{eff}}\, \rho_{\mathrm{mix}}\, c_{\mathrm{p}} \tag{4.3}$$

where the effective thermal diffusivity, α_{eff}, is simply equal to the effective dispersion coefficient, D, and is modified in the heat conduction component of Equation (2.10).

4.2.2.2 Thermal Radiation

Thermal radiation is also defined between in-drift elements, with thermal radiation only connections and can be assigned between emitting (waste packages or drip shield elements) and receiving surfaces (drift wall, invert). This transport occurs unobstructed across the finely discretized open gas spaces that allow for in-drift mass and

heat transfer, and is defined with the Stefan-Boltzmann equation, previously described in eq. (2.13) on page 20. Also, three-dimensional geometry was considered by calculating view factors using a preprocessing code, allowing for detailed representation of radial and axial surface-to-surface radiation, including the effects of individual decay heat output from different waste canister types. The impact of radiation, along with a detailed development of radiation transfer, is presented previously in Chapter 3.

4.2.3 Transport at the drift wall boundary and other In-Drift Surfaces

The formations of boundary layers, a response to the viscous forces applied to the moving fluid at the surface, results in a unique transport situation at the heated surface (a detailed discussion presented in Appendix A.1). This complex interaction of the exchange of heat and liquid through such a surface has been characterized in analytical models[63], however, in the case of in-drift environment at Yucca Mountain was accounted for using natural convection correlations[58] developed by previous investigations[48]. Following this methodology, the in-drift surfaces are approximated by four surface groups (i.e. drip shield top, drip shield side, invert, or drift wall), as shown in Figure 4.3, for which each have a specific correlation from which a Nusselt number is calculated. These Nusselt numbers, specific for the system in question, allow for the calculation of a correlation heat transfer coefficient, hc_{eff}, as described in Appendix A.2.1.

For our case, modeling convection in open air, we must create an effective thermal conductivity to supplement the effect that natural convection has on heat transfer. To do this we will solve for an effective thermal conductivity using the following relation

$$k_{\text{eff}} = hc_{\text{eff}}\,\delta \qquad \left[\frac{\text{W}}{\text{m K}}\right] \tag{4.4}$$

where hc_{eff} is the heat transfer coefficient calculated from the correlation approximations in Appendix A.3 and δ is a chosen thickness, based on the grid discretization, of the air element adjacent to the heated surface. The resulting k_{eff} then used in the TOUGH2 model by replacing the existing thermal conductivity in the heat conductivity calculation given in Equation (2.10)) for connections between the heated surface elements and the in-drift air elements. Acting as an enhanced connection that accounts for the boundary layer effect on heat transfer, these air elements of chosen thickness will conduct heat away from the heated surface at the increased rate specified by the effective conductivity.

Additionally, these air elements are used to enhance the connections between the drift wall surface elements and the in-drift elements by modifying the mass transport rate shared between them. This approximation, again assuming the Lewis number is equal

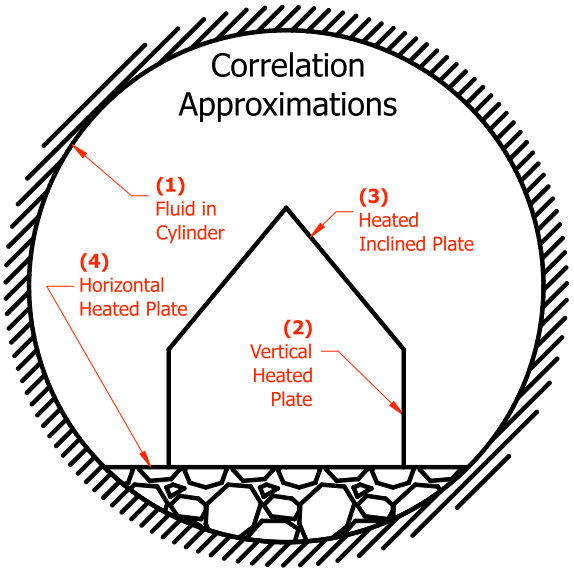

Figure 4.3: Geometry simplifications for in-drift surfaces for calculation of Nusselt correlations.

to one, helps to include the effects of the boundary layer on mass transport at this surface, along with heat transport.

4.2.4 Model Geometry

Following the design developed by Spycher et al.[64], a simplified, three-dimensional, geometrical grid was constructed, representing an emplacement drift located in one of the southern panels of the proposed repository layout as shown in Figure 4.4[17, 65]. The model domain is composed of the entire unsaturated zone, having the mountain ground surface as the upper model boundary and the groundwater table as the lower model boundary, with specified pressures, temperatures, saturations and, in the case of the upper boundary, infiltration rate. In the axial drift direction (y-direction), symmetry is assumed, which allows for reducing the model to half of the drift length—assuming then that the boundary conditions on both ends of the drift tunnel would be relatively similar. Thus, the simulated drift comprises half of the typical emplacement section length (300 m), followed by an 80-m unheated section away from the symmetry axis. With this, the total length of the model domain in y-direction is 520 m, and includes both the 380-m-long drift plus a 130-m extent of fractured rock beyond the end of the drift. The current repository design of parallel drifts allows for even further reductions to be taken to the model domain in the x-direction, by representing it as a series of symmetrical identical half-drift domains with vertical no-flow boundaries

between them. Thus, the numerical mesh can be limited to a lateral width of 40.5 m, extending from the drift center to the midpoint between drifts centers.

As with any simulation, it is important to have refined mesh discretization in the region under investigation, such as the in-drift and near drift environments in the case of this study. Still important, however, is to utilize simplifications, reducing complexity in the calculation and with it, valuable computational time. As such, the waste package, drip shield, and small air space between them are treated in our study as a single, lumped entity—neglecting the flow and transport processes occurring between them—and thus share equivalent thermal properties based on averaging the respective thermal properties of each component. Further simplifications were applied to the model geometry by neglecting the curvature of the drift turnout along with assuming horizontal boundaries at the top mountain surface model boundary and the water table boundary below. Considering the long distances and the large volumes between these regions and the near-drift environment (where we are interested in the transport processes), such simplifications should have little impact on the research effort[17, 65].

The numerical grid is composed of numerous layers, extending from the mountain surface to the water table, of varying thickness along the drift axis (y-axis), and ranging in length from less than 5 m to around 50 m. Similar to a previous Yucca Mountain modeling effort[33], there are two finely gridded segments along the emplacement section—where the thickness of the vertical slices corresponds to the axial length of individual waste packages—as displayed in Figure 4.5. One is located near the drift center, the other at the end of the emplacement section, and it is only in these segments where we will consider the large variability of the decay heat output between waste packages, described ahead in the next section. For grid efficiency purposes however, all other emplacement regions have the average decay heat imposed as a uniform axial line load. In final, the *nat-co* mesh is composed of nearly 14,000 finite volumes and shares about 50,000 connections between them.

4.2.5 Model Boundary Conditions

Decay Heat Load

The current design estimates for waste package loading scenario at Yucca Mountain estimate an initial heat load output by the radioactive waste of 1.45 kW per meter drift length[54]—a value representing the average heat load for all the radioactive waste canister types to be emplaced in the repository. According to the idealized design configuration from where this average is calculated[54], the varying waste packages are arranged in sequence, arranging cooler waste packages such as the *5 HLW* to be situated next to hotter waste packages such as the *21 PWR AP* or the *44 BWR AP*,

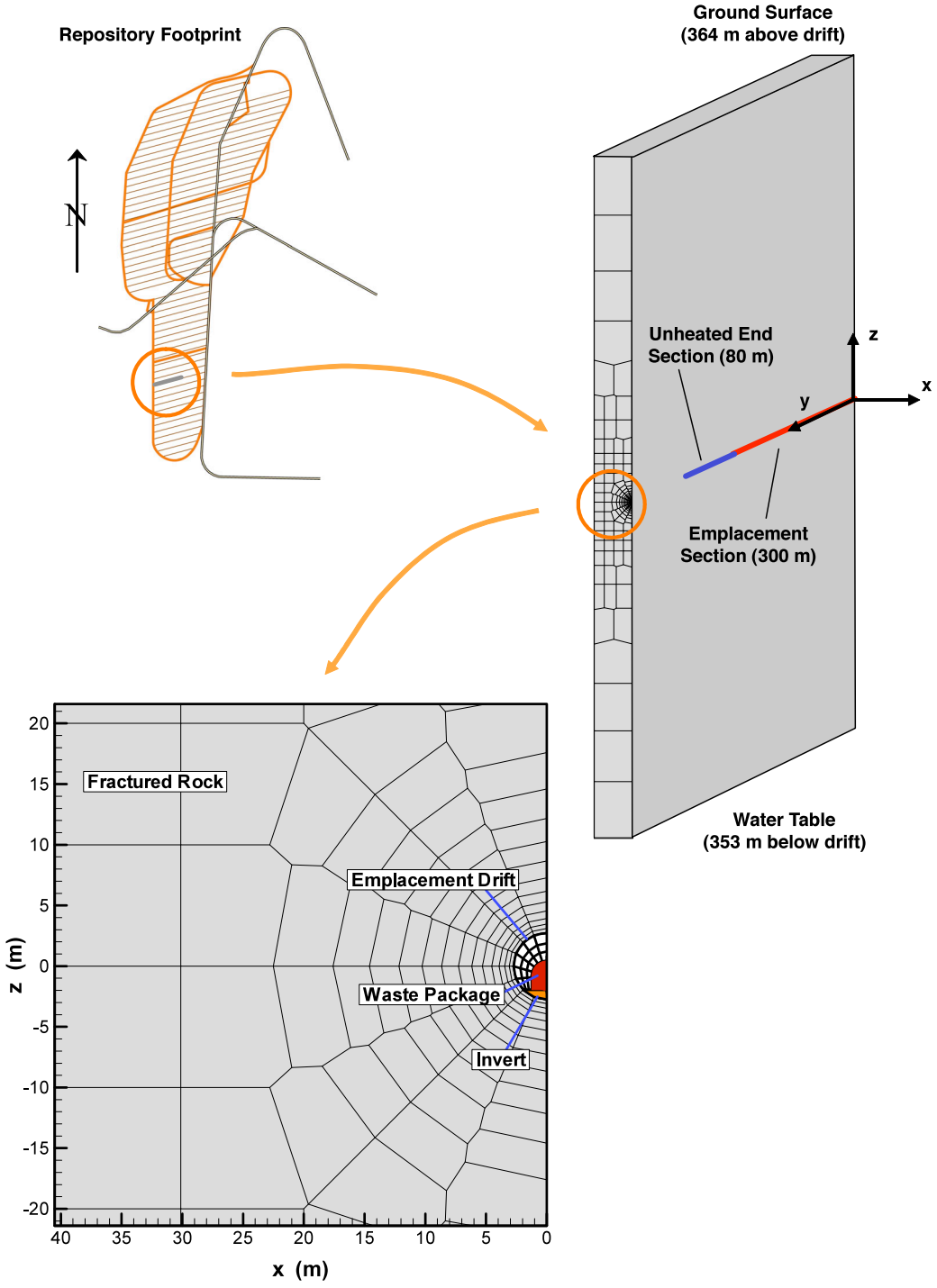

Figure 4.4: Schematic showing the geometry of the three-dimensional model domain (not to scale). The upper left shows the repository footprint and the location selected for consideration (including geological parameters unique to this region). Close-up view shows discretization of drift and drift vicinity (based on Figure 3 from [17]).

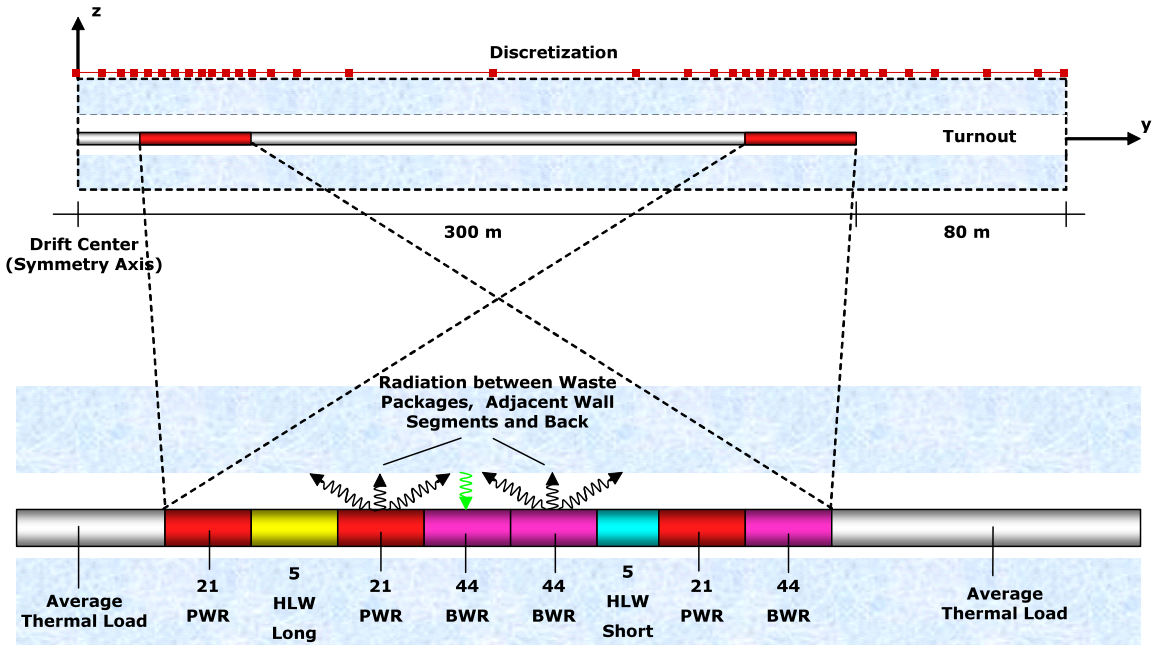

Figure 4.5: Schematic model geometry along emplacement drift. Red dots indicate location of vertical slices. Two segments along the drift at both the drift center and the drift end, labeled **2**1 PWR, are finely discretized to accompany individual waste packages. Notice the yellow and cyan HLW waste packages, which have the smallest heat output.

as shown in Figure 4.5. The thermal load of all waste packages is time-dependent—decaying in an exponential manner from an initial value—and ranges between 0.2 kW per meter-drift for the *5 HLW LONG* and 2.3 kW per meter-drift length for the *21 PWR AP* (shown in Figure 4.6). Varying by over an order of magnitude, the decay heat output of the differing waste canisters, and subsequent thermodynamic conditions formed by them, could result in regions of higher rock saturations (and localized condensation near cooler waste packages, as discussed in [65]). As such, this modeling effort considers two decay heat load scenarios:

(i) a scenario with an **average decay heat load** prescribed to all waste canister elements, and also,

(ii) a scenario with the **individual decay heat loads** prescribed to two specific drift regions as is depicted in Figure 4.5 (capturing the effects of the significant difference in the decay heat outputs).

Note that a considerable amount of the decay heat is removed by forced drift ventilation during the first 50 years after emplacement, ensuring a reduced temperature of the drift environment that allows physical access to the waste canisters. Similar to

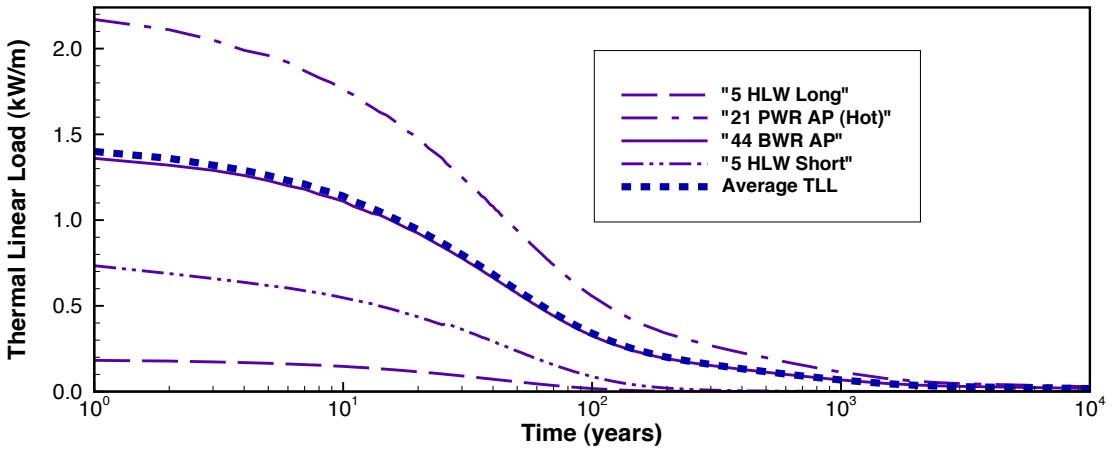

Figure 4.6: Thermal linear load (TLL), or decay heat output from individual waste canisters types, per unit length canister [kW/m], as a function of time. Time zero represents the time of waste emplacement. (from Bechtel SAIC Company, 2003[54]).

previous studies[26, 47], forced drift ventilation is not explicitly modeled in the *nat-co* simulations. Instead, the heat losses by forced drift ventilation are incorporated by reducing the effective decay heat output in the simulation to 14% of its original value, based on Yucca Mountain Project design estimates[66].

Mountain Surface, Water Table, and Grid Vertical Boundaries

Both the mountain surface and water table boundaries of the model domain are far enough away from the repository units[4] such that they are not significantly affected by the decay heat thermal input and, accordingly, were assigned constant Dirichlet-type conditions for temperature, with boundary values based on the geothermal gradient. Gas pressure at the top mountain surface boundary is constant and derived from average barometric conditions at Yucca Mountain while surface infiltration was included by imposing uniform percolation flux values that vary with time. Consistent with future climate and infiltration analyses for Yucca Mountain[67], the model considered three long-term climate periods with constant percolation, with the imposed average percolation fluxes during this times given as:

(i) **6 mm/yr:** the present-day climate (up to 600 years from emplacement of waste)

(ii) **16 mm/yr:** the monsoon climate (600 – 2000 years)

[4]The *repository units* are those geologic units at Yucca Mountain in which the emplacement drifts will reside.

(iii) **25 mm/yr:** glacial transition climate (>2000 years).

all representing average infiltration conditions. At the bottom of the model domain, the groundwater table was modeled as a flat, stable surface saturated with water and impermeable to gas flow. All vertical boundaries, the sides of the numerical grid, were subject to no-flow conditions for gas, liquid, and heat.

A Dirichlet-type boundary condition was also defined just outside the turnout section, where the emplacement drift is connected to the main access drift via a bulk-head door. Assuming good communication to the atmosphere (i.e., assuming that access drifts are backfilled with a high-permeability crushed tuff material), the main access drift was represented using a fixed gas pressure value based on the ambient gas pressure at depth. Also fixed were temperature (using the initial geothermal temperature at depth) and vapor concentration (equilibrium vapor pressure at a given temperature). These boundary conditions were constant with time; the effect of short-term barometric pumping was ignored. The bulkhead door separating the main access drift from the emplacement drift was modeled as a low-permeability, low-conductivity zone between the respective domains.

4.2.6 Thermodynamic and Geological Properties of the In-Drift environment and Rock Mass

The representative emplacement drift selected for this modeling study is located in the Topopah Spring Tuff lower lithophysal unit, the major host rock unit at Yucca Mountain. The hydrological and thermal properties used by the *nat-co model* to represent this geologic unit were derived from properties sets complied by a previous calibrated property model[68]. Unlike previous studies, the stratigraphic variation of geologic layers and small-scale variability of TH properties—an effect of rock heterogeneity—were neglected for this study with instead rock formation properties being uniform throughout the model domain. This was done to reduce computational effort, being that these effects are not relevant for understanding the near-drift TH processes investigated in this study. Also neglected were the potential for transient changes in hydrologic properties as a possible result of heat-induced stress changes[69] or mineral alteration[64].

In-drift elements (those representing the open air-space outside the drip shield and represented by the white area in between the waste package element and fractured rock in Figure 4.4) were simulated as a high-permeability porous medium with a porosity equal to one (meaning no rock phase exists) and zero capillary strength (meaning no capacity to hold liquid water). Confirmed with sensitivity cases, the value of permeability prescribed to such elements was $\sim 10^{-8}\,\mathrm{m}^2$, along with also being assigned an effective mass and heat dispersion coefficient to account for effects of natural convection, as described previously (Table 4.1). The entire volume of the drip

shield, waste package and air gap was represented as a solid (nonporous) medium with an effective heat capacity of 394 J/kg K and a density of 1464 kg/m^3 (an average of all components). Heat transfer from this mixed-component element occurs via natural convection transport and thermal radiation transport (as described in Chapter 3). The thermal radiation properties assigned were: 0.63 for the emissivity of the drip shield, 0.9 for the emissivity of the drift wall and the invert, and 5.6687×10^{-8} W/m^{2}K^4 for the Stefan-Boltzmann constant[58]. The final in-drift region, the invert, is made of crushed tuff material and was represented as a porous medium with large permeability and rather weak capillarity.

4.3 Model Application and Results: the Impact of Natural Convection

The modeling simulations cover the first 4000 years after emplacement of radioactive waste into a representative drift, and with time, consider the diminishing decay heat load of the waste packages (Figure 4.6), along with changes in climate induced infiltration, which starts at 6 $^{mm}/_{yr}$, increases to 16 $^{mm}/_{yr}$ at year 600 and ends with 25 $^{mm}/_{yr}$ at year 2000, as described previously. This time-dependent scenario is compared with two cases of effective dispersion coefficients (given in Table 4.1)—bounding the range of the natural convection driven transport to be expected at Yucca Mountain—along with a comparison case that doesn't consider enhanced dispersion. Our interests resides in times of post closure, after the ventilation of the emplacement tunnels has ceased, with a specific interest on the transitional time from boiling to sub-boiling regimes. Previous research has shown this occurs anywhere from 600–1000 years after emplacement, well within the simulation timeframe. Finally, to understand how differences in the decay heat output from individual waste canisters might impact the local environment, also considered are average and individual waste canister loading scenarios.

4.3.1 TH conditions: near-field rock saturation cross sections

To understand the impact that the decay heat has on the thermal-hydrological conditions of the near-field domain, we begin first with an observation of the near field fractured rock some time after emplacement. The ambient environment, before the waste has been emplaced, has geologic conditions that reflect the temperatures, saturations, and pressures of this region at depth. Saturations in the fracture domain are very small, a result of the small rate of percolation (a few mm/yr) and also a result of a matrix capillarity that is orders of magnitude larger than that of the fracture—strongly imbibing any liquid water from the fracture network. While the fractures are relatively dry and nearly nonconductive, the matrix has a large saturation (around

0.85); however, this porewater is mostly stagnant to the extremely low permeability of the fine-grained domian. Temperature of this region is around 25°C with a local gas pressure around 89 kPa, close to ambient pressure at the repository depth. The mass fraction of vapor in the gas phase is small, representing a relative humidity of 100% at a saturation temperature $T_{\text{sat}} = 25°\text{C}$ (a warm, and humid environment).

We begin by plotting the saturations, of both the matrix and fracture domains, for two-dimensional cross-sections along the length of the drift, and observe specifically the two regions where the decay heat output of individual waste canisters are defined, one at the drift center and the other at the drift end. Figures 4.7 to 4.12 contain such cross sections, and extend vertically from 25 m above and 35 m below the emplacement drift center and horizontally from the drift center ($5\,\text{m} < x < 145\,\text{m}$) to the drift end ($235\,\text{m} < x < 380\,\text{m}$). The six figures represent six scenarios, three times of 100, 500, and 1000 years after emplacement and consider both convective mixing cases: case 1 with *strong convective mixing* and case 2, with *moderate convective mixing* (case 3, with *no convective mixing* is considered later).

We consider, first, the scenario at 500 years after emplacement for case 1, with strong convective mixing shown in Figure 4.8 on page 60—the second figure in the set of saturation cross sections. The top row shows the colored contours of the fracture saturation overlaid with contour profiles of temperatures of the surrounding rock at both the drift center and drift end, while the bottom row shows the colored contours of the matrix saturation overlaid with contour profiles of the vapor mass fraction. At 500 years after emplacement, we can observe a significant amount of drying (represented by the lighter-colored regions) of both the fracture and matrix domains surrounding the drift in regions at the drift center and end—testament to the significant amount of decay heat load still present at this time. This dry region extends meters into formation and indicates that a significant amount of porewater boil-off has occurred and is still occurring (temperatures of $T_{\text{rock}} > 96°\text{C}$ still exist), corresponding to the elevated vapor concentrations observed in the rock surrounding the heated drift, as high as 0.5 at a distance 10 m away from the drift center. The rise in vapor concentration is not restricted to only the boiling region, as vapor concentrations near 0.4 occur 30 m above and below the drift, with the concentrations reaching such values due to vapor transport through the permeable fractured network. With time vapor concentrations around the drift decrease, a result of the dropping temperature, however, still remain well-above ambient at 0.4 at 1000 years after emplacement.

We can also take notice in Figure 4.8 of the differences in saturation of the formation between the hotter drift center (with temperatures around 90°C around most of the tunnel) and the cooler drift end (with temperatures around 70°C). Specifically, we take note of the region of high saturation that has formed at the end of the emplacement tunnel—in the unheated section near the drift bulkhead. Knowing the *nat-co model* characteristics, this region of high saturation is the outcome of a condensation process that is occurring there, and is a direct result of the vapor production and subsequent in-drift transport along the concentration gradient from the moist drift center to

the cool drift end—a first result capturing the expected effects of natural convection transport. The region of increased saturation exists in both fracture and matrix domains, but is, larger in scale in the fractures, extending significantly below the drift, thus implying that the condensate is primarily transported away from the drift through the fracture network (figure 4.7a). The rise in matrix saturations is due to the imbibing of this condensate drainage, with increased saturations observed not only below the drift, but above it as well—condensation occurs on all drift-wall surfaces (figure 4.7b).

To understand the driving forces for the flow processes, we look to the vapor concentrations contours to understand the gradients that are formed, in both the axial and radial directions. As mentioned, the subsequent saturation increase found at the emplacement tunnel end was due to axial vapor transport, and while difficult to immediately discern from Figure 4.7a, the vapor concentration of the in-drift in the tunnel center is much larger (~ 0.3) than at the tunnel end (~ 0.1). This results in a significant gradient that, when combined with the enhanced dispersion approximation for natural convection, drives much vapor from the heated center to the cooler end. This vapor transport process is fed by vapor production in the drift center, and, as such, pressure differences from the boiling of porewater drive vapor to the open air spaces near the tunnel center. While vapor is transported by pressure gradients, significant concentration gradients also exist—from above the drift (where $m_{\text{vap}} \sim 0.5$) to the in-drift (where $m_{\text{vap}} \sim 0.3$)—resulting in vapor transport occurring also via diffusion. How these thermal-hydrological conditions compare for different convective mixing cases is discussed in the next section, after the saturation contour figure set (Figures 4.7 to 4.12).

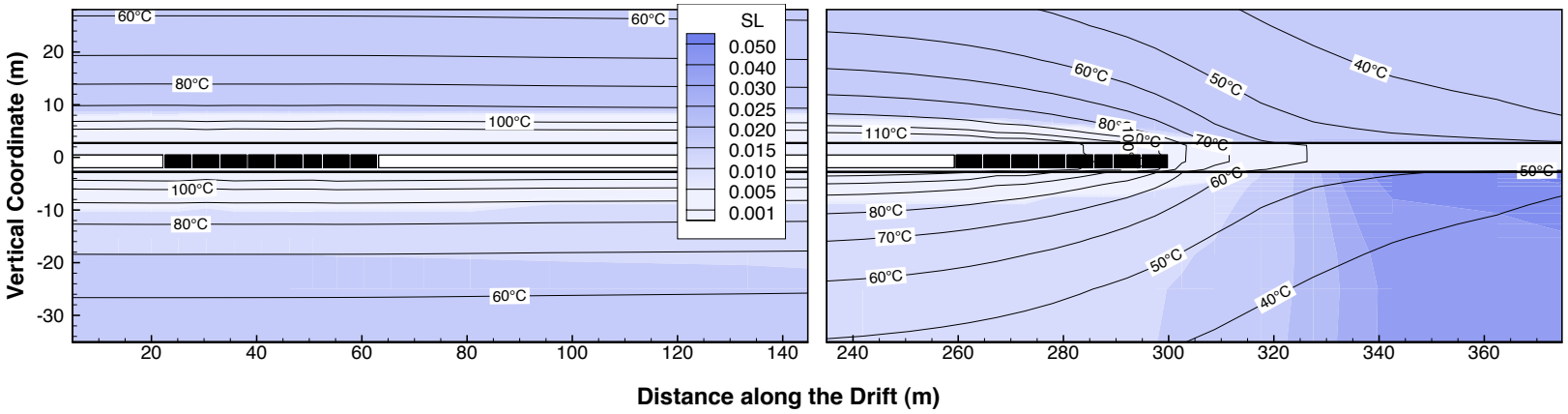

(a) Fracture saturation (shaded contour) and temperature in °C (contour lines) of the rock mass and drift.

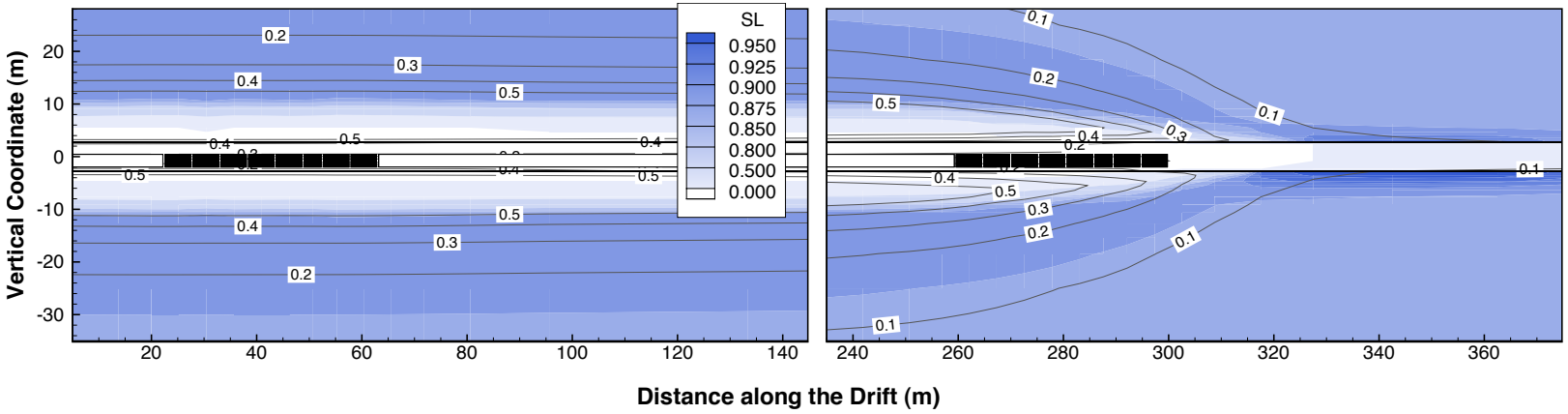

(b) Matrix saturation (shaded contour) and vapor mass fraction (contour lines) of the rock mass and drift.

Figure 4.7: 100 YEARS: (CASE 1): Simulated thermal-hydrological conditions for *strong convective mixing* in vertical cross section along the drift. Waste canisters with individual heat output (shown in black) and those with uniform heat output (shown in white) are represented in both the drift center (plots on left) and the drift end (plot on right).

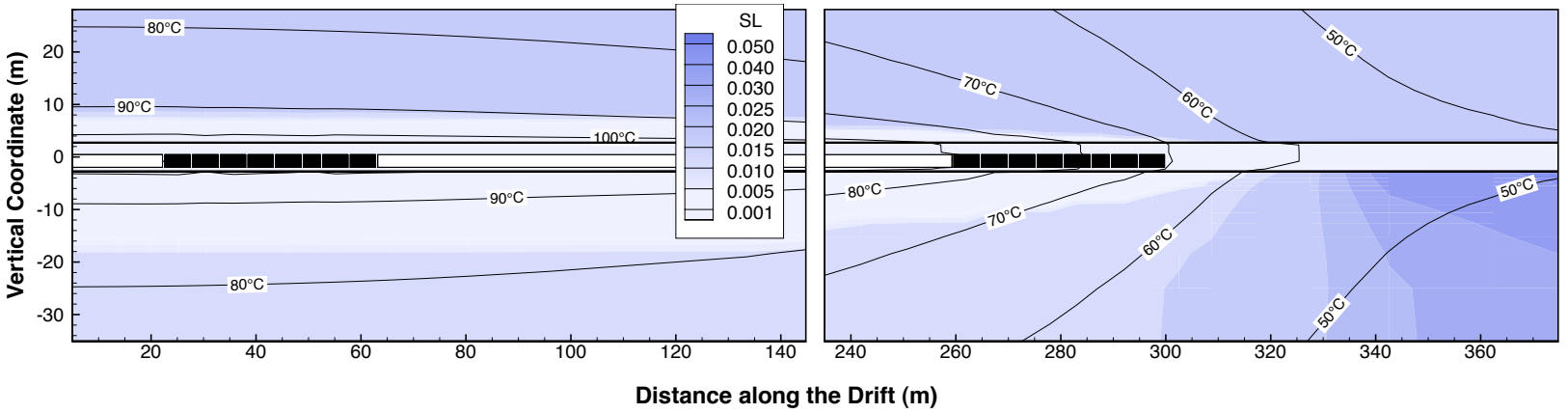

(a) Fracture saturation (shaded contour) and temperature in °C (contour lines) of the rock mass and drift.

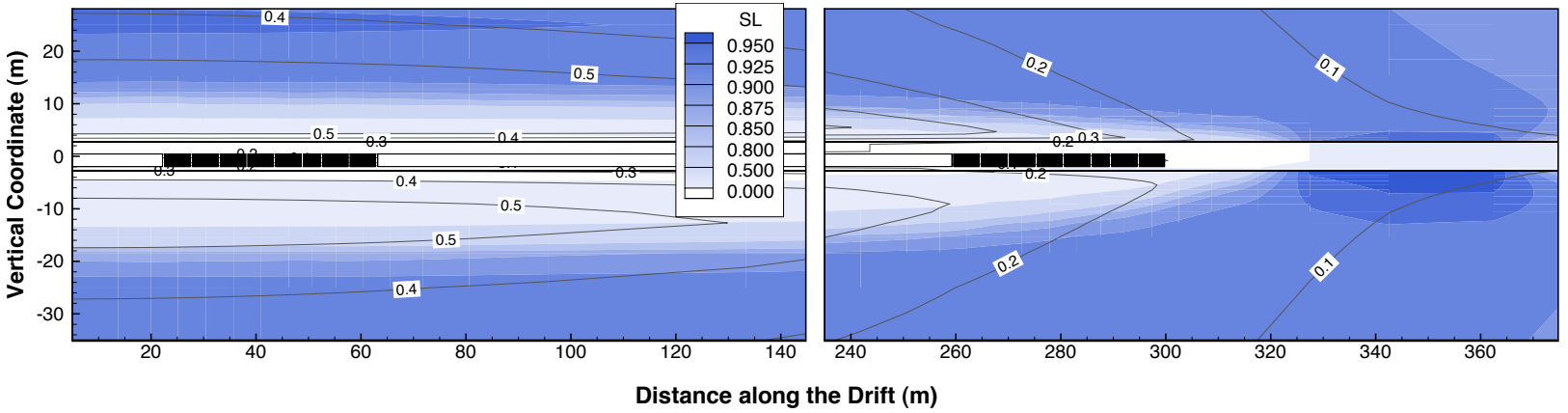

(b) Matrix saturation (shaded contour) and vapor mass fraction (contour lines) of the rock mass and drift.

Figure 4.8: 500 YEARS: (CASE 1): Simulated thermal-hydrological conditions for *strong convective mixing* in vertical cross section along the drift. Waste canisters with individual heat output (shown in black) and those with uniform heat output (shown in white) are represented in both the drift center (plots on left) and the drift end (plots on right).

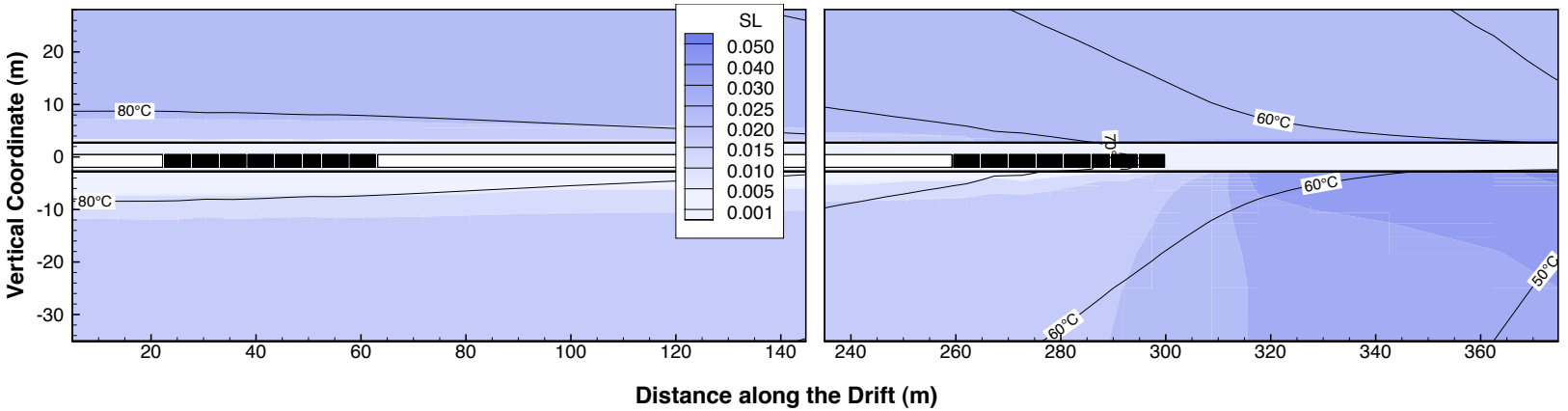

(a) Fracture saturation (shaded contour) and temperature in °C (contour lines) of the rock mass and drift.

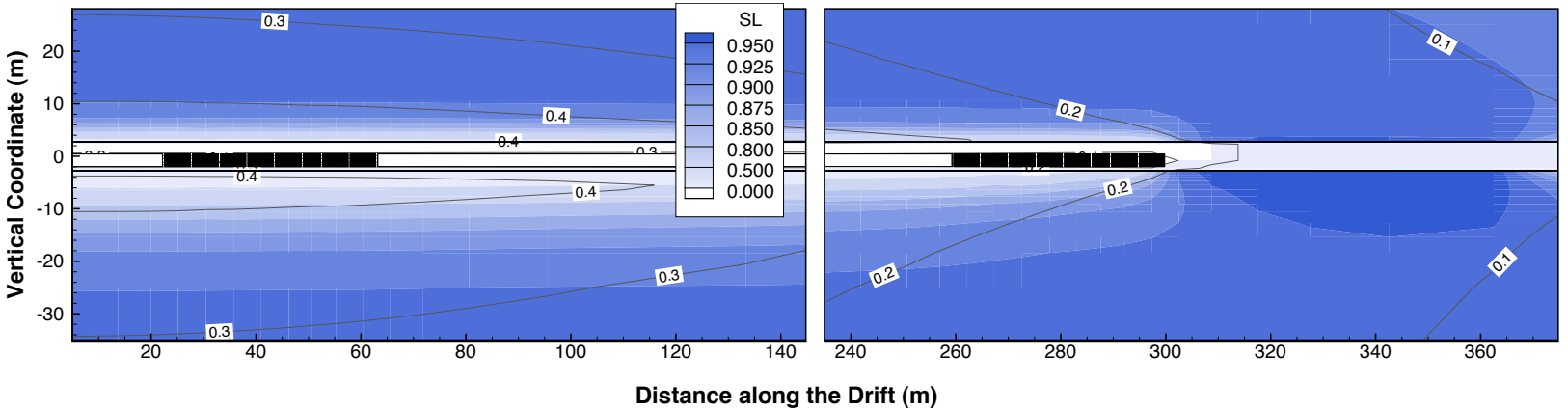

(b) Matrix saturation (shaded contour) and vapor mass fraction (contour lines) of the rock mass and drift.

Figure 4.9: 1000 YEARS: (CASE 1): Simulated thermal-hydrological conditions for *strong convective mixing* in vertical cross section along the drift. Waste canisters with individual heat output (shown in black) and those with uniform heat output (shown in white) are represented in both the drift center (plots on left) and the drift end (plots on right).

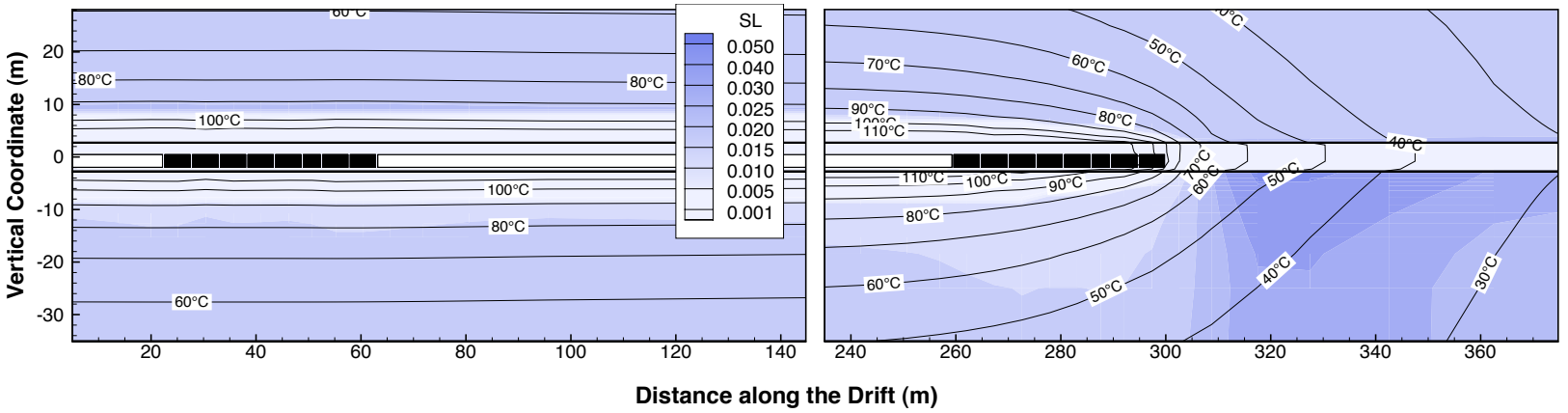

(a) Fracture saturation (shaded contour) and temperature in °C (contour lines) of the rock mass and drift.

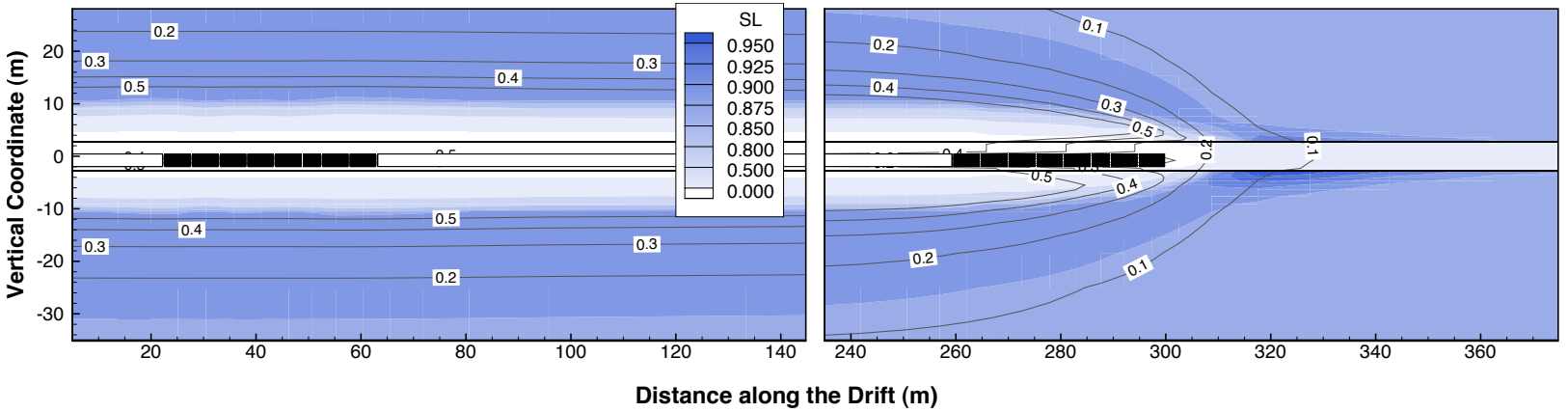

(b) Matrix saturation (shaded contour) and vapor mass fraction (contour lines) of the rock mass and drift.

Figure 4.10: 100 YEARS: (CASE 2): Simulated thermal-hydrological conditions for *moderate convective mixing* in vertical cross section along the drift. Waste canisters with individual heat output (shown in black) and those with uniform heat output (shown in white) are represented in both the drift center (plots on left) and the drift end (plot on right).

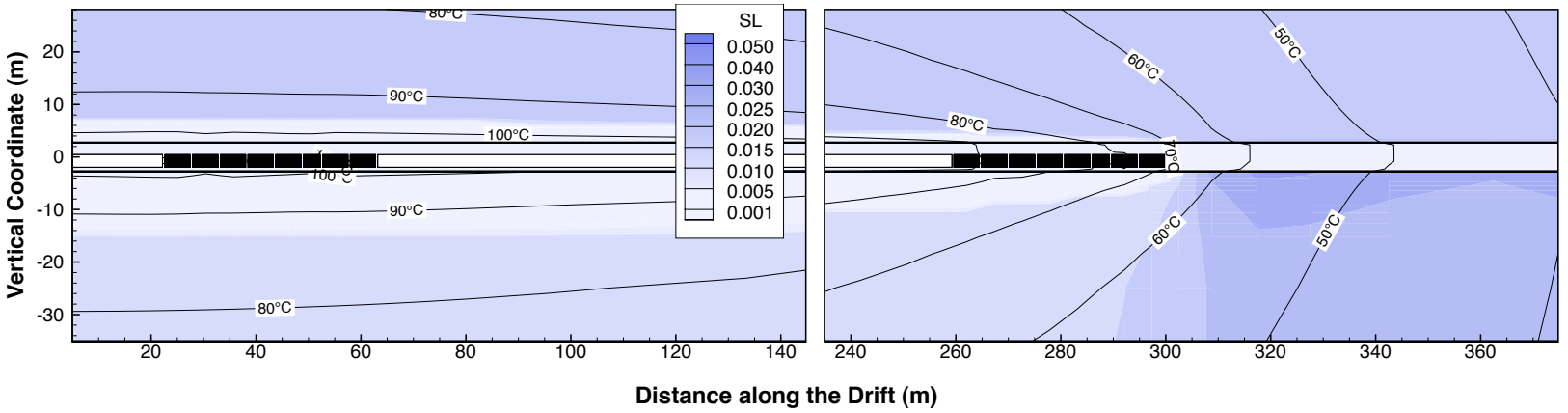

(a) Fracture saturation (shaded contour) and temperature in °C (contour lines) of the rock mass and drift.

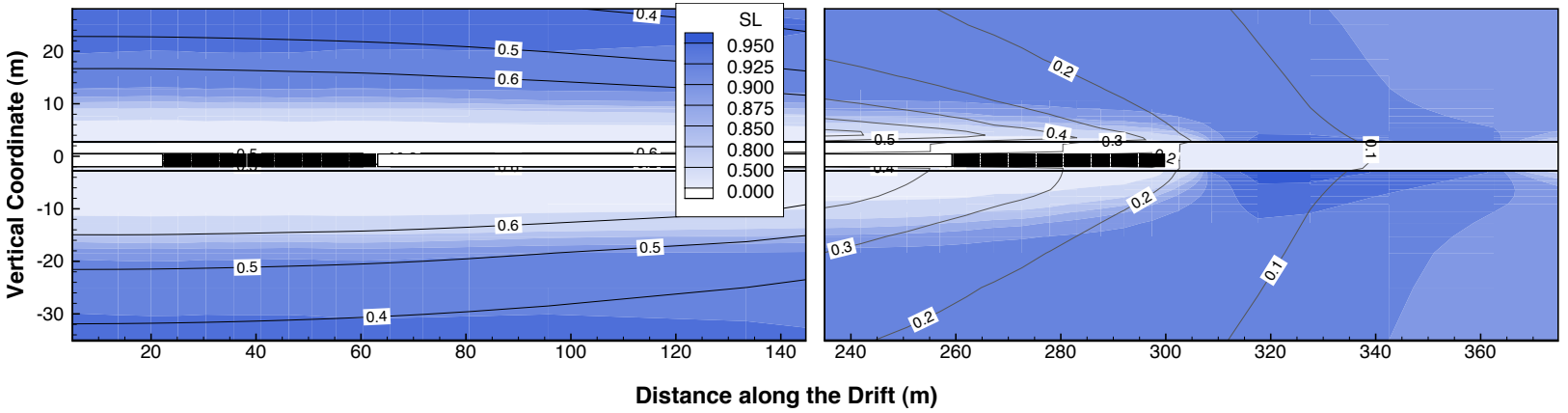

(b) Matrix saturation (shaded contour) and vapor mass fraction (contour lines) of the rock mass and drift.

Figure 4.11: 500 YEARS: (CASE 2): Simulated thermal-hydrological conditions for *moderate convective mixing* in vertical cross section along the drift. Waste canisters with individual heat output (shown in black) and those with uniform heat output (shown in white) are represented in both the drift center (plots on left) and the drift end (plots on right).

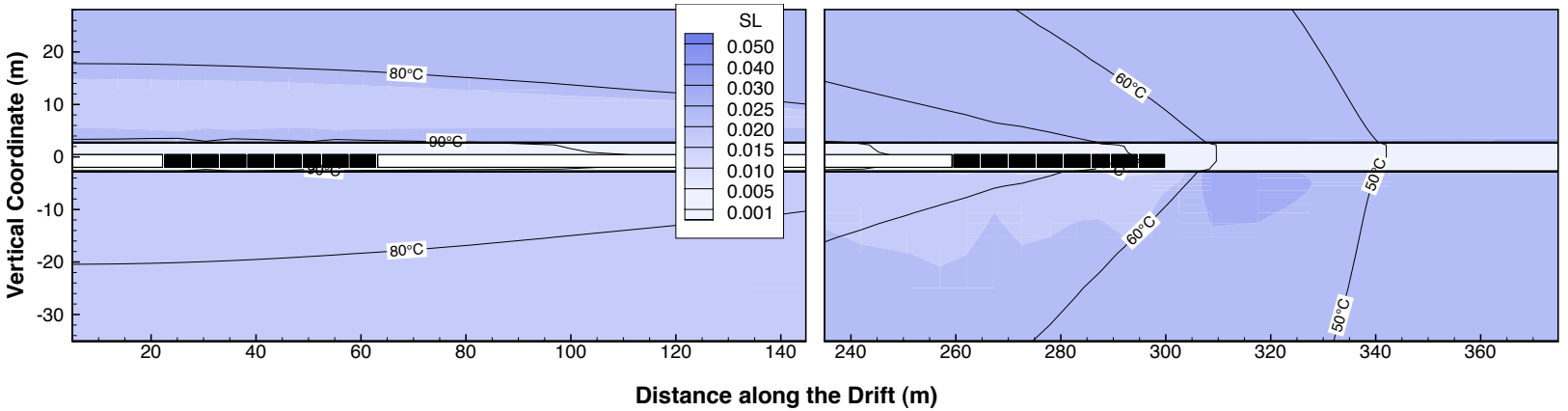

(a) Fracture saturation (shaded contour) and temperature in °C (contour lines) of the rock mass and drift.

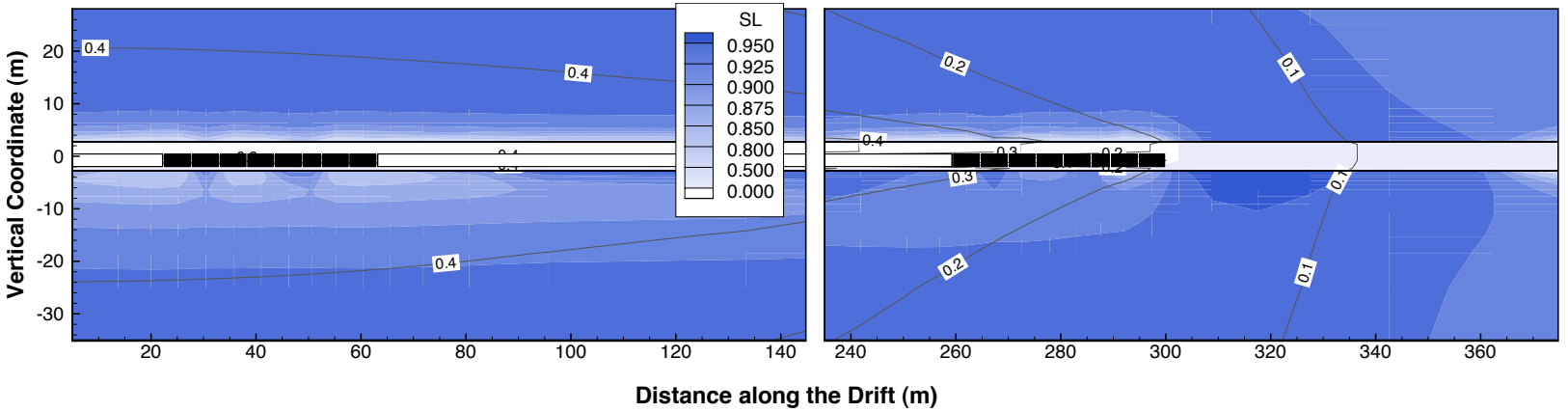

(b) Matrix saturation (shaded contour) and vapor mass fraction (contour lines) of the rock mass and drift.

Figure 4.12: 1000 YEARS: (CASE 2): Simulated thermal-hydrological conditions for *moderate convective mixing* in vertical cross section along the drift. Waste canisters with individual heat output (shown in black) and those with uniform heat output (shown in white) are represented in both the drift center (plots on left) and the drift end (plots on right).

4.3.2 Impact of Convective Mixing: comparison with No Convective Mixing case

What impact do the the three convective mixing cases (given in Table 4.1) have on the TH conditions and transport processes we previously discussed? We again consider the previous scenario of 500 years after emplacement, except for the moment will consider the case where the decay heat load for the in-drift waste package elements for the entire emplacement section is the averaged over all waste package types (dashed line in Figure 4.6). While still having the same overall decay heat output (1.45 kW/m), there now exists no variation in the individual decay heat output along the length of the drift tunnel where waste is stored. This simplification helps to better isolate the impacts the different convective mixings cases have by removing the effects of variation in decay heat load.

We plot in Figure 4.13 the drift response along the length of the drift, specifically observing the temperature, vapor mass fraction, and relative humidity, parameters that allow for comparison of the conditions for each case. The plots extend from near drift center ($x \sim 50$ m) to the drift end ($x \sim 380$ m), and include 80 m of the unheated drift turnout, where no waste is emplaced. The plots refer to all three convective mixing cases, and observe the response of the rock directly above the drift crown (represented by thick lines) and the in-drift element representing the open-air space just below the drift crown (represented by thin lines).

4.3.2.1 Temperature

The temperature profile shown in Figure 4.13a shows a significant region of the drift wall near the drift center is well-above the boiling temperature, meaning the contribution to overall vapor production by boiling is still important at this time. Along most of the heated section of the drift there are negligible differences in temperatures for all three convective mixing cases, however, towards the end of the emplacement section some variations can be observed—lower in the heated section and higher in the turnout. This variation of temperature between the cases begins where the temperatures drop below boiling at the drift wall, suggesting that increased rates of natural convection transport have little impact on temperature reduction of drift wall regions above boiling, yet begin to cause a reduction in temperatures when the drift wall enters the sub-boiling phase.

This is explained as when the temperature of the rock drops below boiling, the matrix formation resaturates, allowing evaporation to occur, with the evaporative rate being the greatest in case 1 due to its reduction of the RH of the in-drift environment (shown in Figure 4.13c). For all evaporation processes, the latent heat absorbed during the phase change reduces temperatures, therefore resulting in a slightly lower temperature for case 1, an effect that becomes greater with time. Also, the slightly

increased temperatures of the rock in the drift turnout for cases 1 and 2 suggest a more effective transport of heat due to increased rate of energy and vapor transport in that case.

4.3.2.2 Vapor Mass Fraction

The difference of the rates of vapor transport between cases is further detailed by observing the distribution of vapor concentration in the in-drift by plotting the vapor mass fraction for all cases, as shown in Figure 4.13b. Case 1 at the drift center has a vapor mass fraction of $x_{vap} \sim 0.3$ and drops gradually to $x_{vap} \sim 0.2$ at the drift turnout while Case 2, with *moderate convective mixing*, has a value ∼0.75 towards with a steady decline to a value equal to that of case 1 at the drift end. While case 1 sees a reduced vapor concentration maintained for the entire length of the drift, this effect is not apparent in case 2, which has a high vapor mass fraction near the drift center, and shows the inability for this convective mixing case to reduce the vapor concentrations throughout the length of the drift. Case 3, the comparison case with *no convective mixing*, considers binary diffusion of air and vapor only, and as such shows a large vapor concentration at the drift center (near 0.9) that is fairly constant until 50 m from the heated drift end where it drops rapidly to values similar to those for cases 1 and 2. Clearly non-physical, and a result of the inability of vapor to transport via convective processes, it shows the importance for accounting of the role of natural convection when investigating in-drift conditions.

4.3.2.3 Relative Humidity

But how are the TH conditions in the fractured rock formation impacted by the in-drift thermodynamic conditions? The evaluation of relative humidity (RH) in the drift gives an understanding for the potential to equilibrate the moisture concentration between the rock and the drift air. A relative humidity of $< 100\%$ in the drift means there exists the potential for evaporation to occur from the near-field rock, and conversely a RH near 100% means the thermodynamic conditions exist for condensation.

In Figure 4.13c we plot the relative humidity profile along the length of the drift for the three convective mixing cases, and see that both cases 1 and 2 maintain RH well below 100% for the entire length of the heated drift for this time. This means that thermodynamic conditions do not permit condensation to occur for either cases for this scenario (the impact of individual canister decay heat load is considered later). The values are relatively constant for the length of the heated emplacement section for cases 1 and 2 (approximately 30% and 60%, respectively); however, they increase quickly towards the end of the emplacement section, especially in case 1—a result of the rapid decline in temperature. It is in the unheated end section that we observe RH reaching 100% for both cases meaning condensation occurs—explaining the large

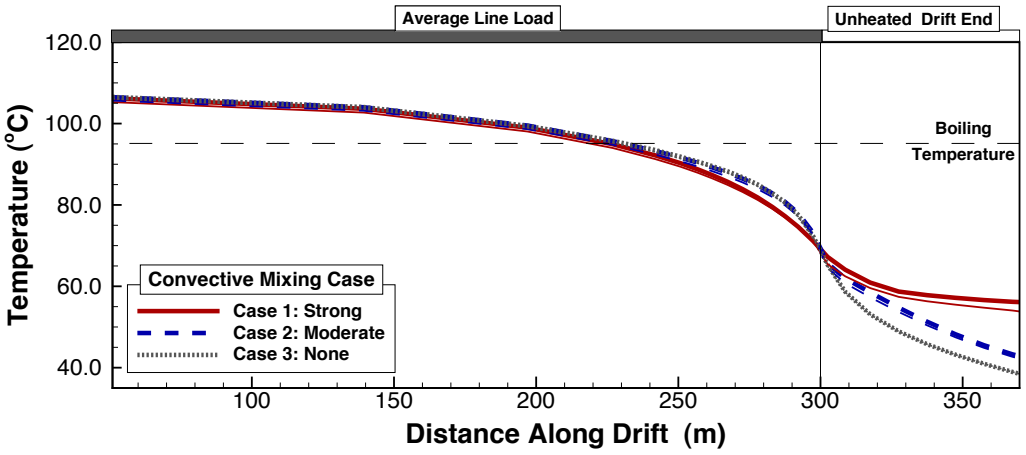

(a) Temperature profile.

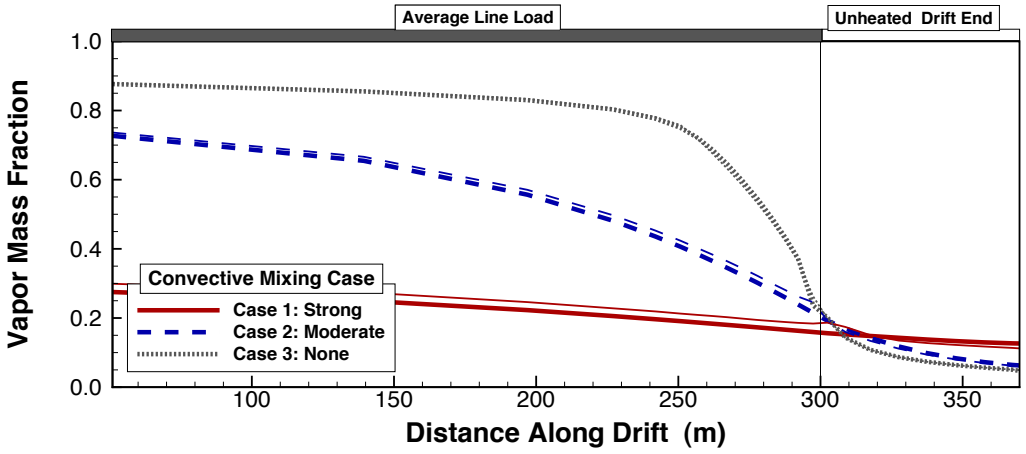

(b) Vapor Mass fraction profile.

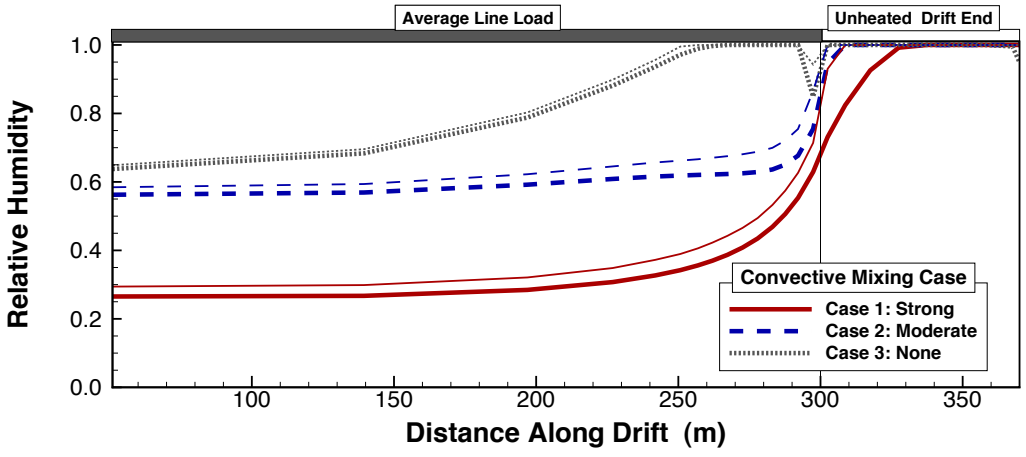

(c) Relative Humidity profile.

Figure 4.13: Profile of fractured rock along drift crown for the three convective mixing cases at 500 YEARS after emplacement. Profile extends from near drift center ($x = 50\,\text{m}$) to unheated drift end ($x = 380\,\text{m}$). Thick lines represent temperature in fracture domain just above drift crown while thin lines represent in-drift element directly below drift crown.

saturation increases observed in the drift turnout (Figure 4.8), as previously discussed. In comparison with case 3, where RH humidities are much higher, even reaching 100% well before the end of the emplacement region (again, non-physical), we can conclude that the role that axial vapor vapor transport has on TH conditions is extremely important.

4.3.2.4 Rock Saturation

To consider how the natural convection cases impact saturation, we again refer to the two dimensional saturation contours presented in Figures 4.7 to 4.12, however now consider case 2 with *moderate convective mixing* shown in Figure 4.11, on page 63. In comparison with the saturation cross-section for case 1 (presented in Figure 4.8) discussed earlier, we observe an overall higher rock saturation, along with higher vapor concentration, in the drift center. This is due to the less effective rate of vapor removal from the drift center in case 2, which is also evident in the smaller saturation profile that is observed in the drift end, an expected result from the reduced amount of vapor arriving in that region in this case. Apparent also are the differences in the temperatures of the surrounding rock formation, with case 2 having slightly higher temperature in the drift center and slightly lower temperature in the drift end. The reduction in the rate of drying of the rock also reduces the heat loss due to the phase change, for case 2 this results in higher temperatures in the drift center as less porewater is undergoing vaporization. Additionally, there is also a reduction in the rate of thermal energy transferred to the drift end simply by a reduction in the the strength of convective mixing.

4.3.3 Flow Processes through the Drift-Wall Boundary

We continue our discussion on the effects that natural convection has on the TH conditions of the surrounding fractured rock. Here, we again consider individual thermal decay outputs from waste canisters. For brevity's sake, now considered are only cases 1 and 2, those bounding the convective processes to be expected in the drift, as they represent realistic thermodynamic conditions expected at the Yucca Mountain (there is no viable vapor mass transport in case 3). For the homogeneous modeling case considered here, the strong capillary forces of the drift wall result in no seepage of liquid water being observed along the drift tunnel for the expected climate conditions at Yucca Mountain. With this, any observed liquid water leaving the drift must be due to condensation, derived from the arrival of water vapor through the transport processes we have discussed previously.

As we now have an understanding of the potentials driving vapor flow into the drift, we inspect directly the resultant flow processes. Plotted in Figure 4.14 is the time-dependent evolution of the log-scale magnitude of the fluxes across the drift wall boundary, including the

(i) vapor fluxes into the drift from the rock formation surrounding *only* the heated emplacement section and the,

(ii) liquid fluxes out of the drift and into the rock formation from *only* the unheated drift ends.

Presented are both case 1 with *strong convective mixing*, and case 2 with *moderate convective mixing*. The fluxes plotted are relative to the percolation flux—they are the ratio of the flux entering or leaving the drift divided by the total percolation flux arriving over the footprint of the heated drift section where the waste is emplaced. For example a relative total vapor flux equal to one means that the mass flux of total vapor entering the heated drift section is equal to the mass flux of the percolation arriving at the drift wall over the heated emplacement section. The flow magnitudes are presented in log-scale along the y-axis, extending from 10 at the top (meaning fluxes there are 10 times that of ambient percolation) to a value of 0.005 at the bottom (where values are 0.5% that of the ambient percolation).

4.3.3.1 Liquid flux from the cool Drift End

To observe the flow leaving the drift, we begin by integrating the liquid water flux draining from the unheated drift end and plot it as a function of time for both the *strong* and *moderate convective mixing* cases (thick, solid blue lines in Figure 4.14).

Case 1 reveals that soon after ventilation ceases, around 75 years after emplacement, the maximum condensate flux draining from the drift end is around 9 times the percolation flux arriving over the entire drift footprint—the magnitude possible because of the additional vaporization of residing pore water in the surrounding rock. This large imbalance in the relative condensation liquid flux diminishes quickly with time; by year 2000 has reached relative values of 100%, and at year 4000 is 25% of the arriving flux of percolation. Notable, as this means that this time, natural convection is still responsible for the transport and condensation of one quarter of the entire flux of arriving percolation water over the heated drift section. The decline observed at year 600 is a result of the step-wise transition to the monsoon climate at that time, thus increasing the infiltration source and reducing the relative condensate flux. Another, less-drastic decline is observed at year 2000, a result of the transition to the glacial climate.

The *moderate convective mixing case* sees much smaller relative condensate fluxes, starting initially around 5 times the arriving percolation flux and decreasing to near

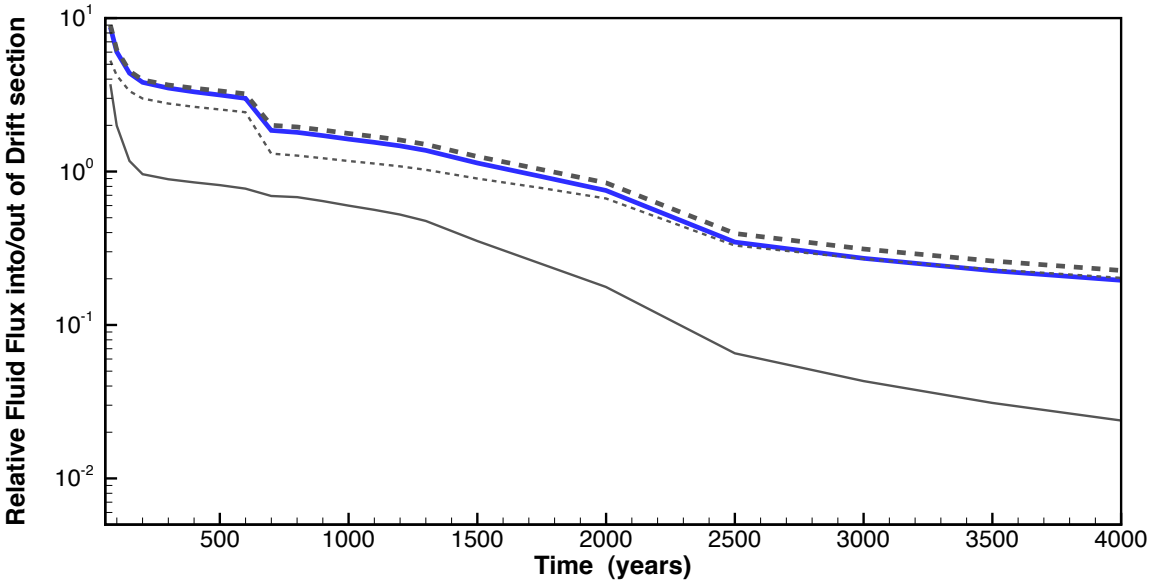

(a) Case 1: with strong convective mixing.

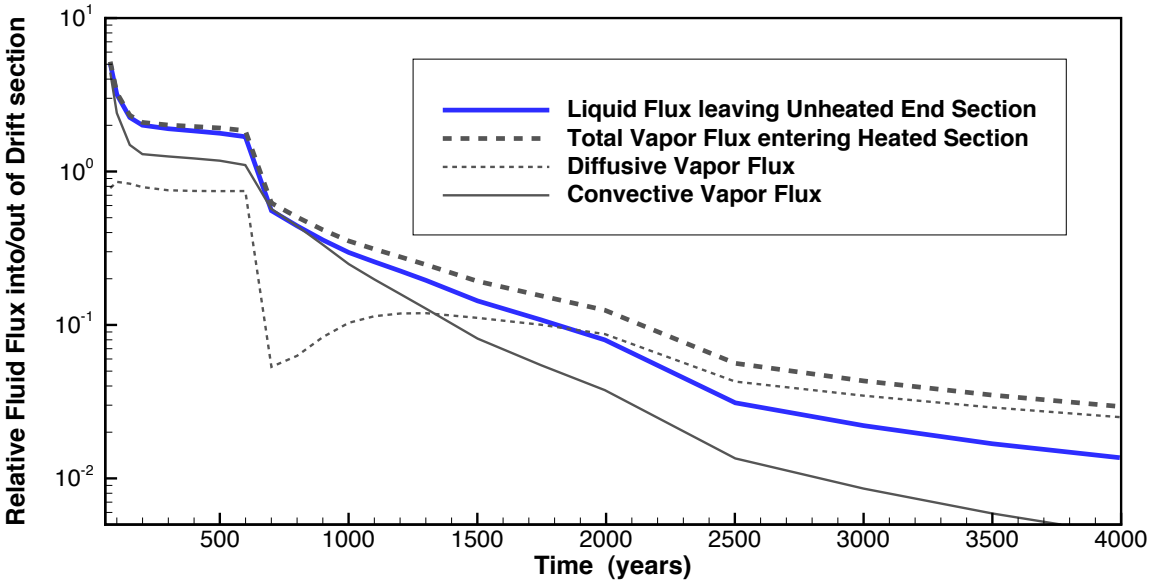

(b) Case 2: with moderate convective mixing

Figure 4.14: Evolution of relative liquid flux (thick, solid, blue line) into the rock formation at the unheated drift end, representing condensation. Evolution of vapor fluxes (diffusive, convective, and total) from heated rock formation to in-drift, representing increased vapor flow due to rock formation heating. Both vapor and liquid flux were normalized by divided by the total flux arriving over the footprint of the heated drift section from ambient percolation.

9% around year 2000, and then 1.5% by the year 4000. The magnitude of the vapor transport due to natural convective mixing in this case is not nearly as large as in case 1. Still, both convective mixing cases produce a considerable amount of vapor transport and condensation in the unheated drift end and contribute to the rock dry-out that occurs during the heated times, for both boiling and non-boiling phases of repository operation.

4.3.3.2 Vapor Flux into the heated Emplacement Section

Now understanding the rates of condensation, logically evoked is the succeeding question: where is vapor produced? While we have already discussed the vapor production in the rock formation briefly, we have yet to analyze the process in detail, and to do so, we have plotted also in Figure 4.14 the integrated total vapor flux (including separately the contributions for convective and diffusive transport) from the formation into the heated section of the drift (represented by thick, dashed grey lines).

We observe from the plot that the magnitude of the total vapor flux in case 1 follows the profile of the liquid condensate, however, is slightly larger at all times. This suggests that most of the vapor flux that enters the heated drift transports, condenses and drains from the drift end. The subtle difference that exists is a result of the small amount of condensate imbibed into the matrix, thus reducing the value of the liquid flux there in comparison to the vapor flux. Further scrutinization reveals that the diffusive flux (the thin dashed grey line) for case 1 dominates the contribution to the total vapor flux into the drift at all times when compared to convective transport, during both boiling (when pressure gradients between the rock and the drift are greatest) and non-boiling phases. This suggests that the strong convective mixing in case 1 maintains a very dry in-drift environment—transport driven via concentration gradients are always greater than the transport driven by pressure differences due to porewater boil-off.

Case 2 follows a similar pattern, however on a smaller magnitude, and when compared to the relative liquid flux leaving the unheated end section, we see a larger difference exists between it and the vapor flux. For example, at 4000 years, the condensate drainage flux is about 1.5% that of the percolation flux, while the vapor flux into the drift is 3%. This means that a this time, only half of the vapor produced is condensed and drained from the drift end, which is likely a result of the amplification of the effects of transport processes in the fractured rock that become apparent at such low relative rates (i.e., $< 3\%$ of arriving percolation). With this, the difference observed is still due to imbibition into the matrix, which continues to show its potential to hold more liquid water in its pore structures. (Note that at certain convective mixing scenarios, this difference might also arise from condensate leaving the *heated* emplacement drift section—condensation near cooler waste packages—as discussed in [65]).

In Case 2, the impact of vapor diffusion is less important initially, meaning that pressure-driven convection due to porewater boil-off dominates the contribution of vapor flow into the drift until the year 1400, when diffusion returns to the dominant role, a result of the declining temperatures of the surrounding rock. Thus, the differences observed between case 1 and case 2 depend on the effectiveness of the diffusive exchange in the initial times after emplacement. Therefore, they compare the capacity for the different convective mixing cases to remove moisture from the surrounding rock not only by removal of vapor from boil-off to the drift ends, but by also contributing to *drying* of the formation by evaporation, in case 1, at all times. In general though, convective mixing in both cases results in a significant rate of vapor flow into the drift region, and at year 500 continues a rate of vapor production larger than the water source from surface inflitration, indicative of its massive drying potential, clearly impacting saturation-dependent processes such as condensation and seepage.

4.3.4 Impact on the in-Drift environment, Relative Humidty

As we have observed how natural convection impacts the rate of flow across the drift wall boundary, we now briefly discuss the time evolution of the relative humidity of the in-drift environment—the parameter driving the rate of diffusion transport from the formation. Figure 4.15 shows the relative humidity of an in-drift element directly above the lumped-parameter waste package element along the length of the drift, and represents the thermodynamic conditions of the open drift environment. Shown in the top figure is the relative humidity for case 1, where it is observed that it remains below 100% in the heated drift section for all simulation times considered, reaching about 90% at year 4000 in the tunnel center. In the unheated drift end, where temperatures are lower, the RH reaches 100% and leads to the condensation we observed in the form of increased saturations of the fracture and matrix domains in this region.

The results for case 2 are shown in the bottom plot, and, in comparison to case 1, show higher levels of relative humidity for each time considered, however, still remain below 100%, with the exception of a few local peaks for times greater than 1000 years after emplacement. Unobservable in the previous case, these peaks represent regions of increased relative humidities near cooler waste canisters, as described in Section 4.2.5, and are a result of the reduced temperatures (and subsequent reduction of saturation vapor pressure) next to the waste packages with lower decay heat outputs. Considered in another modeling study, these decay heat differences, and subsequent relative humidities differences, could result in condensation near the waste canisters[65]. In general these plots show that both convective mixing cases—particularly case 1—have the potential for long term-drying of the drift wall and formation and for reducing the likelihood of seepage events (as considered in the following chapter).

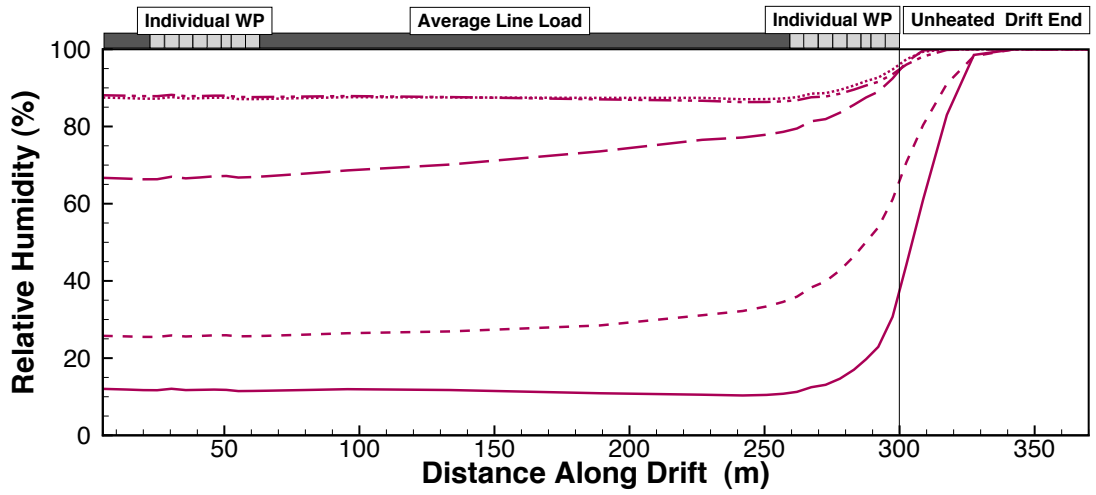

(a) Case 1: with strong convective mixing.

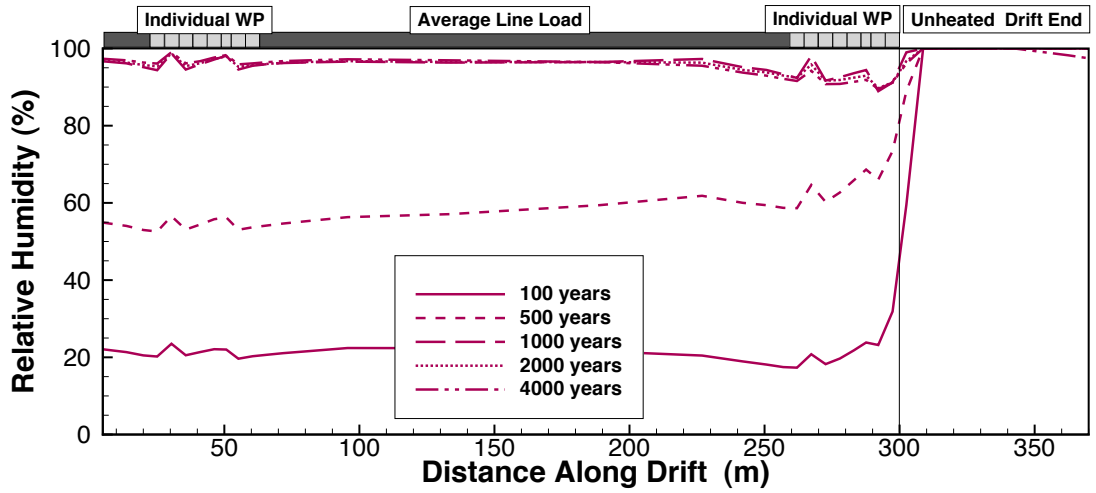

(b) Case 2: with moderate convective mixing.

Figure 4.15: Relative humidity along drift crown.

4.4 Conclusions

We presented in this chapter a numerical study that accounted for the impact of natural convective processes in the near field environment at Yucca Mountain based off on the results of earlier investigations[17, 65]. Following methodologies from previous studies[55, 58], the natural convection of the in-drift domain was approximated as a binary diffusion process, with an enhanced dispersion parameter calculated to incorporate average transport processes predicted from CFD analysis. Additionally, boundary layer correlations accounted for enhanced heat and mass transport at the

in-drift surfaces[36], and TOUGH2 was modified to allow definitions of such connections. Different convective mixing cases were considered, bounding the effects of axial transport, with the *strong* and *moderate convective mixing cases* representing the upper and lower limits.

In general, in-drift axial heat and transport from natural convection was found to cause,

(i) a desaturation of the fractured rock, caused by

(ii) an increase of the vaporization of the pore water, driven by

(iii) a reduction of the relative humidity of the in-drift environment.

This reduction in RH was maintained through the transport and condensation of water vapor produced in the heated drift ends, and existed for both cases of convective mixing. Specifically, the *strong convective mixing* maintained a much lower relative humidity than other cases—testament to its ability to transport vapor more effectively. Still, in terms of repository performance, both convective mixing cases result in TH conditions beneficial to the waste storage environment and would have significant impact on reducing seepage and condensation in the heated drift sections.

We emphasize that while the approximation of natural convection as a diffusive process allows for modeling average response of the formation and in-drift environment, it cannot be expected to yield results of unique turbulent effects that would occur in the open air spaces. Still, for understanding how vapor transport impacts repository behavior, it has provided useful insight on the complex processes. Because of the sensitivity the model has to the value of the dispersion coefficient, it is recommended that future research endeavors focus on better approximating this parameter—including bench-scale experiments.

This chapter laid the foundation for understanding of the transport processes at Yucca Mountain, the modeling methodologies to describe them, and the significance of the predicted conditions. The results presented are crucial in quantifying other processes that are dependent on the TH conditions of the in-drift environment, such as seepage, and indeed are used in another numerical study on the impact on drift seepage, presented in Chapter 5.

Chapter 5

Drift Seepage

5.1 Description

The decay heat from radioactive waste that is to be disposed in the once proposed geologic repository at Yucca Mountain will significantly influence the moisture conditions in the fractured rock near emplacement tunnels (drifts). Additionally, large-scale convective cells will form in the open-air drifts and will serve as an important mechanism for the transport of vaporized pore water from the fractured rock in the heated drift center to the cooler drift end. Such convective processes would also impact drift seepage, as evaporation could reduce the build up of liquid water near the tunnel wall. Characterizing and understanding these liquid water and vapor transport processes is critical for evaluating the performance of the repository, in terms of water-induced canister corrosion and subsequent radionuclide containment.

As described in Chapter 4, previous computational fluid dynamic studies have shown the formation of large-scale natural convections cells along the length of the drifts, a result of temperature differences between the heated and cool sections of the drift[55]. It was assumed that these convective cells could provide an effective mechanism for moisture transport of pore water, evaporated from the rock formation, from the heated drift centers to the cool drift ends (where no waste is emplaced).

We performed studies to understand such processes, by applying a previously developed enhanced version of TOUGH2 [45] that solves for natural convection in the drift domain, including the in-drift environment and the surrounding fractured rock[17, 60]. Results from these studies showed a large increase in the moisture transport away from the heated drift center toward the cooler drift ends for the time period that thermal perturbation from decay heat prevails, and a subsequent reduction in the relative humidity (RH) of the in-drift environment, suggesting a substantial increase in the evaporative potential at the drift wall when compared to a case with no natural convection.

Presented in this chapter is a new procedure for investigating this complex coupled behavior between natural convection and its impact on drift seepage. In the context of the Yucca Mountain repository, seepage refers to the flow of liquid water into open emplacement drifts, or simply the dripping of liquid water from the tunnel walls, as shown in Figure 5.1. Previous studies investigating thermally driven flow processes and their impact on seepage neglected the presence of open drifts as conduits for gas and vapor transport along the drift axis[47], thus neglecting an important mechanism for seepage reduction.

To better understand what role the natural convective processes might have on minimizing seepage of percolation water into the tunnels, we developed a high-resolution seepage model based on existing seepage models; however, now additionally employing the new natural convection module. Because an increased grid resolution was needed to allow for heterogeneity in element permeability near the drift wall, computational limitations prevented simulation of an entire drift in the new model. Instead, we used the time dependent in-drift response (temperature, pressure, and relative humidity) from the previous full-drift and rock model described in Chapter 4 as a Dirichlet boundary source for a short drift section represented in a high-resolution seepage model. To account for future variations in subsurface flow expected at Yucca Mountain, the simulation time period of 5,000 years after emplacement covers three expected climate stages, with present-day climate up to 600 years in the future, followed by a wetter monsoon climate up to 2,000 years, and an even wetter glacial transition climate thereafter. Climate periods are implemented into the model in the terms of stepwise increases in net surface infiltration rates.

5.2 Physical Processes

5.2.1 Natural Convection Processes

As explained in greater detail in the previous chapter, vapor entering the emplacement drifts from the fractured porous rock is subject to effective radial and axial[1] mixing and transport as a result of natural convection processes. Axial mixing can reduce the overall moisture content in heated drift sections because of the presence of the unheated drift ends (turnouts). Principles of thermodynamics suggest that the maximum amount of vapor that can be present in air decreases with declining temperature. Thus, the warm vapor-rich gases moving from heated drift sections toward the drift turnouts—caused by natural convection processes—will be depleted of most of their vapor content through condensation on cooler rock surfaces. The condensate will then drain away from the repository into underlying rock units. At the same time, vapor-poor gas will circulate back towards the center of the drift (where the

[1]The *axial* direction refers to the axis along the length of the drift, and, in the case of a drift a Yucca mountain, is orders of magnitude longer than in the radial direction.

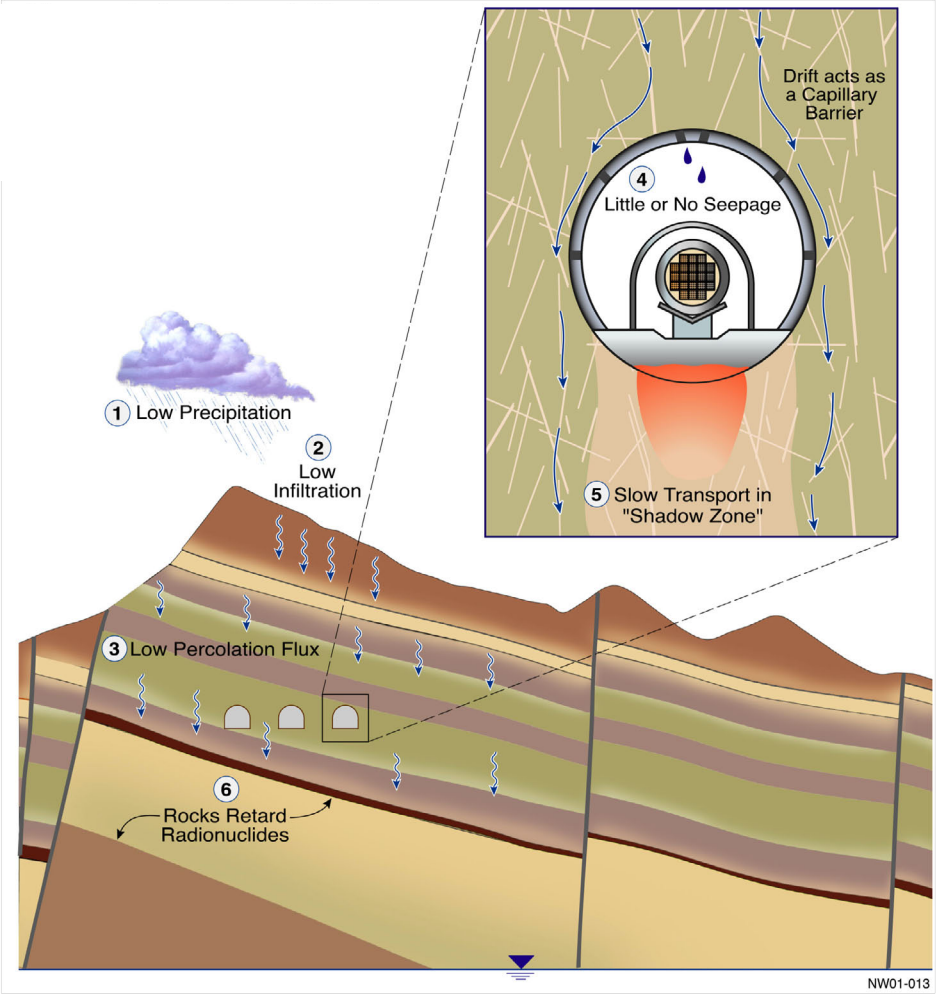

Figure 5.1: Schematic of water transport processes expected in the Yucca Mountain repository and around the drift, including percolation and seepage. Emphasized, specifically, are beneficial qualities for sequestration of radionuclides, from the small quantity and low rate of water transport, including: 1) Low rate of precipitation from arid climate, 2) Low rate of infiltration, 3) Low rate of percolation through unsaturated zone region, reducing advective transport of radionuclides in this region. 4) Little or expected seepage, due to capillary barrier, 5) Minimal transport in *Shadow Zone*, due to extremely reduced rate of water transport, 6) Retardation in geological layers.

waste is emplaced), thereby reducing the moisture content of the air mixture in these areas[17, 65].

5.2.2 Seepage Processes

Of the modest amount of precipitation in the Yucca Mountain region (about 170 mm/yr)[11], a small portion of it infiltrates into the ground surface (∼6 mm/yr at current climate conditions) above the repository[12], percolates downward through the unsaturated rock, through both fracture and matrix domains and eventually reaches the drift wall. Under the flow and thermodynamic conditions expected at Yucca Mountain, the major fraction of this percolation water does not seep, but is rather diverted around the drift opening due to many seepage barriers (described below) present in the surrounding rock. Still possible are physical processes, occurring outside of those expected, which might create conditions allowing seepage to occur. What these processes are and how they might impact seepage is the focus of discussion that follows.

5.2.2.1 Ambient Seepage

Ambient seepage refers to the amount of seepage occurring during non-heated conditions, representing the long-term situation at Yucca Mountain when the initial perturbation from decay heat has ceased. As such, ambient seepage serves as a baseline to compare model response during the thermally perturbed time period. Parameters that have the largest impact on seepage at ambient temperatures are:

- the amount of percolation flux above the drifts (amount of water arriving at the drift wall), including effects of preferential flow which could increase percolation in certain drift sections
- the local heterogeneity of the fracture flow field (the spatial variability of fracture permeability close to the drift opening), and the
- and the capillary strength of the fractures close to the wall (defining the amount of water the rock can hold)[70].

5.2.2.2 Thermal Seepage

Thermal seepage refers to seepage during the time period that the flow around drifts is perturbed from heating due to radioactive decay. Heating of the rock creates additional temperature-driven physical processes that play a role in redistribution of water in the surrounding rock. Then, to consider a repository scenario with thermal seepage,

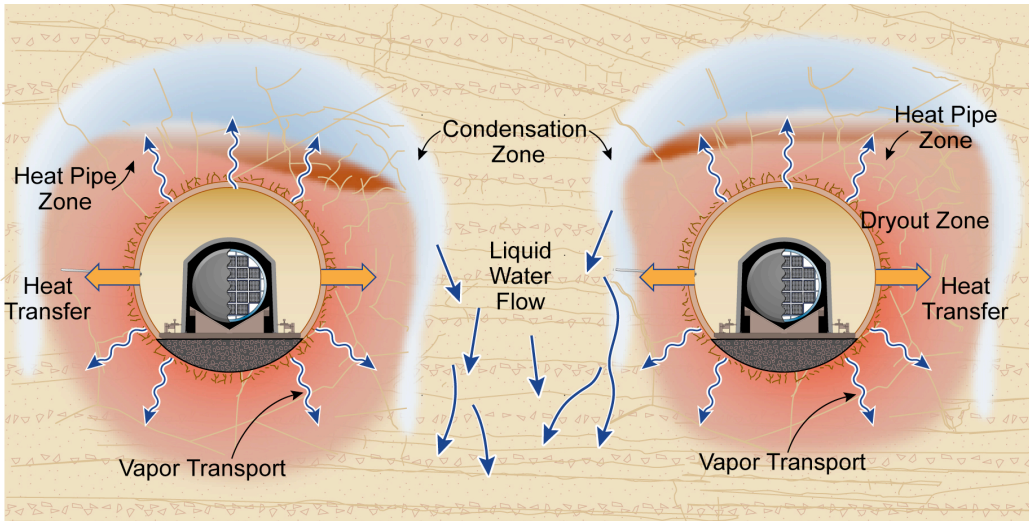

Figure 5.2: Thermal-hydrologic processes near two adjacent drifts during boiling phase of emplacement (from [46] §6.1.2). (Distance between drifts not to scale).

we must investigate all possible impacts on seepage, both processes that increase or reduce the amount of liquid water from existing at the drift wall and/or from seeping into the drifts. It is important to consider that while water might be redistributed, it is not removed from the system. We considered three barriers—processes that remove or reduce liquid water flow into the drifts—for the study.

Vaporization Barrier: The vaporization barrier occurs when the surrounding rock is above boiling temperatures, forming a superheated dryout zone around the drifts (Figure 5.2). This serves as a barrier to seepage as all percolating liquid water is vaporized prior to reaching the drift wall. It has been shown that the flow of percolation water is mostly diverted around these dryout regions, into a below-boiling zone existing between two drifts[46]. The vaporization barrier serves as the relevant barrier to seepage until rock temperatures return to below boiling, establishing thermodynamic conditions at which liquid water can exist at the drift wall. It is at this stage that the rock properties at the drift wall impact the likelihood of seepage.

Capillary Barrier: Water tends to divert around underground openings because of capillarity, a phenomenon well known as the capillary barrier. Indeed, this phenomenon is explored by many inquisitive minds with the investigation of the wetting of a dry kitchen sponge by a small flow of water. It is observed that there will be no dripping from the underside of the sponge until a region forms there that has been completely wetted, thus reducing the capacity for the pore spaces within the sponge to

hold any additional water. In unsaturated zone transport, a similar condition arises, for example, when coarse-grained soils are overlain by fine-grained soils.

What is the mechanism driving this phenomenon? Adhesive forces between water and the rock grain surface drive water to cover and hold to these surfaces, creating a potential against the force of gravity. In general, the fine-grained material exhibits stronger capillarity because the ratio of the pore surface area to total material volume is much larger than in the coarse-grain material. With a larger surface area over which the water adheres to per unit volume, the fine-grained material more forcefully holds to liquid water stored in its pore structures.

Across this boundary between the two mediums, the stronger negative capillary pressure developed in the fine-grained material prevents water from entering the larger pores of the underlying coarse-grained material[70]. In this scenario, the capillary barrier can be overcome by decreasing capillary pressure in the small-grained material so that it is equal to or less than that of the coarse-grained material. This can only occur by increasing the saturation[2] in the fine-grained material, so that, with the loss of pore space to hold additional water, the adhesive forces also decrease and, in turn, reduce the capillary pressure. In the limit-approaching case of infinite pore size of the coarse-grained material (such as an open tunnel), seepage into the drift can only occur if the capillary pressure in the rock nearby the drift walls becomes zero—the case when the rock has reached saturation.

In this context, one must consider the large differences in capillarity between the fracture and matrix continua (the matrix having a much stronger capillarity due to its small pore size) in the fractured porous rock at Yucca Mountain. This difference means that the matrix will strongly imbibe liquid water from fractures, and must be nearly saturated (reducing the capillary pressure of the matrix) before any significant buildup of liquid water can occur in the fractures. However, even with the matrix being close to saturated, seepage is only expected to occur from the fracture domain. This is because the capillarity of the saturated matrix is still significantly stronger than that of the fractures.

Additionally, an increase in the local saturation in the rock can occur due to a disturbance to the flow field (caused by the presence of the drift opening) and more importantly by spatial heterogeneity that promotes channelized flow and local ponding[3]. Variations in fracture permeability along the drift wall allow for regions of increased (or decreased) local saturation, along with changes in the flux of liquid water along the drift wall—creating conditions possibly beneficial for seepage.

[2]Ratio of the volume of liquid to the total volume of a pore space $S_l = V_{liquid}/V_{pore}$, theoretically ranges in value from 0 to 1.

[3]Here, ponding refers to a scenario with a local region of rock being fully saturated in an otherwise unsaturated medium[70].

Evaporation Barrier: Finally, evaporation of water at the drift wall, enhanced by natural convection transport as described in Section 4.1.2, would also serve as a barrier in limiting seepage. Liquid water accumulating at the drift-wall surface, which might overcome the capillary barrier and seep, would be subject to removal by evaporation and be transported via natural convection along the tunnel to be condensed in the cooler regions in the drift end, as shown in Figure 4.2. Although the vaporization and capillary barrier have been explored in great detail in previous studies[46, 47], the effect of an evaporation barrier has only recently been investigated for ambient conditions[37], and has yet to be considered for seepage modeling studies during the emplacement period, when natural convection effects would be most dominant.

The magnitude of this evaporation process and its role in seepage reduction is the focus of this research effort. This, combined with the previous two barrier systems, will provide a better understanding of how natural convection and the subsequent vapor transport in the axial direction might further reduce the likelihood of seepage at the Yucca Mountain repository.

5.3 Modeling Approach

During times with thermal perturbations due to decay heat, the in-drift environment is impacted by axial vapor transport via natural convection. These processes occur over the length of the entire drift and, therefore, require the modeling of a full-scale drift tunnel (including drift turnout, where no waste is emplaced) along with the surrounding host rock.

Developing a model that captures and solves both seepage and natural convection processes simultaneously would require an extremely complex discretization and significant computational resources. Instead we utilize a unique method that involves two models of different spatial scale. The first model is our previously developed natural convection model for the full drift and the surrounding rock[17] (*nat-co*), which simulates the time-varying thermodynamic response of the full in-drift domain. The second model is a high-resolution seepage model covering a much shorter drift section, which specifically deals with smaller-scale, seepage-relevant processes (referred from here on as the *seepage model*). The *seepage model* uses results from the *nat-co model* as a time-dependent boundary condition (temperature, pressure, and relative humidity) for the in-drift domain. By implementing this time-dependent response, we are not required to model the entire length of the drift in the seepage model, a significant advantage as it reduces the grid complexity by an order of magnitude. Because these time-dependent in-drift boundary conditions—generated from the *nat-co model*—will have a large impact on seepage, we shall summarize important aspects of this model and follow with details of the *seepage model*.

Table 5.1: Effective mass dispersion coefficients prescribed in *nat-co* model.

Cases	Descriptions	Dispersion Coefficient $\left[\frac{\mathrm{m}^2}{\mathrm{s}}\right]$
Case 1:	Strong convective mixing	0.1
Case 2:	Moderate convective mixing	0.004
Case 3:	No convective mixing (binary diffusion only)	2.14×10^{-5}

5.3.1 *Nat-Co Model*: The Previous Full-Drift and Rock Natural Convection Model

As discussed in detail in Chapter 4, but briefly reviewed here again for clarity, the *nat-co model* was run for a time period of 5,000 years considering three convective mixing cases, as shown in Table 5.1, with the effective mass dispersion values based off of results from a previous CFD model investigating the magnitude of natural convective mixing[36, 65]. Cases 1 and 2 represent the variability and uncertainty about the magnitude of convective mixing; Case 3 is a comparison case, where convective mixing is ignored (and thus binary diffusion is the only contribution to the effective mass dispersion coefficient).

The results of this study showed that Case 1 (strong convective mixing) causes considerable transport of vapor from heated drift sections to the unheated end, and gives rise to reduced relative humidity along the length of the drift when compared to the case with moderate and no convective transport. It is this time-varying response (temperature, pressure, and RH) that will serve as a boundary condition input for the seepage model. We expect that the evaporative potential associated with the strong convective mixing case will increase the transfer of moisture from the fractured rock mass into the drifts and thus may reduce seepage at the drift wall.

5.3.2 *Seepage Model*: High-Resolution Seepage Model for Seepage Processes

When considering the impact of natural convection, we can assume that the in-drift is well-mixed, or that there is no significant change in the local thermodynamic conditions of the in-drift domain nearby a seepage event. We consider this by developing a quasi-3D model, with boundary conditions prescribed in the same manner as the *nat-co model*. The high-resolution *seepage model*, based on existing TH seepage models[46], employs all the same framework as the *nat-co model* explained in Section 4.2.1, however, with additional modeling details as follows.

Modeling Framework for Fractured Rock Mass

The model extends from the mountain surface to the water table, yet has a more finely gridded mesh in the x-z plane (Figure 5.3), allowing for prescribing a heterogeneous fracture permeability field to the region of rock next to the drift wall (fracture permeability was constant in the *nat-co model*). The higher resolution mesh also allows prescribing of a small capillary-strength parameter to a narrow, select region of rock elements adjacent to the drift wall. This is a conservative approximation for seepage modeling as it reduces the ability for the rock at the drift wall to hold water. Additionally, the mesh includes variation in the geologic strata representing varying rock properties from borehole samples[71]. The drift vicinity in this model resides in the Topopah Spring Tuff lower lithophysal geologic unit, chosen as a majority of the repository resides within this type of geologic layer.

Instead of including the entire length of the drift in the model (as was done in the previous *nat-co* model), it now incorporates only a 25 meter long section of the drift, divided into nine vertical layers (Figure 5.4). Still with these simplifications, the grid contains about 17,000 grid blocks and 70,000 connections, considerably more than in the previous *nat-co* model. To accommodate this additional amount of calculations, we used a parallelized version of the TOUGH2 code[72], allowing calculations to be performed over computer clusters[4], greatly reducing simulation times[5].

As described in Section 6.2.3.2.1 of Birkholzer et al.[46], multiple realizations of a heterogeneous fracture permeability field in this study were generated using a stochastic method, with spatial variability based on small-scale air injection tests conducted in the underground test tunnel at Yucca Mountain. The specific realization selected for the fracture permeability field contains a highly permeable region next to a low-permeability region at the rock-drift interface—a scenario promoting seepage as it allows for local ponding at the wall. It is this region of elements (represented in Figure 5.4, *Local conditions at drift wall with highest seepage potential*) that will be observed in greater detail.

Another main component of seepage modeling is the implementation of a small capillary-strength parameter for the fracture continuum in drift vicinity. This parameter relates the fracture saturation to the capillary pressure; it was derived in previous work[74] from inverse modeling and calibration to niche liquid-release tests conducted at Yucca Mountain[75, 76]. This calibrated parameter incorporates not just the physical capillarity of the fracture network surrounding the tunnels, but also potential effects

[4]Parallel computing is a form of computation in which many calculations are carried out simultaneously, operating on the principle that large problems can often be divided into smaller ones, which are then solved concurrently–in parallel[73].

[5]Initial simulations with the seepage model run on the serial (single-processor) version of TOUGH2 required ~90 days calculation time. This was reduced to only a few days using the parallelized code running on a 20-core Linux cluster.

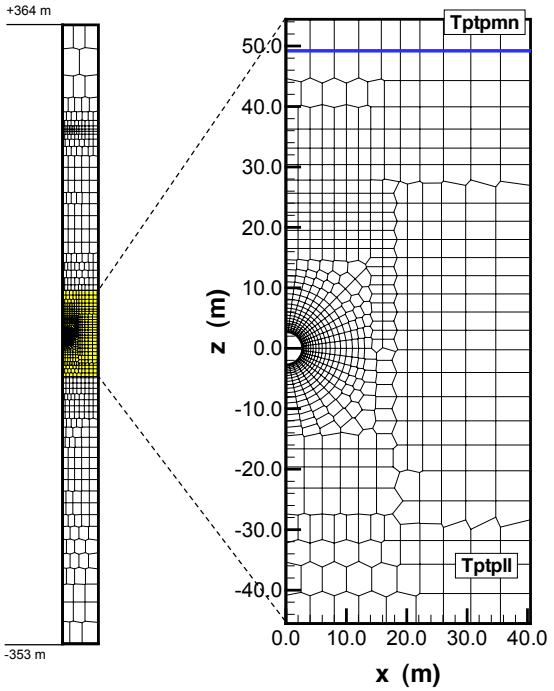

(a) X-Z plane view of grid discretization, from upper model surface boundary at +364 meters above drift horizon to -353 meters below drift horizon, at the water table surface.

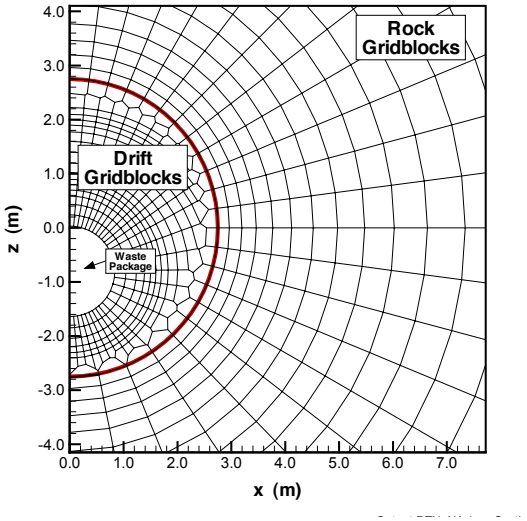

(b) Detailed X-Z plane view of in-drift (region labeled *Drift Gridblocks*) and surrounding rock discretization, including waste package element and drift wall (dark line shows drift wall boundary).

Figure 5.3: X-Z plane view of grid discretization

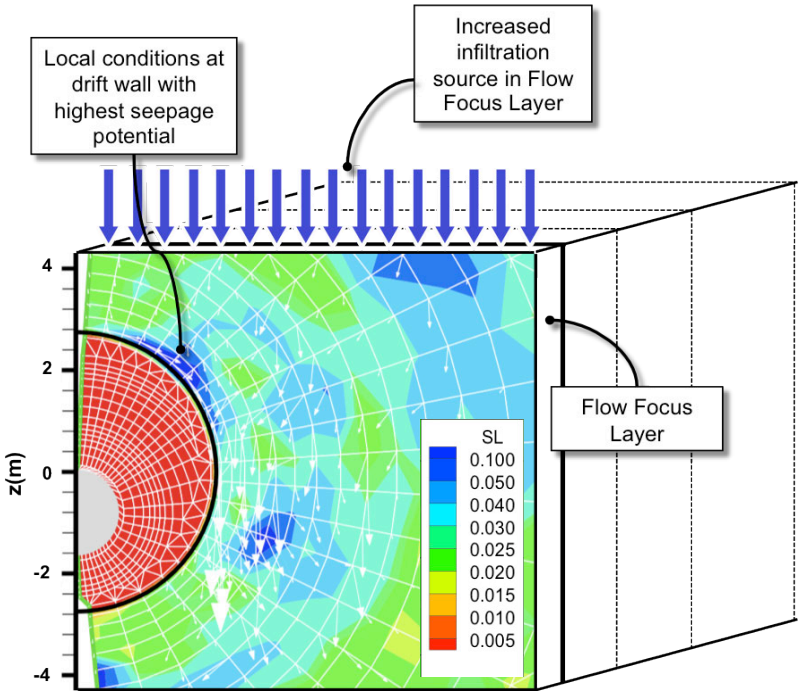

Figure 5.4: A sample contour plot of the fracture saturation in the drift vicinity displaying increased saturations (dark blue regions) due to heterogeneity in fracture permeability. Arrow field represents magnitude of percolation flow around the rock surrounding the drift.

from permeability changes due to excavation effects, small-scale wall roughness, high-frequency episodicity from small-scale flow processes, film flow, drop formation, discrete fractures that may terminate at the wall, artifacts of finite discretization, and, effects from lithophysal cavities. The magnitude of the capillary strength parameter affects the possibility of seepage from occurring—a smaller value promotes seepage while a larger value reduces seepage. As explained previously, seepage from the rock matrix is not expected because of the very strong capillarity existing in that domain. Other rock properties including soil-moisture characteristic curves and thermal characteristics are listed in Table 5.2.

Modeling Framework for Capillary Barrier Behavior at the Drift Wall

A key element for seepage modeling is the specific seepage boundary condition implemented for the fracture continuum at the rock-drift interface. In the model, we represent drifts as open cavities with a zero capillary-strength parameter. For a vertical connection between the fracture continuum at the drift crown and the drift, downward seepage occurs when the threshold capillary pressure at the last node adjacent to the opening exceeds (is less negative than) a value of $-\rho g \Delta z$, where ρ is

Table 5.2: Summary of hydrogeological and thermal input values of fractured rock mass, including Matrix properties, Fracture properties, and Fracture-Matrix Geometry properties.

Parameter	**Units**	**Matrix**	**Fracture**
Permeability	m^2	4.48×10^{-18}	9.10×10^{-13}
Permeability (wall layer)	m^2	4.5×10^{-15}	–
Porosity	–	0.1486	9.6×10^{-3}
Rock grain density	kg/m^3	2325	–
Rock grain specific heat	$J/kg\,K$	985	–
Dry thermal conductivity	$W/m\,K$	1.278	–
Wet thermal conductivity	$W/m\,K$	1.890	–
Tortuosity	–	0.20	–
van Genuchten parameter, α	Pa	9.26×10^4	9.71×10^3
Capillary-strength parameter for fractures in drift vicinity, α	Pa	–	589
van Genuchten parameter, **m**	–	0.216	0.633
residual liquid saturation	–	0.12	0.01
		Fracture-Matrix Geometry	
Volume Fraction of Fractures	–	0.0097	
Fracture-Matrix interface area	m^2/m^3	9.8	
Representative distance between fracture and matrix blocks	m	0.0528	

density, g is gravitational acceleration, and Δz denotes the distance between the last formation node and the first drift node, the latter placed inside the drift immediately at the rock-drift interface. According to this relationship, the fracture continuum close to the drift wall does not need to be fully saturated for seepage to commence. For the properties used in this simulation, seepage conditions exist when the fracture saturation near the wall exceeds about 0.5. Also, the threshold pressure for seepage increases slightly (becomes less negative) with elevated temperatures because of liquid density changes. Therefore, at higher temperatures, the threshold saturation for seepage may be slightly higher than 0.5.

Conceptually, setting a non-zero nodal distance Δz at the rock-drift interface (and thus having a less than unity threshold saturation for seepage to occur) accounts for the possible presence of discrete fracture segments intersected by the drift opening. If these segments do not extend far enough laterally or do not have a lateral connection to other fractures, the water carried in these segments cannot bypass the opening.

As a result, the probability for seepage would increase beyond the value expected for a porous formation, depending on whether the gravity-driven flow in the discrete fracture segment can overcome the capillary barrier. Finsterle et al.[74] propose to use a value of 0.05m as representative for the fracture geometry observed in drifts at Yucca Mountain. A similar rate is chosen in this study.

Modeling Framework for Evaporative Barrier Behavior at the Drift Wall

Before dripping, liquid water that overcomes the capillary barrier and encounters the drift wall is likely to form a film over the local surface of the wall, which was demonstrated in seepage field experiments conducted at Yucca Mountain[37]. The question whether a liquid film forms or not as fracture flow approaches the drift wall is quite relevant in this paper because it heavily influences the area available for evaporative drying. If a liquid film forms, evaporation occurs over the locally wet area of the drift wall. If not, evaporation can only occur over the small cross-sectional area where the flowing fracture intersects the drift. The model results described in this paper are based on the assumption that film evaporation occurs at the drift wall, and that the area available for such film evaporation is proportional to the fracture saturation and the drift wall surface of the seeping gridblock. However, we also note that we performed alternative simulation cases assuming that a liquid film does not form. In the latter case, evaporative drying is almost negligible, independent of the relative humidity conditions in the drifts, due to the very small representative area over which the model assumes evaporation to occur.

5.3.3 Model Boundary Conditions

Seepage is a local event, and occurs over regions of rock on the order of less than a meter. While the in-drift thermodynamic conditions are dependent on the amount of percolation water evaporated into the drift (during sub-boiling conditions), the additional amount of water arriving due to a seepage event is small when compared to the total amount of water arriving and evaporating over the length of the drift.

Seepage is most likely to occur in drift regions where the local percolation flux is much higher than the average percolation, a possible result of intermediate-scale heterogeneity leading to flow focusing. To account for the possibility of locally higher flux arriving at a drift region, we consider three flow focusing cases by multiplying the average input percolation flux prescribed at the model upper boundary by factors of 10 and 20 (Table 5.3). These three cases are referred to as *no flow focusing*, *flow focusing 10*, and *flow focusing 20* cases, respectively.

We restrict the flux increase to a thin (0.25 m) vertical layer in the model, preventing any transport of liquid between this layer and the adjacent layer (Figure 5.4), thus ensuring that the high-percolation conditions imposed at the top boundary of the model

Table 5.3: Flow focusing cases and corresponding infiltration/percolation input fluxes.

	Percolation rate in layer of locally focused flux [mm/yr]		
Cases	**Modern (0-600 years)**	**Monsoon (600-2000 years)**	**Glacial (>2000 years)**
No Flow Focusing	6.0	16.0	25.0
Flow Focusing × 10	60.0	160.0	250.0
Flow Focusing × 20	120.0	320.0	500.0

propagate all the way down to the drifts—a modeling method to create conditions of preferential fast-flow in a fracture zone that intersects or comes close to the drift wall. Heat transfer, however, is still allowed in the axial direction, ensuring that the the large volumes of surrounding rock properly contribute heat to the heavily saturated region/layer. It is this layer of locally focused flux, and the region with increased fracture permeability along the drift wall—conditions best for seepage to occur—that is significant to this study.

As described previously, for treatment of the in-drift we prescribe the results of the *nat-co* model (the thermodynamic conditions of an in-drift element above the waste package that is located near the center of the tunnel, see discussion in Section 4.3.2 on page 65) to the waste package element (Figure 5.3). This time-dependent, thermodynamic, Dirichlet boundary condition allows for maintaining the in-drift environment to expected values for normal infiltration rates while still allowing a balance to occur between the in-drift and fractured rock. Prescribed values include the temperature, pressure, and relative humidity (Figure 5.5).

5.4 Model Results

The goal of this study is to evaluate the potential impact that natural convection has on drift seepage, which is largely affected by the local in-drift thermodynamic conditions at the drift wall in a seepage-prone region. Again, all model results presented below are from the vertical layer of locally focused flow, where average percolation rates have been adjusted by flow focusing factors of 1, 10, and 20, respectively.

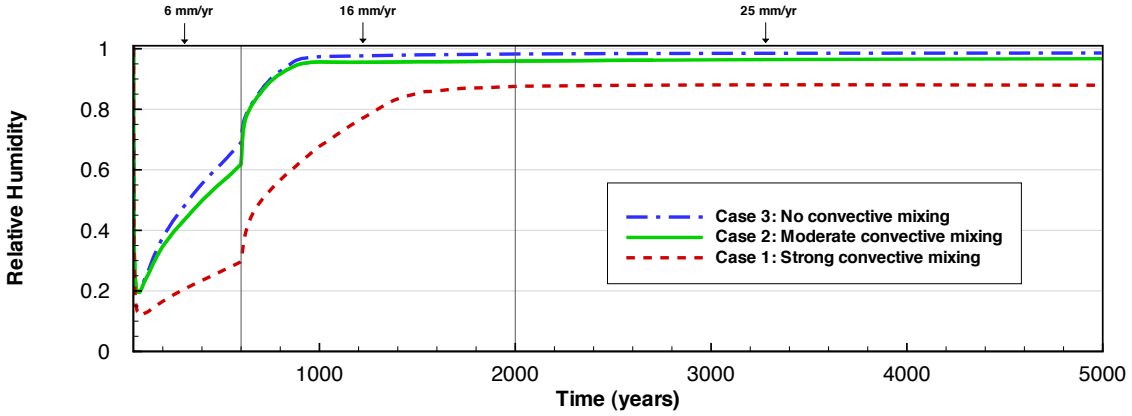

Figure 5.5: Evolution of relative humidity (RH) of in-drift element at the drift center in the full-drift & rock natural convection model (*nat-co*) for all three convective mixing cases. Vertical grey lines indicate stepwise changes in percolation flux caused by expected future climate changes at 600 years and 2000 years after emplacement.

5.4.1 Temperature

First, we will look at temperature response at the drift wall from 50 to 5000 years, the time scale for all future plots. We show in Figure 5.6 the temperature response in the most seepage prone element (that having the largest local saturation buildup) at the drift wall, represented by the solid lines and also the temperature of the time-dependent in-drift Dirichlet boundary condition, represented by the dashed lines (only in Figure 5.6c).

Temperatures max out around 150°C shortly early after emplacement of waste, then cool to the boiling temperature (96°C) around year 800, and eventually drop to below 60°C by year 5000. Similar behaviors are observed in all flow focusing cases, with slightly lower temperatures in the *flow focusing 20 case* due to the increase in the percolation flux. It is however noted that the temperatures are hardly affected by variations in flow-focusing, testament to the effective transfer of heat from the waste packages to the seepage wall location via thermal radiation and also heat conduction through the rock from the adjacent vertical layers. This is consistent with our assumption that seepage would occur over a very small region of the drift, and as such, have little impact on the local temperatures.

The parameter having the largest impact on the temperature is the magnitude of convective mixing. As discussed in Section 4.3.2.1, we had observed the temperature of the drift-wall element for the *strong convective mixing case* being slightly lower than the temperature for the other two convective mixing cases during times when the temperatures were below boiling. Again, this is due to the more effective heat

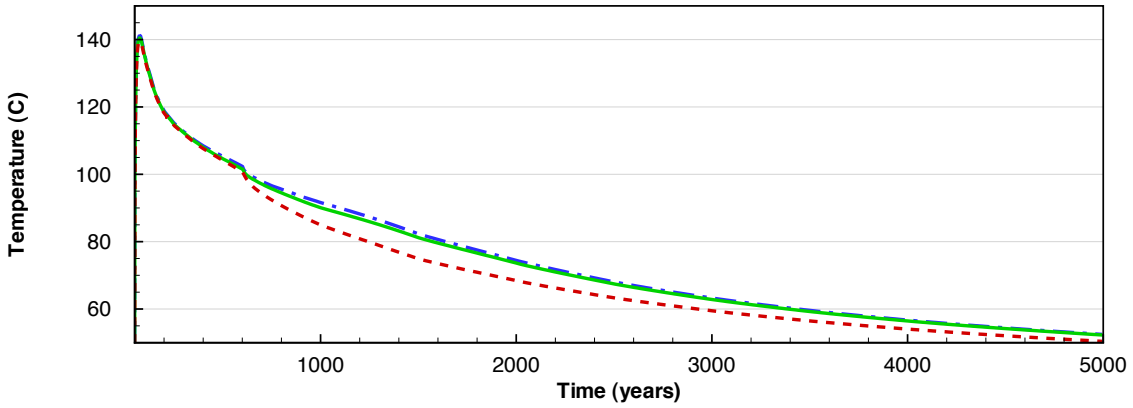

(a) No flow focusing case

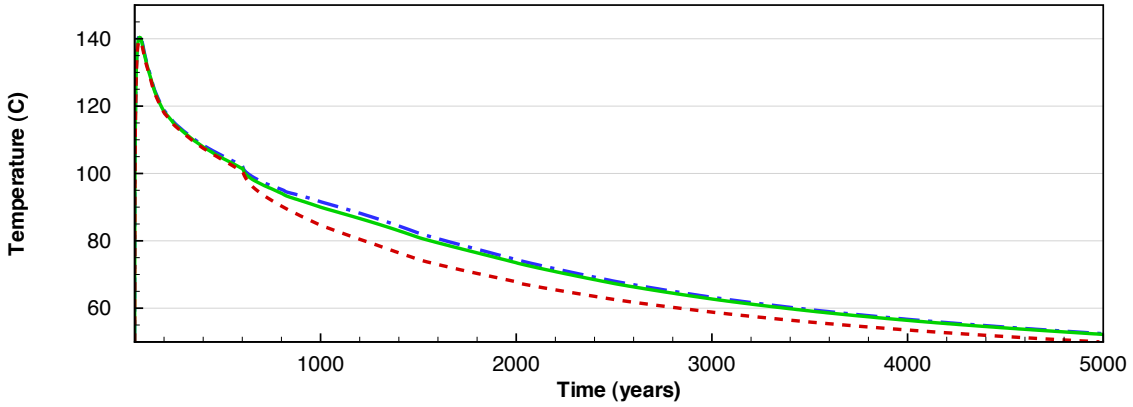

(b) Flow focusing 10 case

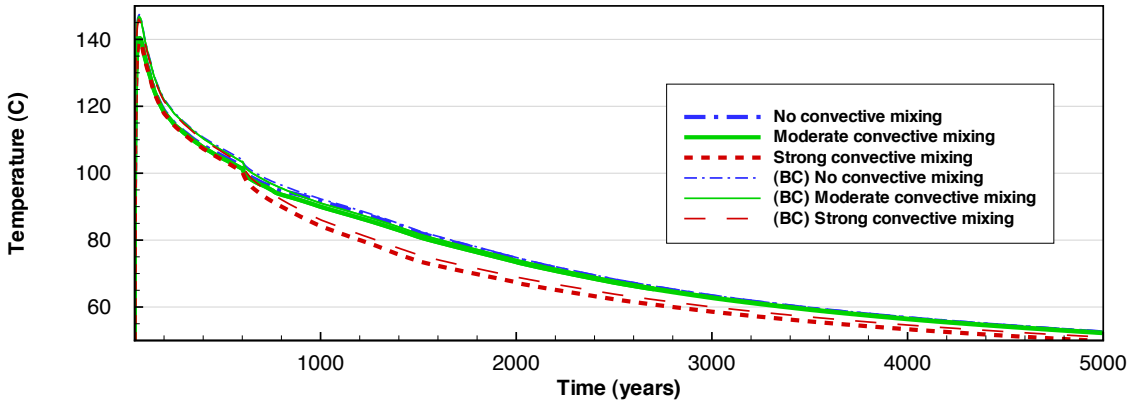

(c) Flow focusing 20 case.

Figure 5.6: Temperature evolution in seepage-prone element at drift wall (solid line) and boundary source (dashed line) for (a) no flow focusing, (b) flow focusing 10, and (c) flow focusing 20 cases.

removal from the drift center due to enhanced axial vapor transport in the *strong convective mixing case*.

5.4.2 Matrix Saturation

As discussed previously, saturations in the rock matrix do not directly correspond to an understanding of seepage due to the large difference in the capillarity between the two continua. They do, however, provide an insight into when the fractures are able to resaturate (the saturation of the fractures create conditions for seepage) and also provide an understanding of vapor transport between the rock wall and in-drift (discussed in Section 5.4.5). We depict in Figure 5.7 the matrix saturation in the seepage-prone element for the varying flow-focusing cases.

In these plots, transitions between current and future climate stages are distinguished by vertical grey lines on the plot. For the *no-flow focusing* scenario (Figure 5.7a), resaturation does not occur in the case of *no convective mixing* until around year 340. Similarly, the *moderate convective mixing case* sees initial resaturation occurring around year 400. Interestingly, both these times correspond to temperatures well above the boiling point, at 107°C and 110°C, respectively. The strong capillarity in the hot, desaturated matrix competes with the boiling point of water at this depth, increasing it, allowing a small presence of liquid water to exist in the matrix pores at such high temperatures.

The *strong convective mixing case* does not see resaturation occur until much later, around year 700 (corresponding to a temperature of 94°C), a result of the effective drying of the rock wall from the low relative humidity of the in-drift environment. This drying is further exemplified when observing the magnitude of saturation achieved in the various convective mixing cases, with the *strong convective mixing* (dashed line) resulting in a much lower matrix saturation than in the cases with *no* or *moderate convective mixing*. This is apparent across all flow-focusing scenarios, and is a result of the ability for natural convection to reduce the relative humidity in the air, and remove moisture from the surrounding rock.

For the other flow focusing scenarios (Figure 5.7b, Figure 5.7c) in the *strong convective mixing case* (dashed line), one can see that resaturation begins practically at the same time across all flow-focusing cases–around year 700. This also occurs in the *moderate* and *no convective* mixing cases, with resaturation times all occurring at years 340 and 400, respectively. These results show that the starting time of resaturation of the matrix is affected little by variation in the rate of percolation, consistent with findings in the temperature response (which also is little affected by the percolation). In fact, as saturation in the rock is primarily dependent on the rock temperature, we actually are observing the same times for matrix resaturation because the temperatures in the rock remain the same across the three flow focusing cases. So then, for any given convective mixing case, the time of matrix resaturation is more or less the same.

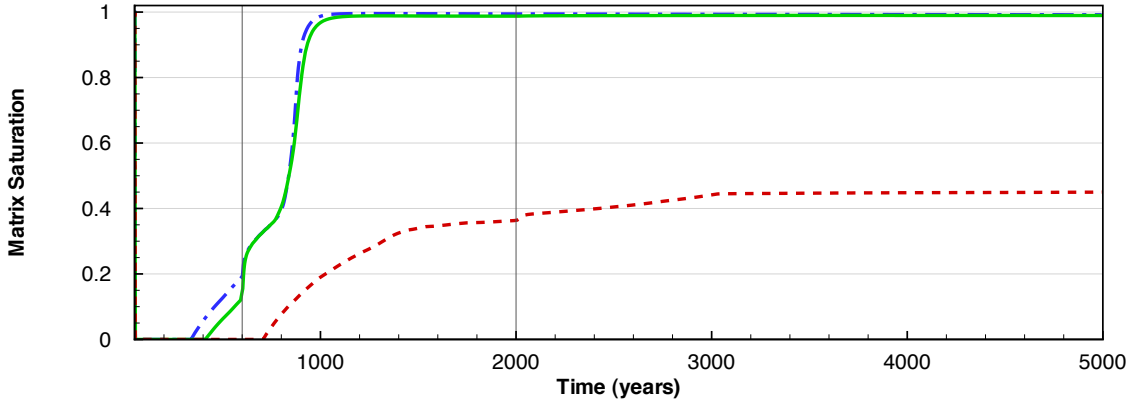

(a) No flow focusing case.

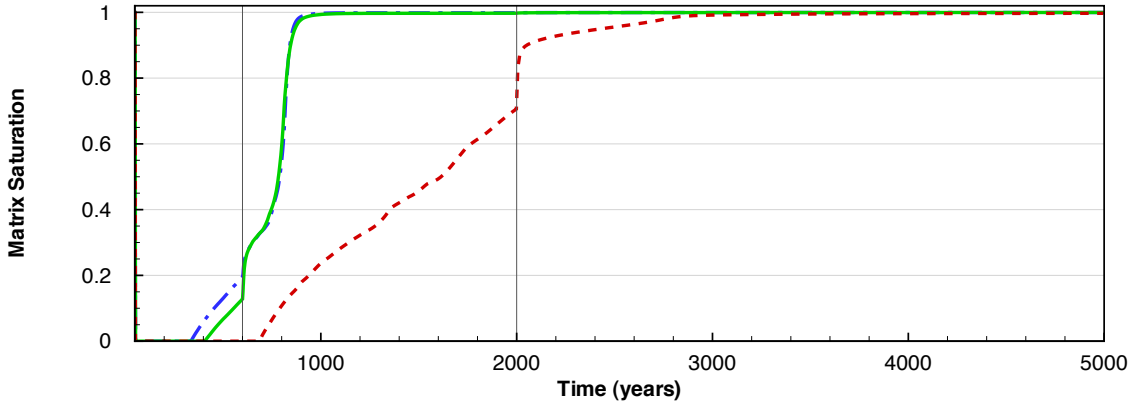

(b) Flow focusing 10 case.

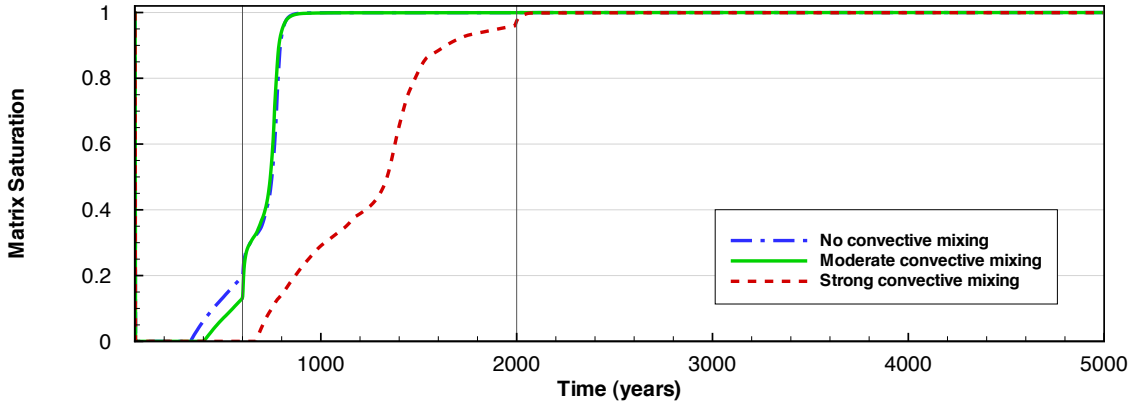

(c) Flow focusing 20 case.

Figure 5.7: Matrix saturation in a seepage prone element at the drift wall for (a) no flow focusing (mean infiltration), (b) flow focusing 10, and (c) flow focusing 20 cases.

Tracing the evolution of saturation in the *no and moderate convective mixing cases* (Figure 5.7, dash-dotted and solid lines), we see a jump occurring at year 600, corresponding to the assumed future transition from a present-day to a wetter monsoon climate. Eventually, both convective mixing cases converge to a threshold saturation around 0.99. Also, the rate at which saturation occurs is impacted by the percolation rate, evident by observing the slope of saturation in the *no convective mixing* and *moderate convective mixing cases* (dash-dotted and solid lines) just after year 600, all of which have a notable increase with increasing percolation. For the strong convective mixing case (dashed line), we see greater variation in the response across the flow-focusing cases, with much lower saturation overall. Strong convective mixing greatly reduces moisture in the rock for all flow-focusing cases.

5.4.3 Fracture Saturation

More important to predicting thermal seepage is the fracture saturation in the seepage element. We show in Figure 5.8 the fracture saturations for each flow focusing case and each convective mixing case. The fractures are completely dry in all cases for the first 800 years as the rock temperature during this time remains above boiling preventing liquid water from existing in the fracture voids. As the decay heat diminishes and the matrix has partially saturated, rewetting occurs soon thereafter in the *no convection* (dash-dotted line) and *moderate convective mixing* (solid line) cases, around year 900 for both. Discussed above, the beginning of the fracture resaturation corresponds to a certain saturation being reached in the matrix when the capillary pressure is reduced significantly to allow water to exist in the fractures. Water present in the fractures provides another source for matrix saturation (i.e., water imbibes into the matrix due to capillary forces), as compared to the case earlier in time, where only the matrix domain was transporting water. As such, these times correspond to an increase in matrix saturationFigure 5.7, apparent with the increase in the slope of saturation a few years after the change to a wetter climate and higher infiltration rates at year 600.

As we would expect, the increase in the infiltration rate at year 2000–due to another assumed climate transition to a glacial climate–promotes a jump in the fracture saturations, which slowly increase with time after as a result of declining temperature. For the *no flow focusing case* combined with *strong convective mixing* (dashed line in Figure 5.8a), no water is observed near the drift wall until well after 3000 years, showing the evaporative potential of the strong natural convection processes. A similar behavior is observed for the *flow focusing 10 case*, depicted in Figure 5.8b, however now with much larger fracture saturations and earlier rewetting of the fractured rock. Whereas fracture saturations in the no flow focusing case are approaching 0.2, the fracture saturations are now close to 0.5. Also, we see the rewetting of the seepage element in the *strong convective mixing case* much earlier, around year 1200.

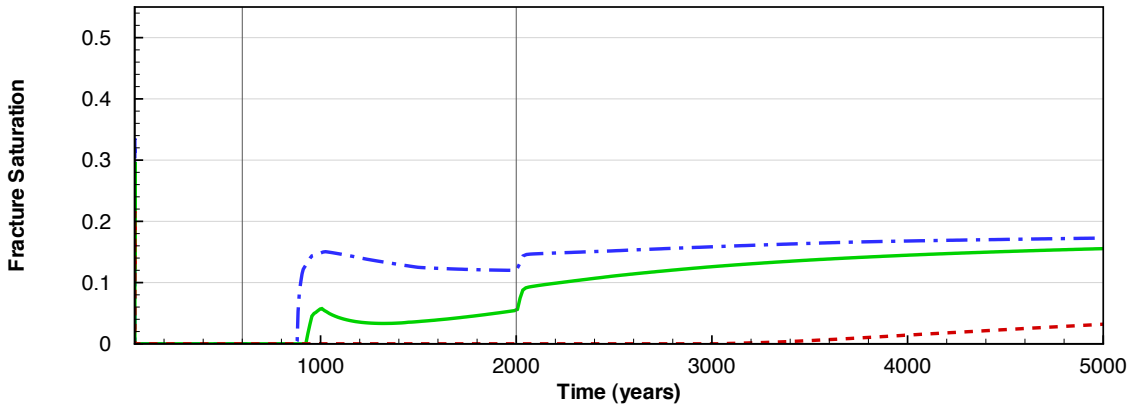

(a) No flow focusing case.

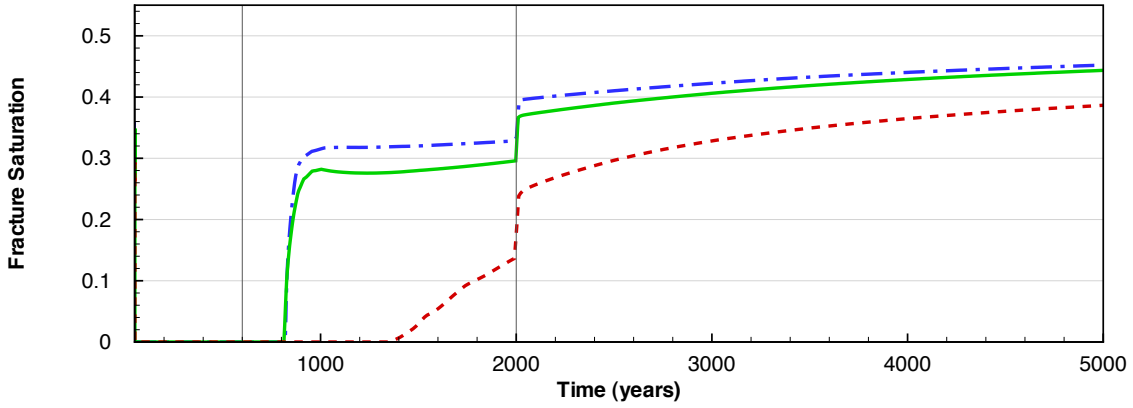

(b) Flow focusing 10 case.

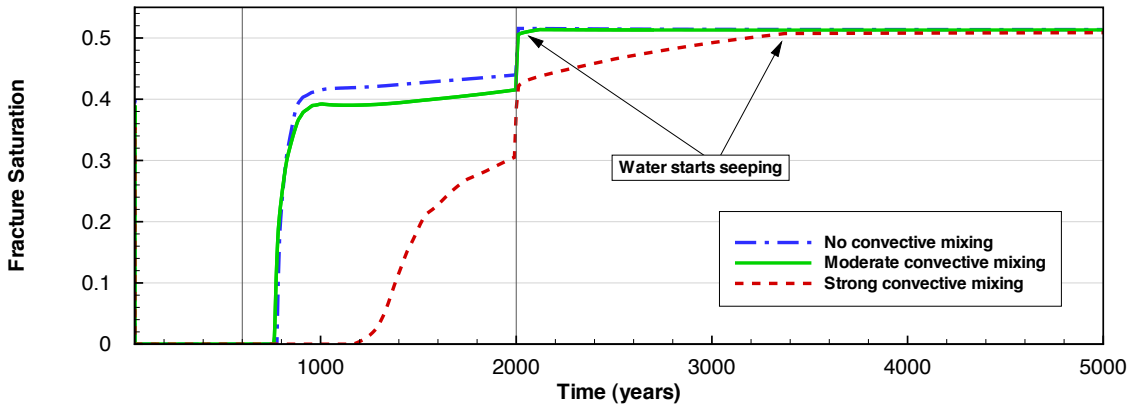

(c) Flow focusing 20 case.

Figure 5.8: Fracture saturation in a seepage prone element at the drift wall for (a) *no flow focusing* (b) *flow focusing 10*, and (c) *flow focusing 20* cases. Vertical grey lines indicate stepwise changes in percolation flux caused by expected future climate changes at 600 years and 2000 years after emplacement.

The *flow focusing 20 case* (Figure 5.8c) shows an even larger response in fracture saturation for all convective mixing cases due to the increase of the percolation rate. In this case we now observe the saturation reaching a threshold, when the slope becomes zero[6]–around 0.5 for all cases. For both the *no convective mixing* and *moderate convective mixing* cases, this occurs around year 2000 due to the transition from monsoon to glacial climates and the subsequent increase in the infiltration rate boundary condition by a factor of about 1.5. The *strong convective mixing* case reaches critical saturation much later, around year 3300, meaning evaporation at this case effectively delays the element from reaching a critical saturation until the thermodynamic conditions of the in-drift become such that it can happen. It is at these critical values where we can expect seepage to occur.

5.4.4 Seepage Percentage

We check our predictions by observing the seepage percentage, both ambient and thermal, from a seepage-prone element. The seepage percentage is defined as the ratio of the liquid flux that seeps into the drift to the total liquid flux percolating with constant infiltration rate through a cross-sectional area corresponding to the footprint of the drift. The calculation is done only for the vertical layer of locally focused percolation flux. As expected from the fracture saturation plots, for the time periods plotted no seepage was observed in the *flow focusing 10* and *no flow focusing* cases, as the threshold saturation was never reached. Therefore, we show in Figure 5.9 seepage for the *flow focusing 20* case only, comparing the seepage percentage for the thermally perturbed simulation with an ambient-seepage reference case where no heat is considered.

In Figure 5.9, no ambient seepage occurs during the first 600 years associated with the modern climate scenario (which has an assumed percolation rate of 120 mm/yr in the layer of locally focused flux for this *flow focusing 20* case, see Table 5.3). However, during the monsoon and glacial climate scenarios, the capillary barrier is overcome (no contribution from evaporation in the ambient cases) and seepage percentages of 6% (320 mm/yr) and 16% (500 mm/yr) are achieved (a seepage percentage of 16% means that 16% of the percolation water arriving at the drift wall is seeping into the drift). Although ambient seepage does occur in the monsoon climate, thermal seepage is not present until the glacial climate infiltration rate is reached. As expected, the start of seepage corresponds to the fracture saturations reaching their threshold values. At the year 2000, we see that the result for the *no convective mixing* case (dashed-dotted

[6]While from observation of Figure 5.8c the slope of the fracture saturation seems to be zero, it is, in fact, slightly positive as decreasing temperatures allows larger saturations to exist in the fractures. The flow of an inbibing liquid into a void due to capillary pressures is halted once an equilibrium is reached with an opposing pressure. This opposing force is normally found from the gas pressure trapped in the void. At reduced temperature the gas pressure decreases, reducing its volume and as such allowing an increase in saturation, if ever so slightly.

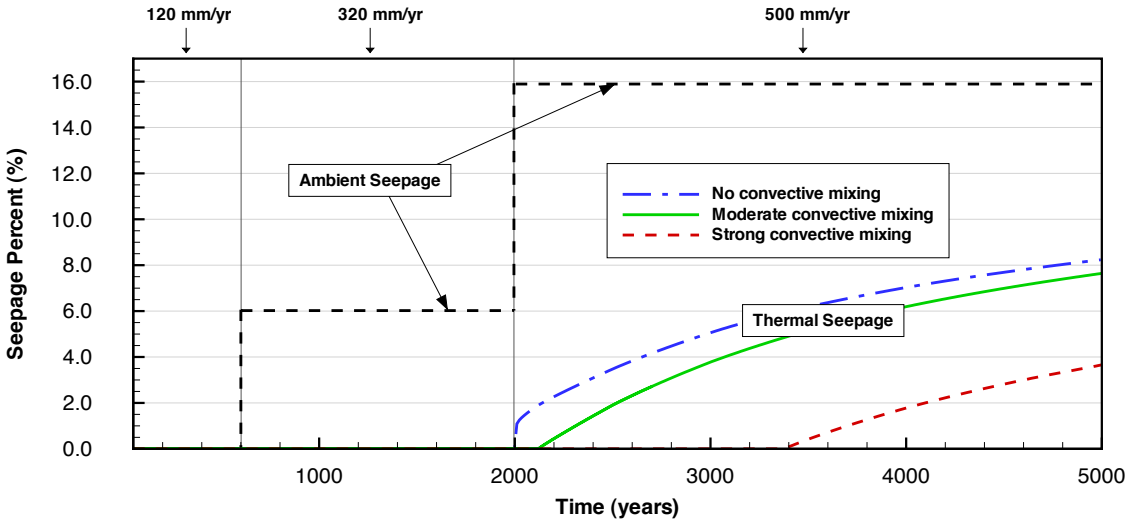

Figure 5.9: Seepage percentage for the *flow focusing 20* case for both ambient (dashed lines) and thermal (solid lines) seepage. (No seepage is observed in either the *flow focusing 10* or the *no flow focusing* cases). Vertical grey lines indicate stepwise changes in percolation flux caused by expected future climate changes at 600 years and 2000 years after emplacement.

line) jumps immediately to a 2% seepage percentage, and increases from this time on, eventually reaching about 8% of the percolation rate.

Similarly, seepage starts around 2100 years after waste emplacement in the *moderate convective mixing* case (solid line), but always remains slightly below the seepage percent in the *no convective mixing* case. This is because even moderate convective mixing allows for some removal of moisture from the drift walls and thereby reduces the rate of seepage. In the *strong convective mixing* case (dashed line), seepage is substantially decreased and starts later, around 3200 years after emplacement—well past the thermal pulse with temperatures now around 60°C. At year 5000, with a seepage percentage of only 3.5%, the *strong convective mixing* case has significantly lower values than the 7% and 8% observed in the *moderate* and *no convective mixing* cases. As suggested earlier, these results show that strong convective mixing due to natural convection can reduce seepage significantly for the time period that thermal perturbation is present.

5.4.5 Vapor Flow

Besides diversion around the drift wall via capillarity, how else is percolation water removed from the wall? Vaporization and evaporation, especially after the temperature

drops below the boiling point, allow for liquid water to be mobilized by phase change to a gas form, which is then transported away in the open drift. To understand how this effects seepage, we can observe vapor transport across the drift wall boundary, specifically, the diffusive and convective vapor fluxes from the drift wall in the seepage layer into the drift. Convective fluxes are driven via pressure gradients, generated by the increased pressure from the boiling of liquid water in the rock. Diffusive fluxes are driven by concentration gradients of water vapor between the near-drift rock and the in-drift environment.

5.4.5.1 Diffusive Vapor Flow

Figure 5.10 shows the diffusive vapor flow from the seepage-prone rock element into the drift in both the fracture (green dashed lines) and matrix (red dashed lines) domains for the strong convective mixing case, across every flow focusing scenario. Figure 5.10a shows the *no flow focusing* case. It is observed that the diffusive vapor flow during the first 3000 years occurs only from the matrix domain. Near year 3000, rewetting of the fracture element occurs and diffusive vapor flow from the fractures to the in-drift begins, gradually increasing to dominate the total diffusive vapor flow (figure 5.10a - green colored line). As the fracture domain rewets, the decay heat still promotes vaporization of water in the rock and increases the concentration of vapor versus the tunnel air space. This vapor produced is driven via diffusion through the more permeable fracture domain into the in-drift.

The *flow focusing 10* case shows a substantial increase in the diffusive vapor flow due to the increased infiltration source. Again, we observe that the diffusive vapor flow occurs only through the matrix domain until rewetting occurs, around 1200 years. Here, as the fracture domain within the element has rewetted, diffusion through the fracture increases quickly to be the main contribution to diffusive flow. The flow rate continues to increase–likely converging to an upper bound–until the transition to glacial climate occurs. This transition (and subsequent increase in the infiltration source) causes a jump in the diffusive vapor flow at year 2000, with a gradual decline after as diminishing decay heat reduces vapor production, decreasing the vapor concentration gradient between the rock and the in-drift air spaces, and eventually converging to a steady value at ambient temperatures.

Finally, we can plot the *flow focusing 20* case (Figure 5.10.c), and now observe an even larger amount of diffusive vapor flow due to the increase in the infiltration source and subsequent production of vaporized water. Initially, as in the *flow focusing 10* case, we see diffusive flow occurring through the desaturated matrix, indicating that, like in the *flow focusing 10* case, the vapor being produced outside of the drift wall region is being driven by diffusion through the matrix domain of the superheated rock and into the open cavity. When the fractures of the rock element finally rewet, around year 1100, we see a shift in diffusive flows from the matrix domain to the fractured

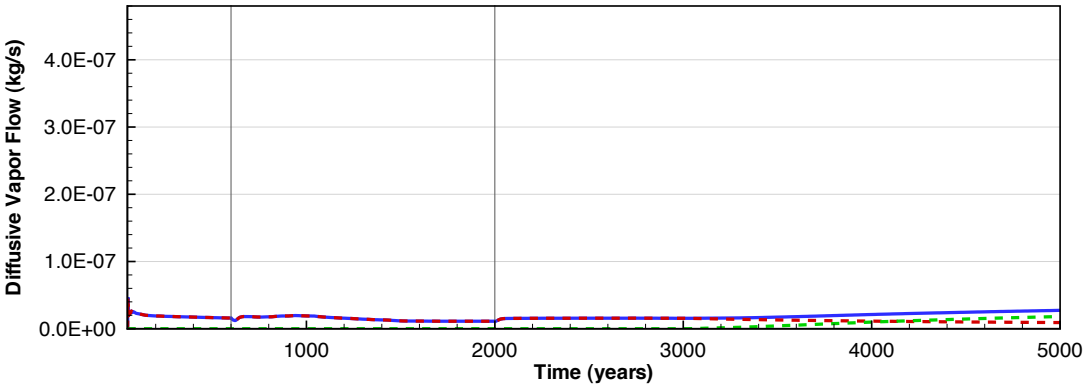

(a) No flow focusing case.

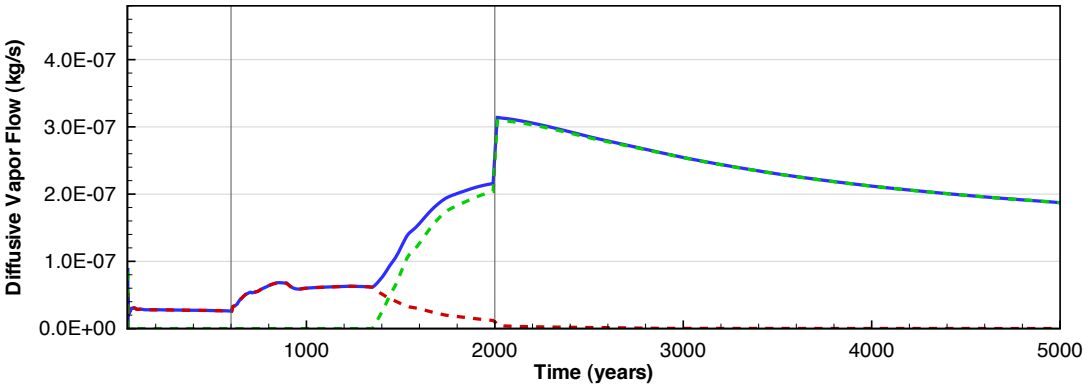

(b) Flow focusing 10 case.

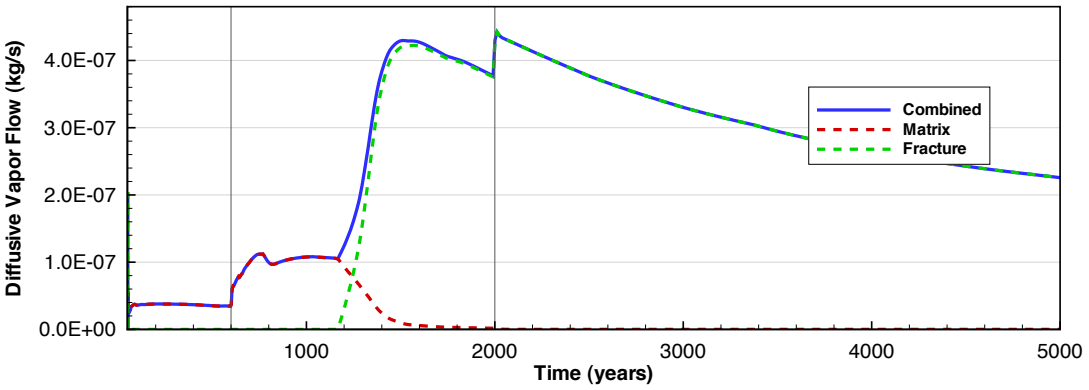

(c) Flow focusing 20 case.

Figure 5.10: Diffusive vapor flow in the *strong convective mixing case* from a seepage prone element at the drift wall from both the matrix domain (red dashed line) and fracture domain (green dashed line) for (a) no flow focusing (mean infiltration) (b) flow focusing 10, and (c) flow focusing 20 cases. Vertical grey lines indicate stepwise changes in percolation flux caused by expected future climate changes at 600 years and 2000 years after emplacement.

domain (red line declining, and green line increasing) as vapor is now being produced and transported in the fractures.

Unique to this *flow focusing 20* case, a peak is observed in the diffusive flow after transport in the fractures begins, around year 1500 during the monsoon climate. Unlike the previous cases, the increased percolation in the *flow focusing 20* case reaches a limit in the diffusive vapor transport. Declining temperatures in the rock, from the diminished heat output of the waste canisters, are able to vaporize only a limited amount of water arriving at the drift wall in the seepage layer. This peak shows the limit being reached, and although it does not imply that seepage is occurring, it does indicate the limited potential for vaporization of percolation water in the rock. Indeed, after the transition to glacial climate, the diffusion flow jumps to an even higher value, and finally the percolation water seeps into the cavity (Figure 5.9).

5.4.5.2 Convective Vapor Flow

Convective fluxes are driven by pressure gradients between the rock and the in-drift environment. As vapor is produced by boiling or vaporization, the large density change associated with the transition from liquid to gas increases the pressure locally where vapor production is occurring creating the pressure potential for transport. Figure 5.11 shows the convective vapor flow from the seepage-prone element to the in-drift for the strong convective mixing case (as was plotted in Figure 5.10). Similarly to what we observed in the previous plot showing the diffusive vapor flow, the fluxes are small in the *no flow focusing* case (Figure 5.11a) and much larger in the *flow focusing 10* and *flow focusing 20* cases, due to the increased vapor production from increased percolation. Unlike diffusive flows, the convective flow takes place almost entirely though the highly permeable fracture domain (green lines Figure 5.11), where the pressure driven vapor can transport more easily than through the matrix.

Initially during the modern climate scenario, in all the flow-focusing cases, convective transport exists only in the fracture domain while the diffusive vapor transport exists in the matrix domain. Following the evolution of both the *flow focusing 10*, and *flow focusing 20* cases (Figures 5.11b and 5.11c), convective transport decreases slightly as a result of declining temperature in the rock until the transition to monsoon climate, where a rapid increase occurs due to vaporization of the additional percolation water. This increase continues until resaturation of the fracture occurs during the monsoon climate for both flow-focusing cases, and we observe a sharp drop in the convective flow. As the fractures now contain liquid water, their ability to transport pressure driven vapor is decreased, and the vapor is now primarily removed by diffusion (as was previously discussed).

The contribution to moisture removal from the rock due to convective vapor transport is very small at later times as the primary mechanism for vapor transport has shifted from pressure driven flow to diffusion driven flow. Both boiling and vaporization

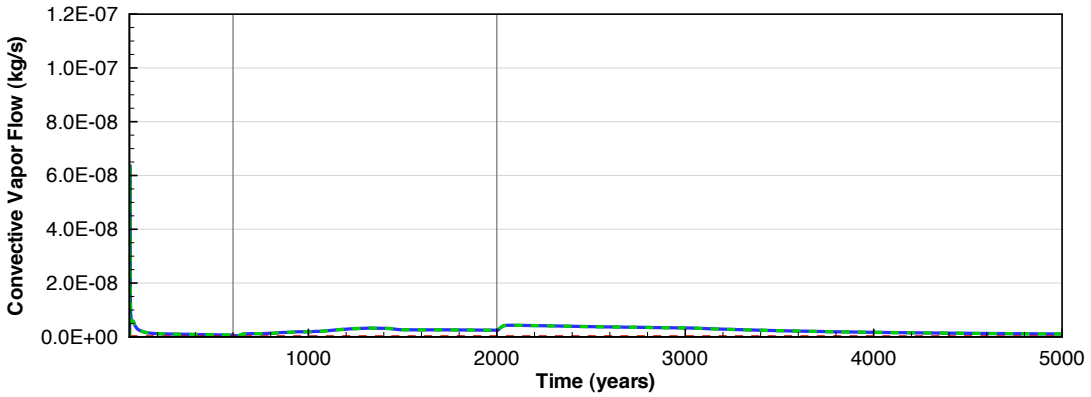

(a) No flow focusing case.

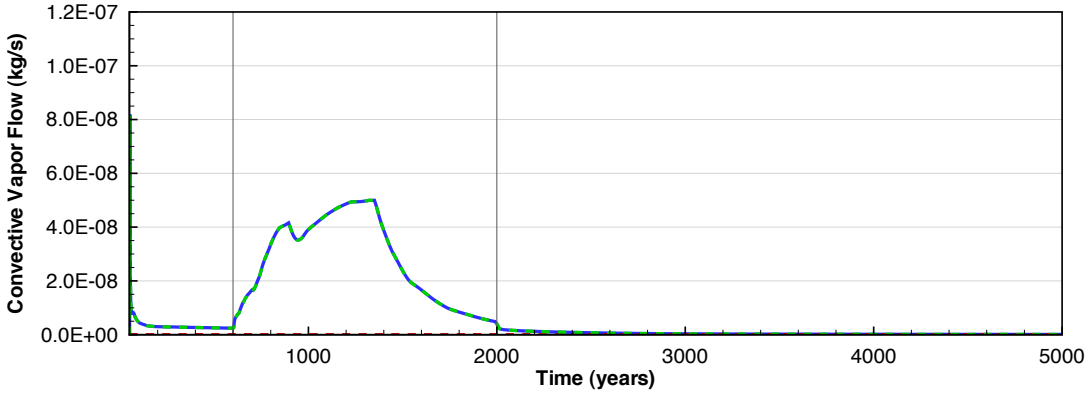

(b) Flow focusing 10 case.

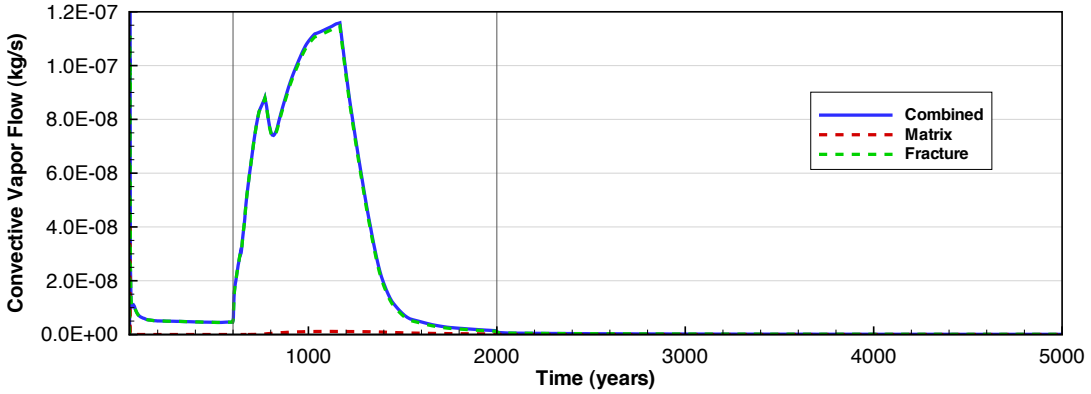

(c) Flow focusing 20 case.

Figure 5.11: Convective vapor flow in the *strong convective mixing case* from a seepage prone element at the drift wall from both the matrix domain (red dashed line) and fracture domain (green dashed line) for (a) *no flow focusing* (b) *flow focusing 10*, and (c) f*low focusing 20* cases.

production rates have decreased substantially, allowing very small pressure differences from existing in the fractured rock and the open cavity. In the *flow focusing 20* case, convective vapor transport has very little contribution to the long-term delay of seepage, when compared with the diffusive vapor transport. This suggests that, in the case of *strong convective mixing*, diffusion driven transport is the primary mechanism for the drying of the rock, and as such, responsible for delaying the start of seepage. This is due to the strong difference in vapor concentrations between the surrounding rock and the in-drift in this case. Although not plotted for sake of brevity, the differences between convective and diffusive vapor transport for the *moderate* and *no convective mixing* cases are much smaller than in the case with strong convective mixing, as diffusive transport is not nearly as effective.

5.5 Conclusions

We conducted a numerical study to explore the impact that natural convection processes have on the reduction of drift seepage at the Yucca Mountain repository. We developed a new TOUGH2 seepage model based off of existing seepage models and employed results from a previous natural convection model. This natural convection model, coupled to existing modeling approaches for predicting heat and mass transport in the rock mass, approximates in-drift convection as a binary diffusion process.

We performed quasi three-dimensional simulations runs for a detailed geometrical representation of an emplacement drift cross-section plus surrounding fractured rock located in one of the southern panels of the repository. Three simulation cases represent different degrees of convective mixing in drifts as determined from CFD studies reported in the literature along with three different flow focusing cases to capture the affect of preferential flow caused by subsurface heterogeneity. Our simulation results demonstrate the importance of in-drift natural convection on seepage reduction. Strong convective mixing in natural convection:

(i) causes considerable delay in the rewetting of the fractured rock, and also the seepage rates, in all flow focusing cases,

(ii) reduces the maximum fracture saturations achieved at the drift wall,

(iii) considerably increases both the diffusive and convective vapor flow from the rock domain into the open air drift tunnel, and

(iv) significantly reduces the amount of seepage into the drift when compared to the other convective mixing cases.

Natural convection effects in the open drifts thus should improve the performance of the repository, since smaller relative humidity values, with reduced local seepage, form

a more desirable waste package environment. As the results of our study have demonstrated the importance of natural convection in assessing the future TH conditions in Yucca Mountain drifts, we recommend conducting large-scale field experiments in heated open tunnel sections to:

(i) validate several model assumptions and

(ii) to better constrain the uncertain magnitude of natural convection occurring in such tunnels (i.e., to determine whether natural convection effects in heated drifts at Yucca Mountain would be better described by the moderate or by the strong convective mixing modeling scenarios).

Chapter 6

Conclusions

6.1 Model Validation and Limitations

Unless the experiments at the Large Hadron Collider (LHC) are not successful in discovering the Higgs boson, the Standard Model of particle physics serves as one of science's greatest examples of a validated model. Since its inception in the 1960's, it has continued to be upheld in its accurate representation of reality with the successive discoveries of the sub-atomic particles that it has predicted to exist. The search for the Higgs Boson in the LHC is a continued attempt in efforts of *validation* of the Standard Model, to claim with certainty that its descriptions of—in this instance, fundamental particle interactions—directly represent that observed in nature.

Model validation is an essential part of the model development process, and involves the testing of the model to ensure its usefulness in that it:

(i) addresses the correct problem and

(ii) provides accurate information about the system in question.

Validation exercises demands modelers take a step back away from the details of the modeling activity and from an introspective position, ask, in a broadest sense, does the model serve well its purpose?

6.1.1 A view from a little bit away

To question if a model well-serves its purpose, it is necessary to first ask the transposed form: what purpose does a model serve? A model is some construct that allows the representation of processes and systems in the *real-world*, often to answer questions

that we might have about it. In the realm of the physical sciences, modeling can refer to various activities, all attempting to capture or explain phenomena ranging from a basic physical process (e.g., diffusion, convection) to an entire system (e.g., the Unsaturated Zone, Yucca Mountain). Models allow for the understanding of processes that occur over scales, such as time, length, temperature or other fundamental parameters, where direct measurement by observation is unattainable. As such, they can often:

(i) provide insight to how such processes can occur where testing is impossible,

(ii) help to overcome limitations of human intuition as to the behaviors and response of complex systems with dependent, coupled processes, and,

(iii) allow numerous testings to be performed with varying system constraints applied (boundary/initial conditions).

Based on observation of nature, analytical models try and explain physical processes in the form of a mathematical relationship and can, with multiple parameter dependancies, quickly become complex. Often, direct analytical solutions are not possible with current methods and must therefore be approximated (and approximated well) using numerical models, which commonly discretize both the equation and the calculation into finite parts to later be summed to form a solution. These numerical models can be combined in the form of a computer model, which employs the use of a computer to perform calculations on massive sets of these numerical approximations. Such computational potential opens the possibility for creating combinations of many models that operate in parallel, nested, and/or recursive relationships. Operating in unison, the complex set of relationships created by such model combinations can begin to define a *system*, and, as such, can estimate this *system's* response to specific changes in conditions over time.

6.1.2 What is Validation?

Due to the fundamental nature of the universe, processes in the real-world are inherently complex and hard to define. Theoretical models that attempt to establish such definitions are often compared to physical models or laboratory experiments, ensuring consistency between predicted and observed results. While customarily scaled to dimensions and operating conditions tenable given constraints of space, time, and cost, these models operate in reality and, in doing so, yield results empowered with the incorporation of *real-world* effects. The comparison with results that include such effects can often show limitations of the theoretical models, providing an important feedback that is critical in ensuring model validity. Similarly, these comparisons can show the robustness of a model, further ensuring its validity of, or ability to accurately represent, the system and constraints in question. Model validation refers to the array of exercises and procedures that can be performed to make such comparisons[77].

It is incorrect to conceptualize successful validation as achieving some rank or level for the model—the final result is not a *validated* model, but is rather a model that has passed validation tests[78]. This shift in perception of the concept is subtle, however, exceedingly important for the modeler undertaking the question-asking activity. Instead, models should be conceptualized as being *valid* for answering a specific range of questions about a specific range of properties or behaviors for a system operating within a specific range of parameters. As such, validation must be considered a continual effort, repeatedly undertaken to expand the model capabilities and further refine the level of processes approximation with each additional question that would necessitate such.

6.1.3 TH Seepage Model Validation

The Thermal-Hydrological models of the Yucca Mountain repository have been in development for over thirty years since the time of this writing[17, 21–23, 33, 37, 44, 46, 74, 79]. Validation exercises of these models have been an ongoing parallel activity for the Yucca Mountain site characterization in order to ensure that the models can answer the question posed as to the site's performance as a long term radioactive waste repository. Indeed, being that these numerical TH models represent a physical system, validation exercises were performed against experiments conducted onsite at Yucca Mountain.

Of the many experiments performed, the Drift-Scale Test (DST) was particularly suitable for this function, as it covered a range of operating conditions that would be experienced by the repository with nuclear waste[80]. In short, the DST was an in-situ test, performed over the course of eight years during which time an exploratory tunnel in the repository horizon was heated to temperatures to be expected during repository operation, inducing the complex coupled phenomena that a numerical TH model would try and capture. Four years of heating—initiating the vaporization, vapor transport, condensation and drainage of the existing pore-water in the fractured rock—was then followed by four years of cooling to ambient conditions. Sensors, measuring a range of parameters that define behaviors in fractured porous media, captured the response of the experiment.

Developed in tandem, a numerical model (referred to as the DST-TH model) of the in-situ test was created to ensure that TH models—describing heat and fluid flow in the porous media—were able to predict important phenomenon in the DST (e.g., saturations, temperatures, phase-changes, and fluid flow patters)[29, 46]. This is significant, as the DST and an actual emplacement drift at the repository are of the same scale, located in the same geologic conditions, and operate over the same temperature range. Thus, if validation of the DST-TH model could be performed, future developed TH seepage models—whose underlying structure employs the very same heat and fluid flow models as those in the DST-TH model—would be considered validated

as well. Indeed, results from this study showed not only a very strong direct agreement between predicted and measured data, but also an underlying comprehension of the fundamental processes from where they were produced[46].

6.1.4 Validation of *Nat-co* and *Seepage* models

The drift *Nat-Co* and *Seepage* presented in this dissertation were developed to answer the question, how would natural convection impact thermal-hydrological conditions and processes in the unsaturated fractured rock, including drift seepage? It was a question that had yet to be asked or answered, and as such, presented a unique opportunity to add to the collective knowledge of the expected behavior of the Yucca Mountain repository. To answer this question, the simulation model harnessed the combination of two model subdomains, that of the fractured rock mass and that of the open space in-drift. The fractured rock sub-model of the Drift *Nat-Co* and *Seepage* models are entirely based on the previously-validated TH models, and being that they represent an almost equal system and operation conditions, can therefore also be assumed to be valid in their predictions for the scenarios presented.

The models for the in-drift environment, however, were taken from methodologies employed in previous studies, and rely specifically on the approximation of the in-drift convection with the enhanced dispersion coefficient. The magnitude of this parameter is, by far, the most important to the overall results of these studies—having a significant impact on the results of drift seepage and the drying of the fractured rock. While it would have been better to have confirmed this value from laboratory experiments (as discussed ahead), the CFD values allow both the *nat-co* and *seepage* models to provide a qualitative understanding of the impact the natural convective processes have on the surrounding fractured rock, answering the original question posed for initiation of the investigation. With this, we can conclude that the model presented in this this thesis is *valid* for the system and scenario in question because:

(i) The model confirmed an expected and unique responses.

(ii) These simulation responses were a result of the implementation of well-thought models (e.g, the in-drift subdomain model, radiation model)

(iii) These models were developed on a solid understanding of fundamental principles, and were expansions of already-existing and well-validated models.

6.2 Research Accomplishments

The research effort was successful in that it answered the question: what role does natural convection have on the in-drift environment and how does that in turn, affect the near-field fractured rock? In the process to answer this question, much was learned about the system, including insight into relevant processes, and established fundamental knowledge of how similar systems would behave—hopefully to be expanded upon in further research endeavors.

6.2.1 Drift Radiation

Chapter 3 presented a model, based on the Stefan-Blotzman approximation, for considering thermal radiation transport within the drift environment. This allowed for radiative connections to be established between the elements representing the emitting and receiving surfaces of the in in-drift. Also developed was a unique preprocessing code calculating the view factors to consider the effects of the geometrical orientation and distance between surfaces, capturing the role of three-dimensional radiation transfer. While existing itself as only a component of the overall in-drift heat transfer in both the *nat-co* and *seepage* models, the model was used to perform simple calculations to show the role thermal radiation has on the redistribution of heat within the drift environment.

6.2.2 Drift Natural Convection Model

Chapter 4 presented a model considering the effect of natural convection in the in-drift domain, approximating its contribution to the axial transport of both heat and energy as a binary diffusion process, with effective dispersion coefficient given from previous CFD studies. Considering two cases for the magnitude of the convective mixing process, natural convection was shown for both to be an effective mechanism for the: (i) transport of vapor from the heated drift center to the cool drift end, (ii) the drying of the formation rock maintaining reduced saturations. Detailed profiles of saturation in both the matrix and the fracture were generated, allowing visualization of changes in the fracture rock with time and the formation of a condensation zone in the drift turnout, a result of an effective transport of vapor from the heated drift center to the cooler drift end. Finally, the average thermodynamic conditions of the in-drift environment were predicted with time, allowing for use in the *Drift seepage model*, presented in Chapter 5.

6.2.3 Drift Seepage Model

The development of a quasi-three-dimension model for understanding the impact of natural convection on drift seepage was discussed in Chapter 5. The results of the thermodynamic conditions of the in-drift environment from the simulations performed with the *nat-co* model were used as a time-dependent boundary condition, reducing the need to model the entire drift-length. With these expected in-drift conditions maintaining a drier in-drift enviroment, the impact of a flow-focused event causing seepage was tested in three cases of increased rates of percolation. The reduced RH environment caused by natural convection was shown to: (i) delay the rewetting of the fractures, (ii) significantly reduce fractures saturations at the drift wall, and (iii) offset the release and reduce the magnitude of seepage during a flow focus event.

6.2.4 Model Result contribution

The results of these models have contributed to the greater knowledge of the behavior of the Yucca Mountain Repository by, specifically, bounding the expected effects that heat-induced natural convection in the in-drift has on the thermohydrological conditions in the surrounding fractured rock. Specifically, they help understand the mechanisms by which natural convection:

(i) reduces the moisture in the local environment of the heated waste canisters and,

(ii) reduces the likelihood of a drift seepage due to a flow focusing event occuring.

In regards to the long-term integrity of the waste canisters guarding the radioactive waste, both the above effects are beneficial as they reduce the probability of any water-induced corrosion from occurring. This knowledge is critical in the effort of assessment of the performance of the repository as a long-term solution for the disposal of high-level radioactive waste, a necessity of a society that has pursued, and continues to pursue, the benefits of nuclear technologies.

6.3 Future Efforts

While significant amount of knowledge was amassed during this research endeavor, there still exist much opportunity to answer remaining questions. Mentioned earlier in this chapter, the model sensitivity to the dispersion parameter, and the wide range of the values provided by the CFD analysis, warrant further investigations to be conducted to better bound the value of this parameter. The geometric configuration

for the in-drift environment is distinctly unique, with no previous analysis of the flow scenarios to be expected in such a system having been performed.

Scaled physical models (as in laboratory experiments) can be designed to capture the range of system operating conditions, fluid properties, heating distribution and geometric configuration that are expected. Properly calibrated using dimensional analysis, a scaled laboratory model, such as that provided by the former ATLAS facility[81], would provide a perfect opportunity to better define this parameter, especially by including the effects of an binary system. Still, university-level experimentation could also be undertaken, employing the use of inexpensive prefabricated construction materials for a mock drift (e.g., concrete forming sonotubes would be a simple construct for the drift tunnel) and the plethora of sensor and data capturing instrumentation (e.g., artificial smoke concentration measurements using laser attenuation devices or capacitance meter) for measuring species transport.

6.3.1 Coupled CFD/Porous Media Models

In addition to the lab scaled experiment, the complex coupling between CFD modeling of in-drift and porous media modeling of fractured rock, would also be a valuable tool for better understanding the coupled processes of in-drift natural convection and the impact on the surrounding fractured rock. This would involve a serious discussion regarding how to handle the large differences in the spatial and temporal differences between the two models, especially at the drift wall boundary, where the two domains interact[59]. A difficult endeavor, it would require tremendous computing power, and an intelligent iteration scheme to maintain equilibrium of the thermodynamic conditions between the open drift CFD model and the fractured rock porous media model.

Appendix A

Boundary Layer Correlations

The use of boundary layer correlations plays an important role in capturing the effects of convective heat and mass transfer in the models described in this dissertation. So then, here further described are the development of such boundary layer correlations, along with a general discussion of how they were implemented into TOUGH2.

A.1 Boundary Layers

In a thin region next to the surface of the heated object, the effects of fluid viscosity play an important role on the heat transfer. In the case of a vertical heated plate, buoyancy forces drive an upward velocity that is shaped by the shear forces exerted on the fluid from the no-slip condition produced by the plate. The region where the velocity changes from zero (against the wall) to some maximum and back down to the bulk air velocity is called the velocity boundary layer, as shown in Figure A.1. The temperature drop from the surface to the ambient air occurs over a region we define as the thermal boundary layer. The temperature and the velocity boundary layers are a coupled phenomena and change with position along the heated surface. It is within these boundary layers that the convection heat and mass transfer occurs, as such, they define how energy and mass is transported from the hot surface to the the inviscid (bulk) gas region. Thus, it is important to be able to characterize the boundary layer in order to predict the convective transport processes accurately.

For the most basic of boundary-layer flows, solutions exist using the integral method, however, different types of flow regimes also have an impact on the boundary layer

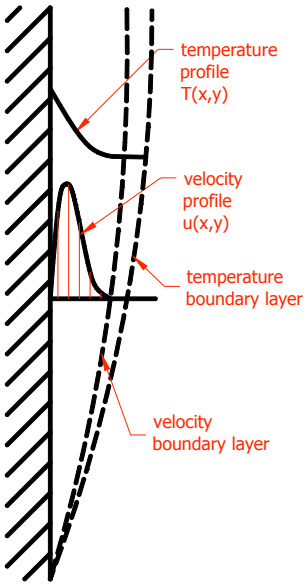

Figure A.1: Boundary layer across a vertical plate.

heat transport. At a critical value for the Rayleigh number[1] the flow transitions from laminar to turbulent—for which no exact solution exists. For anything but the simplest geometry and flow confined to laminar regimes, these boundary layer profiles are extremely complex and solving them is not practical as a method to understand the convective transport. CFD codes can also be used to predict the boundary layer effect by solving the Navier-Stokes equations using a finite-element method on a finely meshed grid near a surface in question—thus simulating the direct effects of boundary layer formation such as done in the convection model developed by Reed et al. [55, 58]. Effective for CFD simulations, our need to include the effects and interaction of both domains does not allow us to calculate the in-drift environment using such a model. The coupling between porous media flow and computational fluid dynamics would be a massively complex and computationally-intensive effort due to the significant differences in the spatial and temporal discretization demanded by both domains. Thus, we are bound to resolve the convective heat and mass transfer problem with a different approach.

[1] A dimensionless parameter quantifying flow regimes for buoyancy-driven transport, the Rayleigh number is a product of the Grashof number (comparing the relationship between buoyant and viscous forces within a fluid) and the Prandtl number (comparing the relationship between thermal and momentum diffusivity) and is generally defined as, $Ra_x = Gr_x Pr = \frac{g\beta}{\nu\alpha}\, x^3\, (T_s - T_\infty)$.

A.2 Nusselt Number

In order to quantify how effectively heat transfer is enhanced due to the fluid motion from convective flow, a ratio is commonly employed that compares the increased effect of heat transfer via convection to the heat transfer via conduction (assuming the non-physical scenario of the surrounding bulk fluid being static). This dimensionless parameter is called the Nusselt number, and can be described as

$$Nu = \frac{q_{\text{conv}}}{q_{\text{cond}}} \tag{A.1}$$

Although it is traditionally solved using dimensional analysis, it can be solved in a more conceptual approach here (using a slightly modified methodology as presented in [49]). From Fourier's Law of Heat Conduction, the heat flux q'' is given by

$$q'' = \frac{q}{A} = k\,\frac{dT}{dx} \quad \left[\frac{W}{m^2}\right] \tag{A.2}$$

where k is the thermal conductivity of the material with units of $\left[\frac{\text{W}}{\text{m K}}\right]$.

Consider a slab of material with thickness L, thermal conductivity k and temperatures T_1 and T_2 at the inner and outer surfaces, respectively. Using Fourier's Law of Heat Conduction and rearranging and integrating across thickness of the slab yields,

$$q'' = \frac{q}{A}\int_0^L dx = -k\int_{T_1}^{T_2} dT \Longrightarrow \underline{q_{\text{cond}} = \frac{kA}{L}\,(T_1 - T_2)} \tag{A.3}$$

which is the well-know equation for one-dimensional heat conduction.

Additionally, Newton's Law of Cooling provides a means to solve for total heat transfer (via conduction and convection). This law is given by

$$q_{\text{conv}} = hA(T_1 - T_2) \tag{A.4}$$

where h is the heat transfer coefficient, with units $\left[\frac{\text{W}}{\text{m}^2\text{K}}\right]$ a term that defines how effectively heat can leave a surface, assuming both conductive and convective modes of heat transfer. Now having the two equations defining the heat transfer given in Equations (A.3) and (A.4) we can divide the two to solve for the Nusselt number as defined previously in Equation (A.1), as

$$\frac{q_{\text{conv}}}{q_{\text{cond}}} = \frac{hA(T_1 - T_2)}{\frac{kA}{L}(T_1 - T_2)} \Longrightarrow Nu = \frac{hL}{k} \tag{A.5}$$

A.2.1 Solution Methodology

As shown above, the Nusselt number can also be seen as a dimensionless heat transfer coefficient, allowing for calculation of convective heat transfer processes, but how is it that we determine a value for the Nusselt number? From physical experiments, researchers have developed many analytical correlations for the Nusselt number for specific flow environments. Basing these correlations off other dimensionless parameters allows these analytical expressions to only change for different geometries, specific heating conditions (i.e. constant heat flux, constant surface temperature), and fluid flow regimes (i.e. natural, forced convection). Engineers use a correlation, valid for the system in question, to solve for a Nusselt number value from which are able to calculate the heat transfer coefficient. With this, and knowing the heat transfer rate q [W] and now the heat transfer coefficient h, we can employ Newton's Law of Cooling (A.4) to predict the temperatures of a surface or object (T_1 , T_2) in question.

Nusselt number correlations are intended to give a good estimate of the heat transfer occurring in simple systems, but cannot be assumed to have much accuracy when the geometry is complex. If necessary, a detailed study can yield a more accurate prediction of the heat transfer rate. Simulations of the system using a CFD code such as FLUENT, along with physical experimentations of the system, can produce the necessary information. By specifying a heating condition (constant heat flux), with a fluid of known thermophysical properties, and for a geometry of known dimensions, temperatures of both the heated surface and the fluid can be observed and recorded. By varying the power input into the heated object, one can determine h for a range of temperature differences using Equation (A.4). Because these models are physical, the effect of the boundary layer is inherent in the study and does not need to be accounted for in the model using the heat transfer coefficient. This procedure is suitable for both simulations and physical experimentation.

As of now, there does not exist any experiments (simulation or physical model) that predict the heat transfer coefficients for the range of temperature differences for the Yucca Mountain in-drift geometry. There have been CFD studies performed on this system, however, these simulations do not encompass the entire range of temperature differences expected to occur over the time scale our numerical model will simulate. Because of this we are unable to predict the heat transfer coefficients using this method.

A.3 Correlation Approximations

Instead, we have used to use Nusselt correlations to account for heat transfer due to natural convection in a drift at the Yucca Mountain repository. Again, because of the uniqueness of its configuration (an eccentric cylinder-in-cylinder), no specific

correlation has been developed to predict the heat-transfer for the in-drift geometry. Following the methodology used by Webb et al. in their condensation model[36, 58], the in-drift geometry can be approximated by grouping into simpler geometries, as shown in Figure 4.3, where the expanded approximation procedure is shown in Figure A.2. Correlations for such geometries exist, yielding a value for the Nusselt number for each geometric approximation, from where, using Equation (A.5) and selecting an appropriate distanct, L, an effective heat or mass conductivity, k, can be calculated. These calculations have been implemented into TOUGH2 to account for boundary-layer heat and mass transfer and the heat transfer coefficient. The correlations for each geometric representation are presented as follows.

A.3.1 Drift Wall to Air

The fractured rock drift wall is represented by the fluid in horizontal cylinder correlation, with heat transfer coefficient defined as,

$$hc_{\text{wall}} = \frac{Nu_{\text{wall}}\, k_{\text{gas}}}{D_{\text{drift}}} \tag{A.6}$$

$$Nu_{\text{wall}} = \frac{2}{-\ln\left[1 - \frac{2}{A}\right]} \tag{A.7}$$

$$A = \left[(B)^{15} + \left(0.1\, Ra_{\text{wall}}^{1/3}\right)^{15}\right]^{1/15} \tag{A.8}$$

where B is defined as,

$$B = \left[\left(\frac{2}{1 - e^{-0.25}}\right)^{5/3} + \left(0.587\, G\, Ra_{\text{wall}}^{1/4}\right)^{5/3}\right]^{3/5} \tag{A.9}$$

$$G = \left[\left(1 + \frac{0.6}{Pr_{\text{gas}}^{0.7}}\right)^{-5} + \left(0.4 + 2.6\, Pr_{\text{gas}}^{0.7}\right)^{-5}\right]^{-1/5} \tag{A.10}$$

$$Ra_{\text{wall}} = g\, \frac{\beta_{\text{gas}}}{\nu_{\text{gas}}^2}\, Pr_{\text{gas}}\, D_{\text{wall}}^3\, |T_{\text{wall}} - T_{\text{gas}}| \tag{A.11}$$

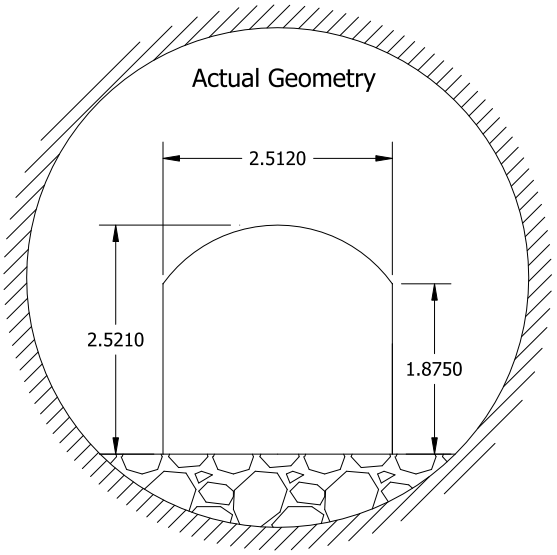

(a) Actual Geometry

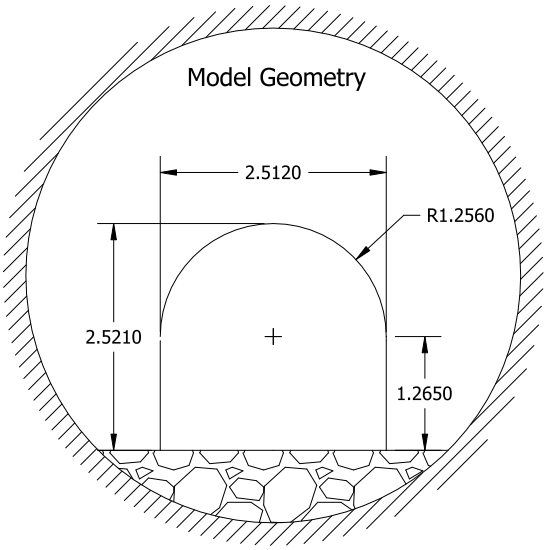

(b) Model Geometry

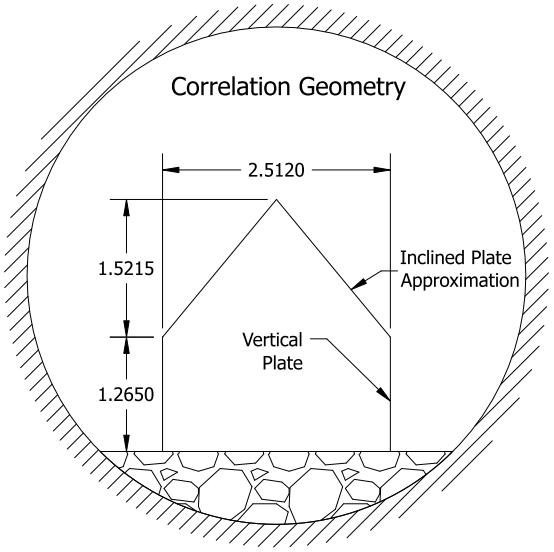

(c) Correlation Geometry

Figure A.2: In-drift geometry approximations for use of natural convection correlations, with dimension in unit meters. Shown are the (a) *actual geometry* of the in-drift, the (b) *model geometry* of the waste package element in the numerical simulation, and finally, the (c) *correlation geometry*.

A.3.2 Drip Shield to Air: Sidewalls

The drip shield sidewall are represented by vertical heated plate correlations, presented here with the heat transfer coefficient defined as,

$$hc_{\text{sides}} = \frac{Nu_{\text{sides}}\, k_{\text{gas}}}{L_{\text{sides}}} \tag{A.12}$$

$$Nu_{\text{sides}} = \left(Nu_l^6 + Nu_t^6 \right)^{1/6} \tag{A.13}$$

$$Nu_T = \bar{C}_l\, Ra_{\text{sides}}^{1/4} \tag{A.14}$$

$$Nu_t = \hat{C}_l\, Ra_{\text{sides}}^{1/3} \tag{A.15}$$

$$Nu_l = \frac{2.8}{\ln\left(1 + \frac{2.8}{Nu_T}\right)} \tag{A.16}$$

$$\bar{C}_l = \frac{4}{3}\, C_l \tag{A.17}$$

$$\hat{C}_t = \frac{0.13\, Pr_{\text{gas}}^{0.22}}{\left(1 + 0.61\, Pr_{\text{gas}}^{0.81}\right)^{0.42}} \tag{A.18}$$

$$C_l = \frac{0.503}{\left[1 + \left(\frac{0.492}{Pr_{\text{gas}}}\right)^{9/16}\right]^{4/9}} \tag{A.19}$$

$$Ra_{\text{sides}} = g \frac{\beta}{\nu_{\text{gas}}^2}\, Pr_{\text{gas}}\, L_{\text{sides}}^3\, |T_{\text{wall}} - T_{\text{gas}}| \tag{A.20}$$

A.3.3 Drip Shield to Air: Curved Top

The top curved portion of the drip shield is represented by inclined heated plate correlations, with heat transfer coefficient defined as,

$$hc_{\text{top}} = \frac{Nu_{\text{top}}\, k_{\text{gas}}}{\frac{P_{\text{top}}}{2}} \tag{A.21}$$

$$Nu_{\text{top}} = \left(Nu_l^6 + Nu_t^6 \right)^{1/6} \tag{A.22}$$

$$Nu_t = C_t\, Ra_{\text{top}}^{1/3} \tag{A.23}$$

$$C_t = \left(C_{tH} \sin(\phi_{\text{avg}}) \right)^{1/3} \tag{A.24}$$

$$C_{tH} = 0.14 \tag{A.25}$$

$$Ra_{\text{top}} = g \frac{\beta}{\nu_{\text{gas}}^2}\, Pr_{\text{gas}} \left(\frac{P_{\text{top}}}{2} \right)^3 |T_{\text{wall}} - T_{\text{gas}}| \tag{A.26}$$

with inclined plate geometry defined by,

$$\phi_{\text{avg}} = \frac{1}{2} \left(\frac{\pi}{2} + \alpha_{arc} \right) \tag{A.27}$$

$$\alpha_{arc} = \text{acos} \left(\frac{P_{inv}}{2\, R_{ds}} \right) \tag{A.28}$$

A.3.4 Invert to Air

The invert to air heat transfer is represented by horizontal heated plates correlations, with heat transfer coefficient given as,

$$hc_{\text{invert}} = \begin{cases} \dfrac{Nu_{\text{invert}}\, k_{\text{gas}}}{P_{\text{invert}}} & \text{if} \quad T_{\text{invert}} > T_{\text{gas}} \\ \dfrac{k_{\text{gas}}}{H_{\text{wp}}} & \text{if} \quad T_{\text{invert}} < T_{\text{gas}} \end{cases} \tag{A.29}$$

$$Nu_{\text{invert}} = \left[Nu_l^{10} + Nu_t^{10}\right]^{0.1} \tag{A.30}$$

$$Nu_t = C_t^H Ra_{\text{invert}}^{1/3} \tag{A.31}$$

$$Nu_l = \frac{C_t^H Ra_{\text{invert}}^{1/3}}{\ln\left(1 + \frac{1.4}{Nu_T}\right)} \tag{A.32}$$

$$Nu_T = 0.835\,\bar{C}_l\,Ra_{\text{invert}}^{1/4} \tag{A.33}$$

$$C_t^H = 0.14 \tag{A.34}$$

$$\bar{C}_l = \frac{4}{3} C_l \tag{A.35}$$

$$C_l = \frac{0.503}{\left[1 + \left(\frac{0.492}{Pr_{\text{gas}}}\right)^{9/16}\right]^{4/9}} \tag{A.36}$$

$$Ra_{\text{invert}} = g\,\frac{\beta_{\text{gas}}}{\nu_{\text{gas}}^2}\,Pr_{\text{gas}}\,P_{\text{invert}}^3\,|T_{\text{invert}} - T_{\text{gas}}| \tag{A.37}$$

Bibliography

[1] W.R. Stratton and D.R. Smith. A review of criticality accidents. Technical Report DOE/NCT-04, Lawrence Livermore National Lab, CA (USA), 1989.

[2] T.P. McLaughlin, S.P. Monahan, N.L. Pruvost, V.V. Frolov, B.G. Ryazanov, and V.I. Sviridov. A review of criticality accidents. *Los Alamos, NM: Los Alamos National Laboratory*, pages 9–13, 2000.

[3] The National Academy of Sciences and the National Research Council. The disposal of radioactive waste on land: Report of the comittee of waste disposal of the division of earth sciences. *The National Acadamies Press*, Publication 519, September 1957. URL http://www.nap.edu/catalog.php?record_id=10294.

[4] Richard G. Hewlett and Oscar E. Anderson. Condensed AEC Annual Financial Report, FY 1953. In *The New World: A History of the United States Atomic Energy Commission* Hewlett and Anderson [82], pages 723–724.

[5] Glenn Butts and Kent Linton. The joint confidence level paradox: A history of denial. Technical report, NASA 2009 Cost Estimating Symposium, April 28th 2009.

[6] Stephen Daggett. Costs of Major U.S. Wars. Technical Report 7-5700/RS22926, Congressional Research Service, June 29 2010.

[7] Office of Civilian Radioactive Waste Management. Analysis of the total system life cycle cost of the civilian radioactive waste management program, fiscal year 2007. Technical Report DOE/RW-0591, U.S. Department of Energy, Washington D.C., July 2008.

[8] United States Department of Energy. Motion to withdraw (request for dismissal of yucca mountain license application). Technical Report Docket No. 63-001, ASLBP No. 09-892-HLW-CAB04, U.S. Department of Energy, March, 1 2010.

[9] Mujid Kazimi, Ernest J. Moniz, and Charles W. Forsberg. The future of the nuclear fuel cycle: An interdiciplinary MIT study. Technical report, Massachusetts Institute of Technology, September 2010.

[10] Steve Tetreault. Yucca project review halted—NRC chief tables viability study of nuclear waste site. *Las Vegas Review-Journal*, October 6, 2010.

[11] J.S. Stuckless and R.A. Levich. *The geology and climatology of Yucca Mountain and vicinity, Southern Nevada and California*. Geological Society of America, 2007.

[12] Y.S. Wu, L. Pan, W. Zhang, and G.S. Bodvarsson. Characterization of flow and transport processes within the unsaturated zone of yucca mountain, nevada, under current and future climates. *Journal of contaminant hydrology*, 54(3-4):215–247, 2002.

[13] J.S. Stuckless and R.A. Levich. Geology of the yucca mountain site area, southern Nevada. In *The geology and climatology of Yucca Mountain and vicinity, Southern Nevada and California* Stuckless and Levich [11], pages 97–98.

[14] F. King, M. Kolar, J.H. Kessler, and M. Apted. Yucca Mountain engineered barrier system corrosion model (EBSCOM). *Journal of Nuclear Materials*, 379(1-3): 59–67, 2008.

[15] G.J. Moridis, Q. Hu, Y.S. Wu, and G.S. Bodvarsson. Preliminary 3-d site-scale studies of radioactive colloid transport in the unsaturated zone at Yucca Mountain, Nevada. *Journal of Contaminant Hydrology*, 60(3-4):251–286, 2003.

[16] A. Macfarlane. *Uncertainty underground: Yucca Mountain and the nation's high-level nuclear waste*. The MIT Press, 2006.

[17] J.T. Birkholzer, S.W. Webb, N. Halecky, P.F. Peterson, and G.S. Bodvarsson. Evaluating the Moisture Conditions in the Fractured Rock at Yucca Mountain: The Impact of Natural Convection Processes in Heated Emplacement Drifts. *Vadose Zone Journal*, 5(4):1172–1193, 2006.

[18] K. Campbell, A. Wolfsberg, J. Fabryka-Martin, and D. Sweetkind. Chlorine-36 data at yucca mountain: Statistical tests of conceptual models for unsaturated-zone flow. *Journal of contaminant hydrology*, 62:43–61, 2003.

[19] G.S. Bodvarsson, W. Boyle, R. Patterson, and D. Williams. Overview of scientific investigations at yucca mountain–the potential repository for high-level nuclear waste. *Journal of Contaminant Hydrology*, 38(1-3):3–24, 1999.

[20] A.L. Flint, L.E. Flint, G.S. Bodvarsson, E.M. Kwicklis, and J. Fabryka-Martin. Evolution of the conceptual model of unsaturated zone hydrology at Yucca Mountain, Nevada. *Journal of Hydrology*, 247(1-2):1–30, 2001.

[21] J.S.Y. Wang and T.N. Narasimhan. Hydrologic mechanisms governing fluid flow in a partially saturated, fractured, porous medium. *Water Resources Research*, 21(12): 1861–1874, 1985.

[22] K. Pruess, J.S.Y. Wang, and Y.W. Tsang. On thermohydrologic conditions near high-level nuclear wastes emplaced in partially saturated fractured tuff: 2. effective continuum approximation. *Water Resources Research*, 26:1249–1261, 1990.

[23] K. Pruess, J.S.Y. Wang, and Y.W. Tsang. On thermohydrologic conditions near high-level nuclear wastes emplaced in partially saturated fractured tuff: 1. simulation studies with explicit consideration of fracture effects. *Water Resources Research*, 26(6): 1235–1248, 1990.

[24] K. Pruess. TOUGH2: A general-purpose numerical simulator for multiphase fluid and heat flow. Technical report, Lawrence Berkeley National Laboratory, Berkeley, California (United States), 1991.

[25] C.B. Haukwa, Y.S. Wu, and G.S. Bodvarsson. Thermal loading studies using the yucca mountain unsaturated zone model. *Journal of Contaminant Hydrology*, 38 (1-3):217–255, 1999.

[26] C.B. Haukwa, Y.W. Tsang, Y.S. Wu, and G.S. Bodvarsson. Effect of heterogeneity in fracture permeability on the potential for liquid seepage into a heated emplacement drift of the potential repository. *Journal of Contaminant Hydrology*, 62: 509–527, 2003.

[27] J.T. Birkholzer, S. Mukhopadhyay, and Y.W. Tsang. The impact of preferential flow on the vaporization barrier above waste emplacement drifts at Yucca Mountain, Nevada. *Nuclear Technology*, 148(2):138–150, 2004.

[28] T.A. Buscheck, N.D. Rosenberg, J. Gansemer, and Y. Sun. Thermohydrologic behavior at an underground nuclear waste repository. *Water Resources Research*, 38 (3):1028, 2002.

[29] J.T. Birkholzer and Y.W. Tsang. Modeling the thermal-hydrologic processes in a large-scale underground heater test in partially saturated fractured tuff. *Water Resources Research*, 36(6):1431–1447, 2000.

[30] Y.W. Tsang and J.T. Birkholzer. Predictions and observations of the thermal-hydrological conditions in the single heater test. *Journal of Contaminant Hydrology*, 38(1-3):385–425, 1999.

[31] S. Mukhopadhyay and Y.W. Tsang. Understanding the anomalous temperature data from the Large Block Test at Yucca Mountain, Nevada. *Water Resources Research*, 38(10):1210, 2002.

[32] S. Mukhopadhyay and Y.W. Tsang. Uncertainties in coupled thermal-hydrological processes associated with the drift scale test at Yucca Mountain, Nevada. *Journal of Contaminant Hydrology*, 62:595–612, 2003.

[33] T.A. Buscheck. Multiscale thermohydrologic model. CRWMS M&O report ANL-EBSMD-000049 REV 03 ICN, Bechtel SAIC Company, Las Vegas, Nevada, 2005.

[34] J.T. Birkholzer. A temperature-profile method for estimating flow in geologic heat pipes. *Journal of Contaminant Hydrology*, 85(3-4):89–117, 2006. ISSN 0169-7722.

[35] J.E. Houseworth, S. Finsterle, and G.S. Bodvarsson. Flow and transport in the drift shadow in a dual-continuum model. *Journal of contaminant hydrology*, 62: 133–156, 2003. ISSN 0169-7722.

[36] S. Webb and M. Itamura. Calculation of post-closure natural convection heat and mass transfer in Yucca Mountain drifts. In *Proceedings of HTFED04 2004 ASME Heat Transfer/Fluids Engineering Summer Conference*, Charlotte, NC, USA, 07 2004. American Society of Mechanical Engineers.

[37] T.A. Ghezzehei, R.C. Trautz, S. Finsterle, P.J. Cook, and C.F. Ahlers. Modeling coupled evaporation and seepage in ventilated cavities. *Vadose Zone Journal*, 3(3):806–818, 2004.

[38] G. Danko and D. Bahrami. Powered and natural passive ventilation at Yucca Mountain. In *Proc. Int. High-Level Radioactive Waste Manage. Conf., 10th, Las Vegas, NV*, volume 30, pages 683–690, 2003.

[39] G. Danko and D. Bahrami. Heat and moisture flow simulation with MULTIFLUX. ASME Heat Transfer/Fluids Eng. Summer Conf., Charlotte, NC, American Society of Mechanical Engineers, New York, June 11-15, 2004.

[40] M.L. Corradini. Comments on the data and analyses related to corrosion presented at the may board meeting (letter from Michael L. Corradini to Margaret Chu). Letter, October 21, 2003.

[41] Per F. Peterson. Letter to Nuclear Waste Technical Review Board in response to comments regarding canister corrosion in Yucca Mountain by deliquescence. Letter, May 9, 2004.

[42] M. Apted, R. Arthur, F. King, D. Langmuir, and J. Kessler. The unlikelihood of localized corrosion of nuclear waste packages arising from deliquescent brine formation. *Journal of the Minerals*, 57(1):43–48, 2005.

[43] K. Pruess. The TOUGH Codes–A Family of Simulation Tools for Multiphase Flow and Transport Processes in Permeable Media. *Vadose Zone Journal*, 3(3):738, 2004.

[44] T.N. Narasimhan and P.A. Witherspoon. An integrated finite difference method for analyzing fluid flow in porous media. *Water Resour. Res*, 12(1):57–64, 1976.

[45] K. Pruess, C. Oldenburg, and G. Moridis. TOUGH2 User's Guide, version 2.0. Technical Report LBNL-43134, Lawrence Berkeley Nat. Lab, Berkeley, CA, 1999.

[46] J.T. Birkholzer, S. Mukhopadhyay, and Y.W. Tsang. Drift-Scale Coupled Processes (DST and TH Seepage) Models. Yucca Mountain Project Report MDL-NBS-HS-000015 REV 01, Bechtel SAIC Company, Las Vegas, Nevada, 2004.

[47] J.T. Birkholzer, S. Mukhopadhyay, and Y.W. Tsang. Modeling seepage into heated waste emplacement tunnels in unsaturated fractured rock. *Vadose Zone Journal*, 3:819–836, 2004.

[48] G.D. Raithby and K.G.T. Hollands. *Handbook of heat transfer fundamentals*, volume 2. McGraw-Hill Book Company, New York, 1985.

[49] J.H. Lienhard IV and J.H. Lienhard V. *A heat transfer textbook*. Number TJ260.L445 v1.31. Philogiston Press, Englewood Cliffs, NJ, 3rd edition, January 16, 2008.

[50] J.C. Chai, H.O.S. Lee, and S.V. Patankar. Ray effect and false scattering in the discrete ordinates method. *Numerical Heat Transfer, Part B: Fundamentals*, 24(4): 373–389, 1993. ISSN 1040-7790.

[51] T.D. Panczak and S.G. Ring. RadCAD—Integrating radiation analysis with modern CAD systems. In *SAE, International Conference on Environmental Systems, 26 th, Monterey, CA*, 1996.

[52] T.D. Panczak, M. Welch, et al. Thermal Desktop® User's Manual. Technical report, Cullimore and Ring Technologies, Inc., Littleton, Colorado, October 2006.

[53] Waste Packages and Source Terms for the Commercial 1999 Design Basis Waste Streams. Yucca Mountain Project Report CAL-MGR-MD-000001 REV 00, CRWMS M&O, Las Vegas, Nevada, 2000.

[54] Repository Design Project, IED Typical Waste Package Components Assembly. Technical Report 800-IED-WIS0-00203-000-00B, Bechtel SAIC Company, 2003.

[55] S.W. Webb, N.D. Francis, S.D. Dunn, M.T. Itamura, and D.L. James. Thermally induced natural convection effects in Yucca Mountain drifts. *Journal of Contaminant Hydrology*, 62:713–730, 2003. ISSN 0169-7722.

[56] T.H. Kuehn and R.J. Goldstein. An experimental study of natural convection heat transfer in concentric and eccentric horizontal cylindrical annuli. *Journal of Heat Transfer*, 100:635, 1978.

[57] T.H. Kuehn and R.J. Goldstein. Correlating equations for natural convection heat transfer between horizontal circular cylinders. *International Journal of Heat and Mass Transfer*, 19(10):1127–1134, 1976. ISSN 0017-9310.

[58] S.W. Webb and A. Reed. In-drift natural convection and condensation. Technical report, MDL-EBS-MD-000001 REV 00, Yucca Mountain Project Report, Bechtel SAIC Company, Las Vegas, Nevada, 2004, 2003.

[59] G. Danko and D. Bahrami. Coupled, Multi-Scale Thermohydrologic-Ventilation Modeling with MULTIFLUX. In *SME Annual Meeting and Exhibit*, pages 1–18, Denver, Colorado, February 23–25, 2004. Society of Mining Engineers.

[60] J.T. Birkholzer, N. Halecky, S.W. Webb, P.F. Peterson, and G.S. Bodvarsson. The Impact of Natural Convection on Near-Field TH Processes at Yucca Mountain. In *11th International High-Level Nuclear Waste Conference (IHLRWM)*, Las Vegas, NV, April 30–May 2 2006. American Nuclear Society.

[61] A.F. Mills. *Mass Transfer*. Prentice Hall, Upper Saddle River, New Jersey, 2nd edition, May 3, 2001. ISBN 0130328294.

[62] W.M. Kays, M.E. Crawford, and B. Weigand. *Convective Heat and Mass Transfer*. McGraw-Hill Science/Engineering/Math, 4th edition, March 12, 2004. ISBN 0072990732.

[63] Per F. Peterson. Diffusion layer modeling for condensation with multicomponent noncondensable gases. *Journal of Heat Transfer*, 122:716, 2000.

[64] N.F. Spycher, E.L. Sonnenthal, and J.A. Apps. Fluid flow and reactive transport around potential nuclear waste emplacement tunnels at yucca mountain, nevada. *Journal of Contaminant Hydrology*, 62-63:653–673, 2003.

[65] J.T. Birkholzer, N. Halecky, S.W. Webb, P.F. Peterson, and G.S. Bodvarsson. A Modeling Study Evaluating the Thermal-Hydrological Conditions in and near Waste Emplacement Drifts at Yucca Mountain. *Nuclear Technology*, 63(1):147–164, 2008.

[66] Ventilation Model and Analysis Report. Yucca Mountain Project Report ANL-EBS-MD-000030 REV 04, Bechtel SAIC Company, Las Vegas, Nevada, 2004.

[67] R.D. McCurley, C.K. Ho, M.L. Wilson, and J.A. Hevesi. Analysis of Infiltration Uncertainty. Yucca Mountain Project Report ANL-NBS-HS-000027 REV 01, Sandia National Laboratory, Albuquerque, NM, and Livermore, CA (US), 2000.

[68] T.A. Ghezzehei and H.H. Liu. Calibrated Properties Model. Yucca Mountain Project Report MDL-NBS-HS-000003 REV2, Bechtel SAIC Company, Las Vegas, Nevada, 2004.

[69] J. Rutqvist and C.F. Tsang. Analysis of thermal-hydrologic-mechanical behavior near an emplacement drift at yucca mountain. *Journal of Contaminant Hydrology*, 62: 637–652, 2003. ISSN 0169-7722.

[70] J.T. Birkholzer, G. Li, C.F. Tsang, and Y. Tsang. Modeling Studies and Analysis of Seepage into Drifts at Yucca Mountain. *Journal of Contaminant Hydrology*, 38(1-3):349–384, 1999.

[71] T. Vogt. Geologic Framework Model (GFM2000). Yucca Mountain Project Report MDL-NBS-GS-000002, REV 02, Bechtel SAIC Company, Las Vegas, Nevada (US), 2004.

[72] K. Zhang, Y.S. Wu, and G.S. Bodvarsson. Parallel computing simulation of fluid flow in the unsaturated zone of yucca mountain, nevada. *Journal of contaminant hydrology*, 62:381–399, 2003.

[73] Wikipedia. Parallel computing — wikipedia, the free encyclopedia, 2010. URL http://en.wikipedia.org/w/index.php?title=Parallel_computing&oldid=337297418. [Online; accessed 18-January-2010].

[74] S. Finsterle, C.F. Ahlers, R.C. Trautz, and P.J. Cook. Inverse and predictive modeling of seepage into underground openings. *Journal of Contaminant Hydrology*, 62:89–109, 2003.

[75] C. Doughty, R. Salve, and J.S.Y. Wang. Liquid-release tests in unsaturated fractured welded tuffs: II. Numerical Modeling. *Journal of Hydrology*, 256(1-2):80–105, 2002.

[76] R. Salve, J.S.Y. Wang, and C. Doughty. Liquid-release tests in unsaturated fractured welded tuffs: I. Field Investigations. *Journal of Hydrology*, 256(1-2):60–79, 2002.

[77] R.G. Sargent. Verification and validation of simulation models. In *Proceedings of the 37th conference on Winter simulation*, page 143. Winter Simulation Conference, 2005.

[78] C.M. Macal. Model verification and validation. In *Workshop on "Threat anticipation: Social science methods and models". The University of Chicago and Argonne National Laboratory*. Citeseer, 2005.

[79] K. Pruess and TN Narasimhan. On fluid reserves and the production of superheated steam from fractured, vapor-dominated geothermal reservoirs. *J. Geophys. Res*, 87 (B11):9329–9339, 1982.

[80] T.A. Buscheck, J.J. Nitao, and D.G. Wilder. Repository-heat-driven hydrothermal flow at Yucca Mountain, Part II. Large-scale in situ heater test. *Nuclear Technology*, 104(3), 1993.

[81] SD Dunn, B. Lowry, B. Walsh, JD Mar, C. Howard, R. Johnston, and T. Williams. YMP Engineered Barrier Systems Scaled Ventilation Testing. Yucca mountain project report, Bechtel SAIC Company, Las Vegas, Nevada (US), 2002.

[82] Richard G. Hewlett and Oscar E. Anderson. *The New World: A History of the United States Atomic Energy Commission*, volume 1. University of California Press, Berkeley, California, 1990.